Publication Year	2022
Acceptance in OA	2025-03-13T13:57:04Z
Title	Spacecraft sample collection and subsurface excavation of asteroid (101955) Bennu
Authors	Lauretta, D. S., Adam, C. D., Allen, A. J., Ballouz, R. L., Barnouin, O. S., Becker, K. J., Becker, T., Bennett, C. A., Bierhaus, E. B., Bos, B. J., Burns, R. D., Campins, H., Cho, Y., Christensen, P. R., Church, E. C.A., Clark, B. E., Connolly, H. C., Daly, M. G., DellaGiustina, D. N., d'Aubigny, C. Y.Drouet, Emery, J. P., Enos, H. L., Kasper, S. Freund, Garvin, J. B., Getzandanner, K., Golish, D. R., Hamilton, V. E., Hergenrother, C. W., Kaplan, H. H., Keller, L. P., Lessac-Chenen, E. J., Liounis, A. J., Ma, H., McCarthy, L. K., Miller, B. D., Moreau, M. C., Morota, T., Nelson, D. S., Nolau, J. O., Olds, R., PAJOLA, Maurizio, Pelgrift, J. Y., Polit, A. T., Ravine, M. A., Reuter, D. C., Rizk, B., Rozitis, B., Ryan, A. J., Sahr, E. M., Sakatani, N., Seabrook, J. A., Selznick, S. H., Skeen, M. A., Simon, A. A., Sugita, S., Walsh, K. J., Westermann, M. M., Wolner, C. W.V., Yumoto, K.
Publisher's version (DOI)	10.1126/science.abm1018
Handle	http://hdl.handle.net/20.500.12386/36757
Journal	SCIENCE
Volume	377

The Subsurface of Bennu Excavated by OSIRIS-REx Sample Collection

Authors: D. S. Lauretta[1*], C. D. Adam[2], A. J. Allen[3], R.-L. Ballouz[1], O. S. Barnouin[4], K. J. Becker[1], T. Becker[1], C. A. Bennett[1], E. B. Bierhaus[5], B. J. Bos[6], R. D. Burns[6], H. Campins[3], Y. Cho[7], P. R. Christensen[8], E. C. A. Church[5], B. E. Clark[9], H. C. Connolly Jr.[10,1], M. G. Daly[11], D. N. DellaGiustina[1], C. Y. Drouet d'Aubigny[1], J. P. Emery[12], H. L. Enos[1], S. Freund Kasper[5], J. B. Garvin[6], K. Getzandanner[6], D. R. Golish[1], V. E. Hamilton[13], C. W. Hergenrother[1,†], H. H. Kaplan[6], L. P. Keller[14], E. J. Lessac-Chenen[2], A. J. Liounis[2], H. Ma[5], L. K. McCarthy[2], B. D. Miller[5], M. C. Moreau[2], T. Morota[7], D. S. Nelson[2], J. O. Nolau[3], R. Olds[5], M. Pajola[15], J. Y. Pelgrift[2], A. T. Polit[1], M. A. Ravine[16], D. C. Reuter[6], B. Rizk[1], B. Rozitis[17], A. J. Ryan[1], E. M. Sahr[2], N. Sakatani[18], J. A. Seabrook[11], S. H. Selznick[1,†], M. A. Skeen[5], A. A. Simon[6], S. Sugita[7], K. J. Walsh[13], M. M. Westermann[1], C. W. V. Wolner[1], K. Yumoto[7]

Affiliations:

[1]Lunar and Planetary Laboratory, University of Arizona, Tucson, Arizona, USA.

[2]KinetX, Simi Valley, CA, USA.

[3]Physics Department, University of Central Florida, Orlando, FL, USA.

[4]The Johns Hopkins University Applied Physics Laboratory, Laurel, MD, USA.

[5]Lockheed Martin Space, Littleton, CO, USA.

[6]Goddard Space Flight Center, Greenbelt, MD, USA.

[7]Department of Earth and Planetary Environmental Science, University of Tokyo, Tokyo, Japan.

[8]School of Earth and Space Exploration, Arizona State University, Tempe, AZ, USA.

[9]Department of Physics and Astronomy, Ithaca College, Ithaca, NY, USA.

[10]Department of Geology, Rowan University, Glassboro, NJ, USA.

[11]Department of Earth and Space Science and Engineering, York University, Toronto, ON, Canada.

[12]Department Astronomy & Planetary Science, Northern Arizona University, Flagstaff, AZ, USA.

[13]Southwest Research Institute, Boulder, CO, USA.

[14]Johnson Space Center, Houston, TX, USA.

[15]INAF National Institute for Astrophysics - Astronomical Observatory of Padova, Italy

[16]Malin Space Systems, San Diego, CA, USA.

[17]School of Physical Sciences, Open University, Milton Keynes, UK.

[18]Department of Physics, Rikkyo University, Tokyo, Japan.

[†]Now at Ascending Node Technologies, Tucson, AZ, USA.

*Corresponding author. Email: lauretta@arizona.edu

Abstract: The OSIRIS-REx spacecraft acquired imaging and spectral data during and after collecting a sample of surface particles from the primitive asteroid Bennu. Sampling mobilized sub-millimeter dust, which was thought to be rare or absent. Thermal emission spectra of the dust match those of type-1 CI and CM chondrites, the meteorites that experienced the most intense aqueous alteration. The 9-meter-long elliptical crater excavated by sampling is darker, spectrally redder, and has more fine particulates than the original surface. The displaced volume of 12.2 ± 0.9 cubic meters is consistent with a subsurface bulk density of 500-700 kilograms per cubic meter, less than that of the asteroid. The spacecraft stowed 250 ± 101 grams of sample, which will be returned to Earth in 2023.

One-Sentence Summary: Sample collection from Bennu excavated a crater and exposed a fine-grained, very low-density subsurface.

Main Text:

On 20 October 2020, the Origins, Spectral Interpretation, Resource Identification, and Security–Regolith Explorer (OSIRIS-REx) spacecraft collected rock particles from the surface of the ~500-m-diameter rubble-pile asteroid (101955) Bennu. Sampling this body was challenging [1] owing to Bennu's microgravity environment [2] and unexpectedly rocky and rough surface [3]. The Touch-and-Go Sample Acquisition Mechanism (TAGSAM) [4], a circular sample collection device connected to the spacecraft by a pogo stick–like arm (fig. S1), contacted the asteroid for 6 s before the spacecraft's back-away thrusters fired [1]; hence the moniker Touch-and-Go sampling, or TAG (fig S2).

The sampling event was documented by the SamCam imager of the OSIRIS-REx Camera Suite (OCAMS) [5,6], the NavCam 2 imager of the Touch-and-Go Camera System (TAGCAMS) [7,8], the OSIRIS-REx Thermal Emission Spectrometer (OTES) [9], and the spacecraft's inertial measurement unit (IMU). SamCam also imaged TAGSAM two days later to verify collection of the sample. SamCam and StowCam (another camera in the TAGCAMS suite) imaged TAGSAM again 8 days after sample collection as it was stowed in the protective sample return cannister.

On 7 April 2021, the spacecraft, which had been drifting away from the asteroid since sample collection, returned to Bennu for a final flyby to characterize the disturbance of the surface in response to sampling [10-§2.1]. It surveyed Bennu from 3.7 km in a series of north-south linear scans optimized for the OCAMS PolyCam telescopic imager [5,6] to obtain images at 5 cm pixel scale (nadir resolution). Other instruments aboard OSIRIS-REx [11] also collected scientific data, including the OCAMS MapCam multispectral imager at 25 cm pixel scale, OTES at 28.2-m footprint, and the OSIRIS-REx Visible and InfraRed Spectrometer (OVIRS) [12] at 14.1-m footprint (fig. S3). Here we analyze the observations acquired during and after sampling to gain insight into the properties of Bennu's subsurface (to a depth of about 1 meter) and the nature of the collected sample, which will be delivered to Earth in 2023 [1].

Site of sample collection

The sample was collected from a site dubbed Nightingale, situated within the 20-m-diameter Hokioi Crater with center coordinates of about 56°, 43° (Fig. 1A). This site was selected for sampling because, in addition to spacecraft navigation and safety considerations [1,13], it has a high abundance — relative to the rest of the boulder-dominated asteroid [3] — of surface particles <2 cm in diameter [14], the size class ingestible by TAGSAM [4,15]. Spectra collected before sampling indicated the presence at Nightingale of hydrated phyllosilicates [16-18], the iron oxide magnetite [3,16,19], and carbon in the form of organic molecules [18,20] and carbonate minerals [21]. In panchromatic images, the site exhibits a salt-and-pepper appearance (Fig. 1B), suggesting that Bennu's two major lithologies — dark with low thermal inertia and brighter with higher thermal inertia [19,21,22] — might both be sampled. The Hokioi Crater is part of the population of small craters on Bennu that are spectrally redder than average, which are proposed to be among the youngest features on the surface [19]. Together with this crater's relatively cool mid-latitude location [23], this suggests a reasonable likelihood of OSIRIS-REx sampling material that has experienced minimal thermal processing or other forms of space weathering.

Contact of the sampling mechanism with the surface

About four hours and 20 minutes after the spacecraft departed from its home orbit to descend to the surface for sample collection, TAGSAM contacted Bennu at latitude 55.8993°, longitude 41.8412° with a downward velocity of 10.05 ± 0.004 cm s^{-1} (fig. S4). The actual contact

point was within 73 cm of the targeted point [10-§2.3]. The spacecraft's IMU signaled surface contact, registering a small but measurable surface contact force between 10 and 15 N [24]. One second after contact was sensed, TAGSAM released a jet of nitrogen gas that fluidized and entrained particles and guided them into the sample collection chamber (fig. S5). Six seconds after making contact, the spacecraft retained a downward velocity of ~4 cm s^{-1}. The deceleration of 6 cm s^{-1} experienced up to that point is attributable to TAGSAM gas release. Then, the spacecraft fired four of its 4.5-N thrusters, initiating the back-away maneuver. Three seconds of thruster firing arrested the residual downward velocity, and the spacecraft began to retreat from Bennu. By then, TAGSAM had penetrated 48.8 cm into the subsurface. The thrusters fired for a total of 24 s, with TAGSAM rising above the original surface height 16.6 s after initial contact. The spacecraft departed Bennu on a hyperbolic trajectory at 40 cm s^{-1}.

Overall, the surface of Bennu responded to sampling like a compliant, viscous fluid, providing minimal resistance to the downward motion of the spacecraft [24]. This response is consistent with discrete-element simulations of TAGSAM interacting with regolith that has near-zero intergranular cohesion [24-26]. It is also consistent with experimental data collected under low-gravity conditions in which loose material was easily mobilized [27].

Images collected by SamCam 0.2 seconds after contact (0.32 s before gas firing) showed evidence of surface disturbance in all directions around TAGSAM (Fig. 1D). TAGSAM partially disrupted a ~20-cm-long boulder near the eastern edge of its contact point and lofted fine particulates (fig. S6; Movie S1). Another boulder, 40-cm long and to the southeast of TAGSAM, acted like a rigid plate, flipping up and launching small particles perched on its surface (fig. S7; Movie S2). These different responses support the inference from remote sensing that Bennu's boulders have a range of strengths [22,28]. In addition, PolyCam images from the final flyby on 7 April 2021 show a 1.25-m boulder appears to have launched 12 m, landing well outside Hokioi Crater (fig. S8; Movie S3).

We compared pre-contact NavCam 2 images with post-contact images collected during back-away to constrain the extent of surface disturbance. The best pre- and post-sampling pair captured the surface at almost identical scales and attitudes and was acquired within a short enough window of time to have similar illumination (Fig. 2, A and B). Via manual, pixel-by-pixel inspection of this image pair, we traced a boundary in the post-contact image between perturbed and unperturbed surfaces. We used landmarks visible in the pre-contact image to identify surface features that were unchanged during sampling.

By using correlation and co-registration between the SamCam image acquired immediately after the initial TAGSAM surface contact and the last NavCam 2 image acquired with the Nightingale site still in its field of view, we identified the sample acquisition site in the NavCam 2 image (fig. S9). Comparing this location to the unperturbed surface boundary shows that landmark #8 (the boulder visible in the upper right corner of Fig. 2A) was unaltered by the TAG event. This feature is a little less than 7 m away from the sample acquisition site. Thus, the immediate surface alterations were generally contained within a 7-m radius of the touchdown location, though many particles were displaced much further distances.

Dust liberated by the sampling event

The release of the nitrogen gas mobilized abundant sampleable material. Comparing the NavCam 2 image acquired right before surface contact (Fig. 2C) to the image taken 0.1 s after gas release (Fig. 2D) reveals a cloud of unresolved fine particulates emanating from the contact point. We calculated the mass, particle size, and integrated layer thickness of this dust cloud by

comparing these two images. We measured the opacity of this unresolved component and integrated it with respect to distance from the center of the outflow. The reduction in brightness between the two images informs our optical model, which we use to derive an average opacity of 0.47, generated by sub-millimeter dust particles [10-§5.2].

We combined the measurement of the post–gas release dust cloud's opacity with an estimated size frequency distribution (SFD) to determine the mass and source region of the dust cloud. We used a hybrid differential SFD (Weibull/Rayleigh + power law) to model the unresolved component, with a maximum size of 3 mm (Equation S14). This value is based on a review of the cumulative SFD from other populations of particles observed at Bennu, including those ejected on 6 January 2019 [29,30], global boulder and cobble counts [31], higher-resolution counts at Nightingale and other candidate sample sites [14], particles escaping from TAGSAM after sampling (discussed later), and the Weibull/Rayleigh theoretical distribution. We integrated this hybrid differential SFD with respect to particle size to derive a dust mass of 1.8 kg (–1.1/+1.2) and an initial dust layer thickness of 3.2 mm (–2.2/+3.2) based on the NavCam 2 snapshot of the cloud (Fig. 2D).

Post-sampling debris plume

In all images collected during back-away, a high-opacity feature with a large spatial extent, smooth texture (relative to the unperturbed surface), and well-defined shadows is visible (Fig. 2B). Quantitative image analyses [10-§5.3] indicate that the object is an optically dense, lofted plume with a distinct vertical and lateral velocity relative to the asteroid surface. The morphology of the plume is a combination of subsurface excavation by TAGSAM gas release and pressure from the thruster exhaust. The TAG point is out of the field of view, west of the scene in Fig. 2B. Two of the thruster's impingement points are near landmarks #3 and #8 in this same image. The force from the thruster appears to modify the TAG ejecta plume, arresting the lateral velocity of finer particulates, while permitting larger boulders to continue their general eastward motion, as evidenced by their shadows over a flat, bright boulder (Movie S4).

At least one clear example of collisions between one of the mobilized boulders with a larger stationary rock is evident in the NavCam 2 back-away image set. This collision is between a lofted particle and a boulder. Fig. S12 shows a close-up of the impactor colliding with the boulder on the surface while a nearby tumbling rock spins almost in place, relative to Bennu (see also Movie S5). The impactor collides with the boulder, partially breaks apart, potentially modifies a small portion of the boulder, changes direction, appears to roll into the heavily shadowed region, and disappears. The observation of such collisions and particle fragmentation supports our interpretation that TAGSAM partially disrupted one of the boulders at the contact point. It also suggests that some of the fine, unresolved material in the lofted plume was produced by the sampling event via collisional and tribological processes involving initially larger rocks. The presence of lofted fines immediately upon gas release (Fig. 2D) revealed dust originally present in the subsurface at the Nightingale site, but additional fine-particulate material may have been created by the TAG-initiated dynamics.

Dust analysis from optical component contamination

Checkouts of the instruments after the sampling event revealed substantial degradation in the throughput of their optics, indicating accumulation of mobilized dust [10-§6.1]. The degree of dust loading experienced by the instruments varied depending upon their aperture size and location on the spacecraft; decreases in throughput ranged from ~5% (OVIRS, the instrument with the

smallest boresight and mounted on the side of the spacecraft) to 70% (NavCam 2, wide-field imager close to TAGSAM) (table S4).

In the case of OTES, the optical contamination allows us to spectrally characterize the dust (Fig. 3). The OTES post-TAG checkout indicated a ~15% decrease in signal, of which only about ~1% can be attributed to fluctuations in the measured instrument temperature (fig. S17). We produced a spectrum of the contaminating particles by using OTES observations of space with and without dust on the optics and taking their ratio [10-§6.6]. Because the instrument, and thus the particulates, are hotter than the background of space, the contaminant spectrum is analogous to an emission spectrum [32].

This spectrum has deeper absorptions than spectra of Bennu's surface [16,17]. In addition, an Mg-OH absorption centered near 605 cm^{-1} (~16.5 μm) (Fig. 3) is present that was not detected previously. We attribute this feature to hydrated Mg-rich phyllosilicate minerals [34]. Hydrated phyllosilicates were already known to be abundant on Bennu based on the ubiquitous 2.7-μm absorption feature in OVIRS data and silicate absorption band positions and shapes in the OTES spectra [16-18], which contributed to the inference that Bennu's composition is like that of the highly aqueously altered (type-1 CI and CM) chondritic meteorites [16,21], which are chemically the most primitive known meteorites, having compositions closest to that of the solar photosphere [33]. The newly detected feature confirms this interpretation and is consistent with the expectation from meteoritic analogs of Bennu that the phyllosilicates are Mg-rich.

Crater excavated by sampling

PolyCam images collected during the global survey of Bennu in 2019 (Fig. 4A) and during the final flyby on 7 April 2021 (Fig. 4B) show changes to the Hokioi Crater floor caused by the sampling event. Using stereophotoclinometry [35-37], we constructed a digital terrain model (DTM) with 5-cm ground sample distance of Hokioi Crater from these PolyCam images [10-§7.1] (Fig. 4D). We registered portions of the images to landmarks exterior to the crater that were not affected by sampling and compared the resulting DTM with one constructed pre-sampling using OSIRIS-REx Laser Altimeter (OLA) data at the same resolution [37-39] (Fig. 4C). This comparison showed that the sampling event removed the far edge of a pre-existing debris apron at the base of the Hokioi crater wall (Fig. 4, A and C; Fig S8) and replaced it with a small crater centered at 55.997°, 44.971° (Fig. 4, C and D), dubbed the TAG crater, with several boulders at its bottom (Fig. S8). This excavated crater is elliptical (9.04 × 6.54 m), with its long axis-oriented north-to-south. Its average lateral dimension is 7.8 ± 1.8 m, and its depth is 0.68 ± 0.1 m. The displaced volume is 12.2 ± 0.9 m^3. It is surrounded by sub-meter rocks mobilized by sampling and thruster firing into a campfire ring–like pattern — like those seen around small craters elsewhere on the surface [40] (Fig. S8).

The differences between the pre- and post-sampling DTMs indicate that the elliptical shape of the TAG crater is the result of two factors. First, the sampling event occurred on a 20–30° north-to-south slope, relative to Bennu's gravity vector (Fig. 4E). It is likely that a transient crater would have formed when the gas release led to upslope oversteepening, especially to the north and northwest. This interaction would have led to subsequent back-wasting upslope and produced the elliptical shape observed. Back-wasting would also explain the rock accumulations at the crater center (Fig. 4B). In mass movements on Earth [41] and on asteroids [42], larger blocks "surf" on the finer particles of regolith, flowing downslope, and are the last to be buried. Second, the sampling event excavated surface material along the north-south long axis of the TAG crater and along a line running along its short axis from the west-southwest to east-northeast (Fig. 4F and fig.

S20). These shallow trenches of material loss correspond to orientation of the backaway thrusters and thus may have been created when the spacecraft pulled away from the surface. The thrusters could have increased the volume of the observed crater by as much as 30%.

The elliptical morphology and accumulation of larger rocks at the crater bottom are not unusual for impact craters generated by low-velocity (<500 m s^{-1}) projectiles on a 20–25° slope in laboratory experiments in Earth's gravity [43-45]. Further substantiating this back-wasting hypothesis, depth profiles through the TAG crater provide evidence for removal of 5 to 20 cm of material over a broad region in the north and north-northeast (fig. S20), along the steepest areas of the Hokioi crater wall. Much of this portion of the wall likely readjusted via surface failure in response to the formation of the TAG crater.

We applied crater scaling relationships [46-48] and used the known energy of the gas released to assess the physical properties of the rubble in which the TAG crater formed [10-§7.2]. As an upper bound, we assume that the entire 8-m-average-diameter post-TAG crater is the result of TAGSAM gas release. As a lower bounding case, we remove the possible contribution to the crater size from thruster effects, yielding a 5.1-m-average-diameter (fig. S21). The formation of either size crater requires a nearly cohesionless (<1 Pa) granular material (fig. S22). Minimal surface yield strength (≤0.001Pa) in the sampled debris apron, or any cratering efficiency losses due to compaction of pore space, would not have resulted in a TAG crater as large as observed. Furthermore, we find that crater formation in a cohesionless and non-compacting surface material does not reproduce the observed crater if the bulk regolith density is the same as that of bulk Bennu (1190 kg m^{-3} [2,36]). Rather, the crater size corresponds to a bulk density of 500 kg m^{-3} for the larger crater or 700 kg m^{-3} for the smaller crater (fig S22). Our findings are consistent with independent results from spacecraft accelerometer data and granular mechanics force laws [15]. This density, combined with the estimated excavation volume, suggests that the sampling event mobilized at least 6000±650 kg, substantially more mass than predicted [24].

Properties of the subsurface

We counted particles in PolyCam images of the sample site taken during the final flyby to assess the SFD of the newly exposed subsurface [10-§8]. Previous mapping of particles in PolyCam images of Nightingale obtained at various resolutions before sampling achieved completeness limits of 0.25 ± 0.07 to 0.05 ± 0.02 m and yielded SFD power-law indices of -1.9 ± 0.3 to –2.3 ± 0.1 (fig. S23) [14]. The final flyby data yield a completeness limit of 0.22 ± 0.02 m (with a total of 561 particles larger than this limit) and a post-sampling power-law index of –2.7 ± 0.2 (fig. S27). The sampling event increased the number of visible particles less than 90 cm, suggesting that the subsurface contains smaller particles than are evident on the surface. In addition, more high-reflectance material (relative to the generally dark surface) [3,19] is visible near the contact point after sampling (Fig. 4, A and B). The change in SFD is consistent with surface modification following the formation of the crater generated by sampling. Surface flow due to back wasting of the walls of the transient TAG crater can lead to sorting with coarser pebbles and less dense materials floating to the top, while smaller fines are buried below [42]. In such flows, large rocks tend to move to the toe of the flow and can be partially buried when they come to a stop at the center of the crater, as more flow follows behind.

Post-sampling MapCam (Fig. 5A) and PolyCam (Fig. 5B) data from the final flyby show that Nightingale is darker, with normal albedo decreasing 5% (Fig. 5C) [10-§8]. MapCam color data show that the surface became spectrally redder (+0.202 percent per micron change in spectral slope) in the wavelength range 0.55 to 0.85 μm (compared to Bennu's moderately blue (negative)

average spectral slope) (Fig. 5D); and has a deeper band minimum near 0.55 μm (Fig. 5E) than before sampling [19].

The post-sampling surface is also spectrally redder and darker in OVIRS spectra (Fig. 6), compared to data collected earlier [18]. The OVIRS spectral changes are consistent with the MapCam results. The visible–near-infrared spectral slope (0.5–1 μm) at the sampling site increased by 0.19 ± 0.02 percent per micron (fig. S32), whereas the surrounding areas were essentially unchanged (0.00 ± 0.02 percent per micron). The change at the sampling site represents a 58% increase in spectral slope compared with observations from flybys in 2019 [18]. Reflectance at 0.55 μm decreased by 0.17 ± 0.02%, or ~5% relative to previous OSIRIS-REx observations after accounting for reduced optical throughput [10-§10]. The changes in reflectance are centered on the sampling site and do not extend past the edge of Hokioi Crater; the reflectance of the surrounding region did not change (0.00 ± 0.04%). The OVIRS detector was too warm during the post-sampling observations to confidently assess any possible changes at longer wavelengths.

The reflectance and spectral slope changes are consistent with predictions of the effects of space weathering based on color variation across Bennu's surface [19] — in particular, that the most freshly exposed surfaces are among the reddest and darkest owing to a high proportion of organic material. To explain Bennu's global spectrum, it was hypothesized that freshly exposed redder material undergoes carbonization during space weathering, which leads to bluing and brightening [19]. This prediction is supported by the post-sampling spectral observations.

Although magnetite production via space weathering can also cause spectral bluing [49], laboratory studies show that phyllosilicates become darker when intermixed with magnetite [50], a property that is not consistent with the brightness of materials with older putative exposure ages. Though magnetite is a likely constituent of Bennu surface materials, including in the TAG crater [3,16,17], its formation during space weathering does not appear to drive spectral changes on the asteroid based on our post-sampling observations.

Spectral reddening can also be attributed to the exposure of smaller particle sizes, it coincides with brightening, not darkening, at fine particle sizes (<100 μm) in both carbonaceous meteorite powders and Bennu simulant materials [51]. Particle size also has little effect on the position and depth of band minima at 0.55 μm, which is attributable to magnetite [52]. In addition, if the spectral changes were caused by particle size effects, then it should have produced a notable change in thermal inertia. Thermophysical analysis of the pre- and post-sampling spectra using the methods of [22] finds no notable change in thermal inertia within the Hokioi Crater. The post-sampling spectral changes observed at Nightingale therefore appear more attributable to exposure of fresh, organic-rich material than to particle size effects.

Properties of the collected sample

Mass

To estimate the mass of the collected sample, the spacecraft was programmed to hold an inertially fixed attitude while the TAGSAM arm moved, making it possible to measure the exchange of momentum between TAGSAM and the reaction wheels [53]. This activity was performed three times: before sampling (zero sample mass), 2 days after sampling (during SamCam verification imaging of TAGSAM), and 8 days after sampling, just before TAGSAM (with the sample inside) was stowed in its protective return capsule. This analysis yielded an estimated stowed sample mass of 250 ± 101 g.

However, the stowed mass is less than the mass initially collected. The SamCam verification images collected 2 days after sampling showed that TAGSAM was

packed with sample (indicated, for example, by a reduction in the average brightness of the chamber to just 1.5% of its pre-sampling value), but it was overflowing and losing particles (fig. S34) [10-§11.3]. Several pebbles with long axes up to 3 cm were visibly wedged into the chamber, propping open the mylar flap that was intended to prevent material from escaping (fig. S32). The escaping particles have a flake-like shape (fig. S36), consistent with the shape suggested for particles ejected from Bennu based on photometry and trajectory reconstruction [54,55].

We tracked 1804 individual particles leaving TAGSAM in the SamCam verification images [10-§11.3]. Each particle was observed in at least three images, allowing for their trajectories to be estimated and traced back to TAGSAM following methods developed for Bennu's particle ejection events [56]. The images were taken over the course of nine different articulations of the TAGSAM wrist motor (fig. S34), each documented with SamCam images of increasing exposure times. The median estimated range from the camera to the particles at the time of their first observation was 2.4 m, and the median estimated particle velocity was 0.8 cm s^{-1}. We observed the largest number of particles (560, or 31% of all observed particles) leaving just after the first movement of the wrist (fig. S34A). Fewer escaping particles were observed with each successive wrist movement (figs. S34B-H) until it reversed direction, at which point the number of escaping particles increased (fig. S34I).

We estimated the size and mass of each tracked particle photometrically by using the 3D trajectories to determine range and phase angle (fig. S35). We observed a minimum estimated 54.78 g of material leaving TAGSAM, with a mean particle mass of 0.03 g, and an average mass loss rate of 2.21 g min^{-1} between the first wrist movement and the last image. Particle long dimensions ranged from 0.004 to 23 mm, with a mean of 0.92 mm. The tracked particles are only a fraction of the total particles in the images, which in turn are likely only a fraction of the total particles that escaped. Thus, these results represent a lower bound on the total mass loss. The momentum transfer analysis described above [53] estimated a loss of 67 g of sample between the SamCam verification imaging and stowage, implying that TAGSAM contained 317 ± 101 g at the time of the verification imaging. This is consistent with the predicted sampled mass of 252–575 g based on empirical formulations of TAGSAM performance given the observed sampling conditions [24].

The total stowed mass includes not only the sample inside the chamber but also particles adhering to the 24 stainless steel contact pads on the baseplate of TAGSAM. In post-sampling images taken by SamCam and StowCam, we observed a total of 23 particles, up to 4 mm in diameter, clinging to the contact pads (fig. S37) [10-§11.2]. These illuminated images proved useful in identifying unresolved particles: The pattern of specular and diffuse reflection on each pad repeated itself faithfully in the absence of captured particles, which changed the pattern of light and dark. In addition, >260 sub-millimeter particles adhered directly to baseplate surface areas other than the pads or were trapped between the assembly screws and the walls of their countersinks (fig. S33). Given the evidence of sub-millimeter dust mobilized by the sampling event, we infer that such a population of smaller particles is also trapped in the pads.

Size-frequency distribution

We measured the diameters (D) of particles emplaced on the top plate of TAGSAM, using its known diameter (30.5 cm) as a scale, to a completeness limit of 0.2 cm and obtained their SFD as an approximation for that of the captured sample [10-§12]. The obtained SFD follows a power law with a cumulative exponent of -2.2 ± 0.1 for $0.2 \leq D \leq 2$ cm. This value is consistent, within

its uncertainties, with the power-law index of –2.2 measured at Nightingale before sampling for the size range 0.4 cm to 1.51 m [14].

We also measured the size of moving particles in the debris curtain kicked up by sampling by comparing several consecutive NavCam 2 images (fig. S39). From these data, we obtained an SFD that follows a power law from 2.5 cm to 30 cm, adjacent to the size range measured for the TAGSAM particles. The power-law indices of the SFD for the ejecta curtain particles are –3.6 to –3.9 for $D > 10$ cm and –2.7 to –3.3 for 2.5 cm $< D < 10$ cm. This observation suggests that the material mobilized by sampling contained a higher proportion of finer particulates. However, given the observations of particles disrupted by collisions with TAGSAM and other particles, the SFD of the sample after delivery to Earth in 2023 may not reflect that of the sampling location or of the initially collected sample. Nevertheless, the hundreds of grams of mass will provide the opportunity to test many of the hypotheses developed from remote sensing.

References and Notes

1. Lauretta, D. S., H. L. Enos, A. T. Polit, H. L. Roper, C. W. V. Wolner. OSIRIS-REx at Bennu: Overcoming challenges to collect a sample of the early Solar System. In Sample Return Missions, ed. A. Longobardo (Elsevier), pp. 163–194 (2021).

2. Scheeres, D. J., et al. Heterogeneous mass distribution of the rubble-pile asteroid (101955) Bennu. Science Advances 6, eabc3350 (2020).

3. Lauretta, D. S., and DellaGiustina D. N., et al. The unexpected surface of asteroid (101955) Bennu. Nature 568, 55–60 (2019).

4. Bierhaus, E. B., et al. The OSIRIS-REx spacecraft and the touch-and-go sample acquisition mechanism (TAGSAM). Space Science Reviews 214.7, Article number: 107, 1-46 (2018).

5. Rizk, B., et al. OCAMS: the OSIRIS-REx Camera Suite. Space Science Reviews 214, 26 (2018).

6. Golish, D. R., Drouet d'Aubigny, C., Rizk, B., et al. Ground and In-Flight Calibration of the OSIRIS-REx Camera Suite. Space Science Reviews 216, 12 (2020).

7. Bos, B. J., et al. Touch and Go Camera System (TAGCAMS) for the OSIRIS-REx asteroid sample return mission. Space Science Reviews 214, 37 (2018).

8. Bos, B.J., Nelson, D.S., Pelgrift, J.Y. et al. In-Flight Calibration and Performance of the OSIRIS-REx Touch and Go Camera System (TAGCAMS). Space Science Reviews 216, 71 (2020).

9. Christensen, P. R., et al. The OSIRIS-REx thermal emission spectrometer (OTES) instrument. Space Science Reviews 214.5, Article number: 87, 1-39 (2018).

10. Supplement to this manuscript

11. Lauretta, D.S., et al. OSIRIS-REx: Sample Return from Asteroid (101955) Bennu. Space Science Review. 212, 925–984 (2017).

12. Reuter, D. C., et al. The OSIRIS-REx Visible and InfraRed Spectrometer (OVIRS): spectral maps of the asteroid Bennu. Space Science Reviews 214.2 (2018): 1-22.

13. Berry, Kevin, et al. Revisiting OSIRIS-REx Touch-and-Go (TAG) Performance Given the Realities of Asteroid Bennu. *AAS Guidance, Navigation, and Control conference*. 2020.

14. Burke, K. N., et al. Particle Size-Frequency Distributions of the OSIRIS-REx Candidate Sample Sites on Asteroid (101955) Bennu. Remote Sensing 13, 1315 (2021).

15. Bierhaus, E. B., et al. Bennu regolith mobilized by TAGSAM: Expectations for the OSIRIS-REx sample collection event and application to understanding naturally ejected particles. Icarus 355, 114142 (2021).

16. Hamilton, V. E., et al. Evidence for widespread hydrated minerals on asteroid (101955) Bennu. Nature Astronomy 3, 332–340 (2019).

17. Hamilton, V.E., et al. Evidence for limited compositional and particle size variation on asteroid (101955) Bennu from thermal infrared spectroscopy. Astron. Astrophys. 650 A120 (2021).

18. Simon, A. A., et al. Widespread carbon-bearing materials on near-Earth asteroid (101955) Bennu. Science 370, (2020a).

19. DellaGiustina, D. N., et al. Variations in color and reflectance on the surface of asteroid (101955) Bennu. Science 370, eabc3660 (2020).

20. Simon, A. A., et al. Weak spectral features on (101995) Bennu from the OSIRIS-REx Visible and InfraRed Spectrometer. Astronomy & Astrophysics 644, A148 (2020b).

21. Kaplan, H. H., et al. Bright carbonate veins on asteroid (101955) Bennu: Implications for aqueous alteration history Science 370.6517 (2020).

22. Rozitis, B., et al. Asteroid (101955) Bennu's weak boulders and thermally anomalous equator. Science Advances 6, eabc3699 (2020).

23. Rozitis, B., et al. Implications for ice stability and particle ejection from high-resolution temperature modeling of asteroid (101955) Bennu. Journal of Geophysical Research: Planets 125.8 (2020): e2019JE006323.

24. Walsh, K. J. et al. Near-zero cohesion and loose packing of Bennu's near-subsurface revealed by spacecraft contact. Submitted to Science (companion paper).

25. Ballouz, R. Numerical simulations of granular physics in the solar system. Thesis, University of Maryland, College Park, 2017.

26. Ballouz, R. Modified granular impact force laws for the OSIRIS-REx touchdown on the surface of asteroid (101955) Bennu, Monthly Notices of the Royal Astronomical Society Main Journal (accepted) ref. MN-21-2051-MJ.R2.

27. Murdoch, N., et al. Low-velocity impacts into granular material: application to small-body landing. Monthly Notices of the Royal Astronomical Society 503, 3460–3471 (2021).

28. Ballouz, R-L., et al. Bennu's near-Earth lifetime of 1.75 million years inferred from craters on its boulders. Nature 587, 205–209 (2020).

29. Lauretta, D. S., and Hergenrother C. W., et al. Episodes of particle ejection from the surface of the active asteroid (101955) Bennu. Science 366.6470 (2019).

30. Hergenrother, C. W., et al. "Introduction to the special issue: exploration of the activity of asteroid (101955) Bennu." Journal of Geophysical Research: Planets 125.9 (2020): e2020JE006549.

31. DellaGiustina, D.N. and Emery, J.P. et al. Properties of rubble-pile asteroid (101955) Bennu from OSIRIS-REx imaging and thermal analysis. Nature Astronomy 3, 341–351 (2019).

32. Ruff, S.W., Christensen, P.R., Blaney, D.L., Farrand, W.H., Johnson, J.R., Michalski, J.R., Moersch, J.E., Wright, S.P. and Squyres, S.W. The rocks of Gusev Crater as viewed by the Mini-TES instrument. J. Geophys. Res. 111, doi:10.1029/2006JE002747 (2006).

33. Grevesse, N., M. Asplund, and J. Sauval. The solar chemical composition. Space Science Reviews 130, 105–114 (2007).

34. Hanna, R. D., et al. Distinguishing relative aqueous alteration and heating among CM chondrites with IR spectroscopy. Icarus 346, 113760 (2020).

35. Gaskell, R. W., et al. Characterizing and navigating small bodies with imaging data. Meteoritics & Planetary Science 43.6 (2008): 1049-1061.

36. Barnouin, O.S. et al. Shape of (101955) Bennu indicative of a rubble pile with internal stiffness. Nature Geoscience 12 247–252 (2019).

37. Barnouin, O. S., et al. Digital terrain mapping by the OSIRIS-REx mission. Planetary and Space Science 180 (2020): 104764.

38. Daly, M. G., et al. The OSIRIS-REx laser altimeter (OLA) investigation and instrument. Space Science Reviews 212.1 (2017): 899-924.

39. Daly, M. G., et al. Hemispherical differences in the shape and topography of asteroid (101955) Bennu. Science Advances 6, eabd3649 (2020).

40. Bierhaus, E. B. et al. Bennu's crater size-frequency distribution reveals impact armoring and young surface age. Nature Geosciences (submitted).

41. Iverson, R.M., Reid, M.E., LaHusen, R.G. Debris-flow mobilization from landslides. Annual Review of Earth and Planetary Sciences 25.1, 85–138 (1997).

42. Perera, V. et al. The spherical Brazil Nut Effect and its significance to asteroids. Icarus, 278, 194–203 (2016).

43. Aschauer, J., Kenkmann, T., 2017. Impact cratering on slopes. Icarus 290, 89–95 (2017).

44. Hayashi, K. Sumita, I. Low-velocity impact cratering experiments in granular slopes. Icarus 291, 160–175 (2017).

45. Daly, R.T. et al., 2021. The JHUAPL Planetary Impact Lab (PIL): Capabilities and initial results. Hypervelocity Impact Symposium. Vol. 883556. American Society of Mechanical Engineers, (2019).

46. Holsapple, K. A. The scaling of impact processes in planetary sciences. Annual review of earth and planetary sciences 21, 333–373 (1993).

47. Housen, K. R., K. A. Holsapple. Ejecta from impact craters. Icarus 211, 856–875 (2011).

48. Housen, K.R., Schmidt, R.M., Holsapple, K.A. Crater ejecta scaling laws - Fundamental forms based on dimensional analysis. Journal of Geophysical Research 88, 2485–2499 (1983).

49. Trang, D., et al. The Role of Hydrated Minerals and Space Weathering Products in the Bluing of Carbonaceous Asteroids. The Planetary Science Journal 2, 68 (2021).

50. Izawa, M. R. M., et al. Spectral reflectance properties of magnetites: Implications for remote sensing. Icarus 319, 525–539 (2019).

51. Johnson, T. V., F. P. Fanale. Optical properties of carbonaceous chondrites and their relationship to asteroids. Journal of Geophysical Research 78, 8507–8518 (1973).

52. Sen, Antara, et al. Spectral effects of varying texture and composition in two-component "mudpie" simulations: Insights for asteroid (101955) Bennu. Meteoritics & Planetary Science 56.6 (2021): 1173-1190.

53. Ma, H. et al., Alternative Sample Mass Measurement Technique for OSIRIS-REx Sample Collection Phase. In preparation.

54. Hergenrother, C. W., et al. Photometry of particles ejected from active asteroid (101955) Bennu. Journal of Geophysical Research: Planets 125.9 (2020): e2020JE006381.

55. Chesley, S. R., et al. Trajectory estimation for particles observed in the vicinity of (101955) Bennu. Journal of Geophysical Research: Planets 125, e2019JE006363 (2020).

56. Pelgrift, J. Y., et al. Reconstruction of Bennu Particle Events from Sparse Data. Journal of Geophysical Research: Planets 125, e2019EA000938 (2020).

57. Rizk, B.; Drouet d'Aubigny, C.; Golish, D.; DellaGiustina, D.N.; Lauretta, D.S. OSIRIS-REx Camera Suite (OCAMS) Bundle. Identifier (LID) urn:nasa:pds:orex.ocams Version 10.0.

58. Bos, B.; Adam, C.; and Lauretta, D.S. OSIRIS-REx TAGCAMS Bundle. Identifier (LID) urn:nasa:pds:orex.tagcams Version 10.0.

59. Christensen, P; Hamilton, V.; Anwar, S.; Mehall, G.; Lauretta, D. OSIRIS-REx Thermal Emission Spectrometer (OTES) Bundle. Identifier (LID) urn:nasa:pds:orex.otes Version 10.0.

60. Reuter, D.C.; Simon, A.A.; Lunsford, A.; Cosentino, R.; Gorius, N.; Lauretta, D. OSIRIS-REx OVIRS Bundle. Identifier (LID) urn:nasa:pds:orex.ovirs Version 10.0.

61. Daly, M.; Barnouin, O.; Espiritu, R.; Lauretta, D. OSIRIS Laser Altimeter (OLA) Bundle. Identifier (LID) urn:nasa:pds:orex.ola Version 3.0.

62. Williams, B., et al. OSIRIS-REx flight dynamics and navigation design. Space Science Reviews 214.4, Article number: 69, 1-33 (2018).

63. https://naif.jpl.nasa.gov/pub/naif/toolkit_docs/C/req/pck.html

64. Golish, D. R., et al. Disk-resolved photometric modeling and properties of asteroid (101955) Bennu. Icarus 357 113724 (2021a).

65. Hog, E., Fabricius, C., Makarov, V., Urban, S., Corbin, T., Wycoff, G., & Wicenec, A. The Tycho-2 catalogue of the 2.5 million brightest stars. Astronomy & Astrophysics 2, L27- L30 (2000).

66. Zacharias, N., Finch, C., Girard, T., Henden, A., Bartlett, J., Monet, D., Zacharias, M. The Fourth US Naval Observatory CCD astrograph catalog (UCAC4). The Astronomical Journal, 145, 44 (2013).

67. Liounis, A. J., Swenson, J. C., Small, J., Lyzhoft, J., Ashman, B. W., Getzandanner, K. M., & Lauretta, D. S. (2019). Independent optical navigation processing for the OSIRIS-REx mission using the Goddard image analysis and navigation tool. 2nd RPI Space Imaging Workshop, Saratoga Springs, NY, (2019).

68. Liounis, A. J., Small, J. L., Swenson, J. C., Lyzhoft, J. R., Ashman, B. W., & Getzandanner, K. M., et al. Autonomous detection of particles and tracks in optical images. Earth and Space Science 7, e2019EA000843 (2020).

69. Smith, M.D., Wolff, M.J., Spanovich, N., Ghosh, A., Banfield, D., Christensen, P.R., Landis, G.A. and Squyres, S.W. One Martian year of atmospheric observations using MER Mini-TES. J. Geophys. Res. 111, doi:10.1029/2006JE002770 (2006).

70. Al Asad, M.M. et al. Validation of Stereophotoclinometric Shape Models of Asteroid (101955) Bennu during the OSIRIS-REx Mission. The Planetary Science Journal 2, doi:10.3847/PSJ/abe4dc (2021).

71. Gault, D.E. & Wedekind, J.A. Experimental hypervelocity impact into quartz sand - II: Effects of gravitational acceleration. In: Impact and explosion cratering. Planetary and

terrestrial implications (Roddy, D. J., Pepin, R. O., and Merrill, R. B., editors) Pergamon Press (New York). pp. 1231-1244 (1977).

72. Schmidt, R.M. Meteor Crater: Energy of formation - Implications of centrifuge scaling. In: Lunar and Planetary Science Conference 11, 2099-2128 (1980).

73. Schultz, P.H. & Gault, D.E. Clustered impacts - Experiments and implications. Journal of Geophysical Research 90, 3701-3732 (1985).

74. Barnouin-Jha, O.S. et al. Non-intrusive measurements of crater growth. Icarus 188, 506-521 (2007).

75. Schröder, S.E. et al. The Boulder Population of Asteroid 4 Vesta: Size-Frequency Distribution and Survival Time. Earth Space Sci. 8, 000941 (2021).

76. Pajola, M. et al. Blocks Size Frequency Distribution in the Enceladus Tiger Stripes Area: Implications on Their Formative Processes. Universe 7, 82 (2021).

77. Ernst, C. et al. The Small Body Mapping Tool (SBMT) for Accessing, Visualizing, and Analyzing Spacecraft Data in Three Dimensions. 49th Lunar and Planetary Science Conference, abstract no. 1043 (2018).

78. Clauset, A., C. R. Shalizi, M. E. J. Newman. Power-law distributions in empirical data. SIAM Review 51, 661-703 (2009).

79. Levesque, M., Martin P. Lelievre, Evaluation of the Iterative Method for Image Background Removal in Astronomical Images. Defence Research and Development Canada Valcartier (Quebec), 2008.

80. Calinski, T., J. Harabasz. A dendrite method for cluster analysis. Communications in Statistics 3, 1-27 (1974).

81. Arthur, D., S. Vassilvitskii. K-means++: The Advantages of Careful Seeding. SODA '07: Proceedings of the Eighteenth Annual ACM-SIAM Symposium on Discrete Algorithms Technical Report, Stanford Infolab, pp. 1027-1035 (2007).

82. Blackman, S. S. Multiple hypothesis tracking for multiple target tracking. IEEE Aerospace and Electronic Systems Magazine 19, 5-18 (2004).

Acknowledgments: The OSIRIS-REx sample collection was the culmination of years of effort by hundreds of team members. This “TAG Team” overcame substantial challenges to successfully collect abundant sample from Bennu.

Funding: The material presented here is based upon work supported by NASA under Contract NNM10AA11C issued through the New Frontiers Program. M. Pajola was supported for this research by the Italian Space Agency (ASI) under the ASI-INAF agreement no. 2017-37-H.0. S. Sugita was supported by the *International Network of Planetary Sciences* grant from the

Japanese Society for Promotion of Science (JSPS) Core-to-Core program. B. Rozitis acknowledges funding support from the UK Science and Technology Facilities Council (STFC).

Author contributions: DSL led the investigation and compiled, integrated, and interpreted the results, supported by CWVW. CDA led the investigation of escaping particles from TAGSAM supported by DSN, JYP, EMS, EJL-C, AJL, and LKM. CWH analyzed the shapes of particles escaping from TAGSAM and supported their photometric analysis. KJW led the evaluation of regolith properties supported by RLB. OSB led the altimetry investigation of the TAG crater supported by MGD and JAS. MGD is also the instrument scientist for OLA. DND led the image processing of OCAMS data supported by KJB, TB, CAB, DRG, CYDd'A, and BRi. CYDd'A, and BRi also serve as the OCAMS instrument scientists. EBB is the TAGSAM lead scientist. BJB is the TAGCAMS instrument scientist and lead the image processing of TAGCAMS data supported by JBG and MAR. RB and MCM are the project managers for the OSIRIS-REx mission. MP led the particle size frequency analysis of the final flyby data supported by HC, AA, and JN. SS performed the particle size frequency analysis of the TAGSAM head and the debris plume supported by YC, TM, NS, and KY. VEH led the spectral analysis of OTES data supported by PRC. PRC and VEH are the OTES instrument scientists. AAS led the spectral analysis of OVIRS data supported by BEC, HHK, and DCR. DCR and AAS are the OVIRS instrument scientists. HLE led the science operations team supported by ATP, MMW, and SHS. KG led the flight dynamics and navigation team supported by CDA, DSN, JYP, EMS, EJL-C, AJL, and LKM. LPK led the analysis of the contact pads supported by BRi. RO led the analysis of spacecraft momentum build up supported by HM, BDM, and MAS. SFK led the spacecraft operations team. ECAC was the TAG lead system engineer. BRo led the thermal analysis, supported by AJR and JPE. HCCJr serves as the mission sample scientist and supported interpretation of the collected sample.

Competing interests: Authors declare that they have no competing interests.

Data and materials availability: OCAMS [57], TAGCAMS [58], OTES [59], OVIRS [60], and OLA [61] data from the sampling event and/or the final flyby have been submitted to the Planetary Data System and will be available before publication at https://sbn.psi.edu/pds/resource/orex/. The IDs of images, spectra, and scans used in this work are provided in table S10. This research has made use of the USGS Integrated Software for Imagers and Spectrometers (ISIS3), which is available from https://isis.astrogeology.usgs.gov. The stereophotoclinometry software used for producing the DTM is available at https://spc.psi.edu. The digital terrain analyses shown were undertaken with the JHUAPL Small Body Mapping Tool (SBMT). It is available for the analysis of a broad suite of asteroid and comet data at https://sbmt.jhuapl.edu. The DTMs produced for this work are also available at this site.

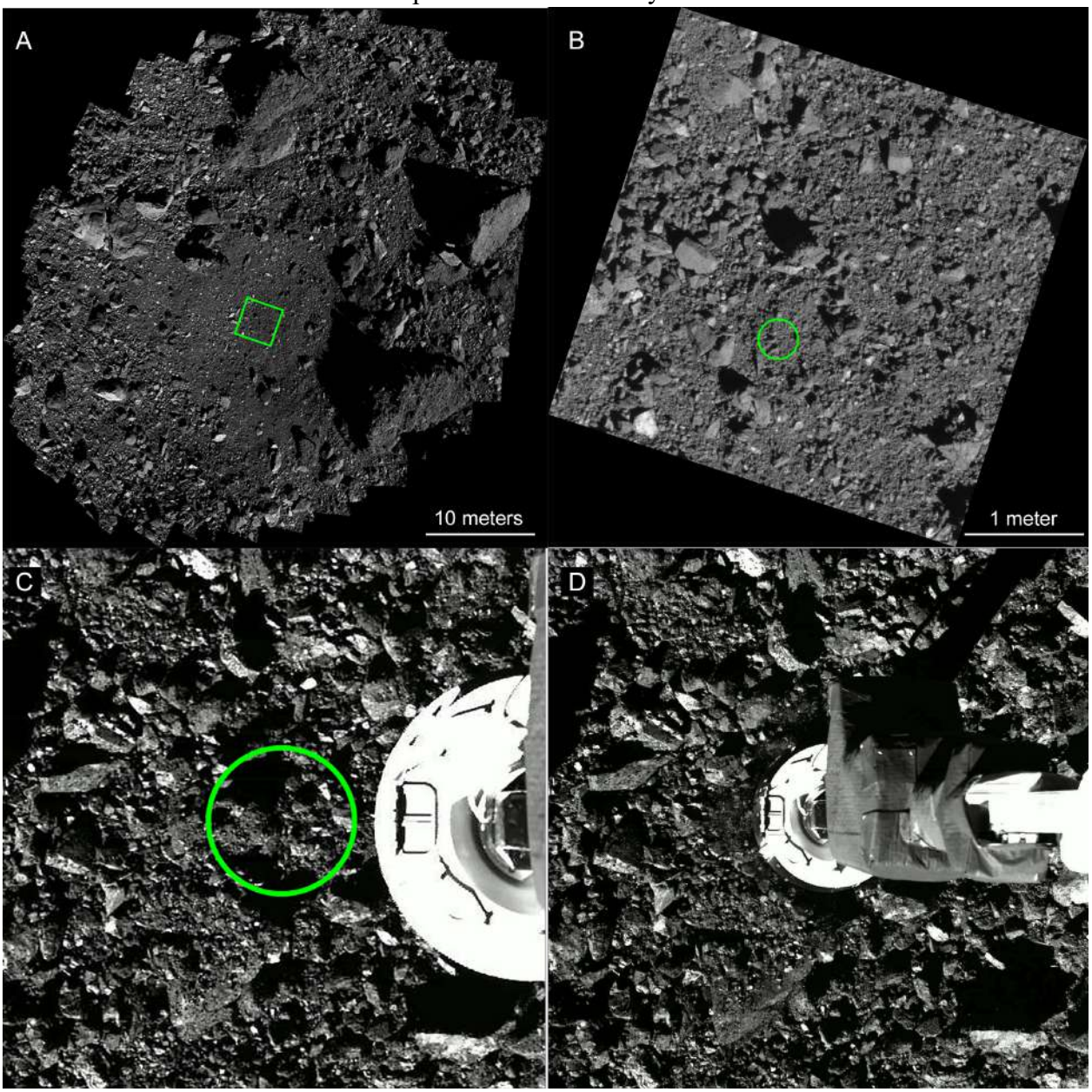

Figure 1. OCAMS provided photo documentation of the OSIRIS-REx sample site (**A**) Hokioi Crater, location of Nightingale, the sample collection site. Shown is a mosaic of PolyCam images taken on 3 March 2011 (Recon C) [1] with a pixel scale of 4 mm per pixel. The box indicates the area shown in (B). (**B**) PolyCam image showing a close-up of salt-and-pepper appearance of Hokioi Crater. PolyCam image taken 3 March 2020 with a pixel scale of 0.3 cm. The circle indicates where TAGAM contacted the surface to collect the sample. (**C**) Highest resolution image of the TAG point. Shown is a SamCam image collected 38 seconds prior to surface contact. The area where TAGSAM contacted is indicated with the green circle, which has a diameter of 32 cm. Image has been cropped to show the same field of view as in Fig. 1D. (**D**) TAGSAM contacting Bennu. Shown is a SamCam image collected after contact with the surface, 0.32 s prior to gas bottle firing. North is up in all images.

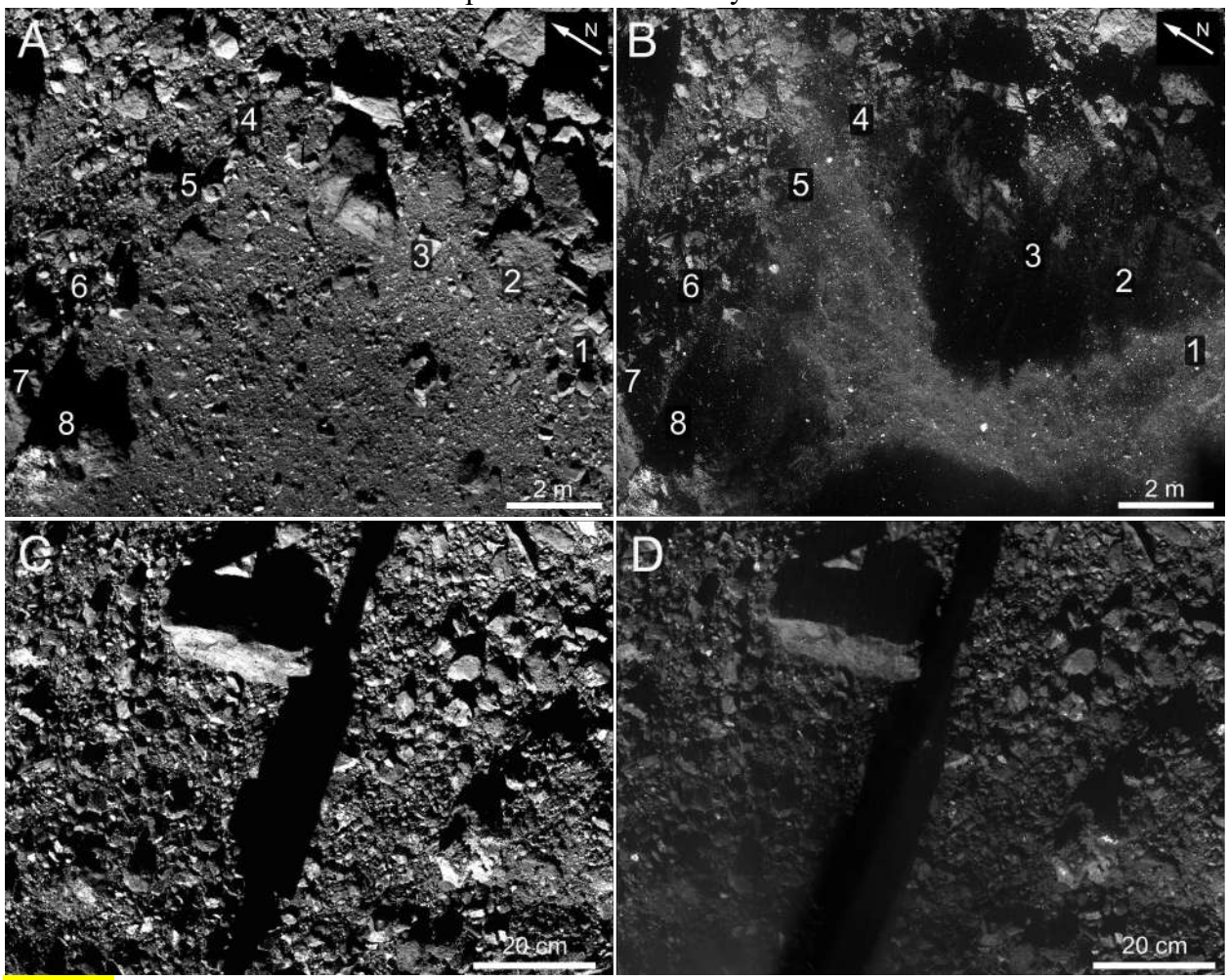

Figure 2. NavCam 2 images document the asteroid surface before and just after sampling on October 20, 2020. (**A**) Pre-contact, high-altitude NavCam2 image taken at 21:42:41 UTC. Yellow numerals indicate eight landmarks allows for comparison with the post-contact image to assess the extent of surface disturbance. Image has been cropped to show the same field of view as in (B). Image resolution is 15 mm per pixel (**B**) Post-contact, high-altitude NavCam2 image taken at 21:51:13 UTC, same landmarks as in (A). The yellow line traces the extent of surface disturbance. Image resolution is 9 mm per pixel (**C**) NavCam2 image taken right before surface contact at 21:49:49 UTC. The shadow of the TAGSAM arm runs through the middle of the image. Image resolution is 1 mm per pixel (**D**) Post-contact NavCam2 image dust taken at 21:49:50 UTC, with the same field of view as in (C), showing a cloud of sub-millimeter dust emanating from the TAG point. Image resolution is 1 mm per pixel.

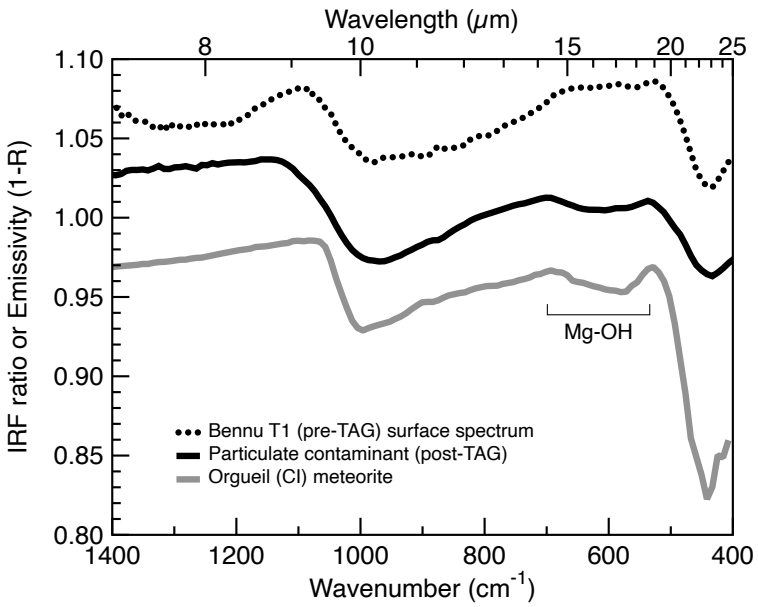

Figure 3. **OTES spectra reveal the composition of the sub-mm dust from Bennu's subsurface.** Plot showing an example Bennu surface type (T1) spectrum prior to TAG [17], particulate contaminant on instrument post-TAG (IRF ratio), and a representative carbonaceous meteorite, the Orgueil CI chondrite [17]. Spectra are offset vertically for clarity; the Bennu T1 spectrum is shown at 300% contrast to enable comparison of spectral features. The meteorite exhibits a small Mg-OH absorption from ~700-535 cm^{-1} (~14.3 – 18.7 μm) that is common to aqueously altered, phyllosilicate-rich CI and CM chondrites but has been difficult to distinguish in Bennu surface spectra.

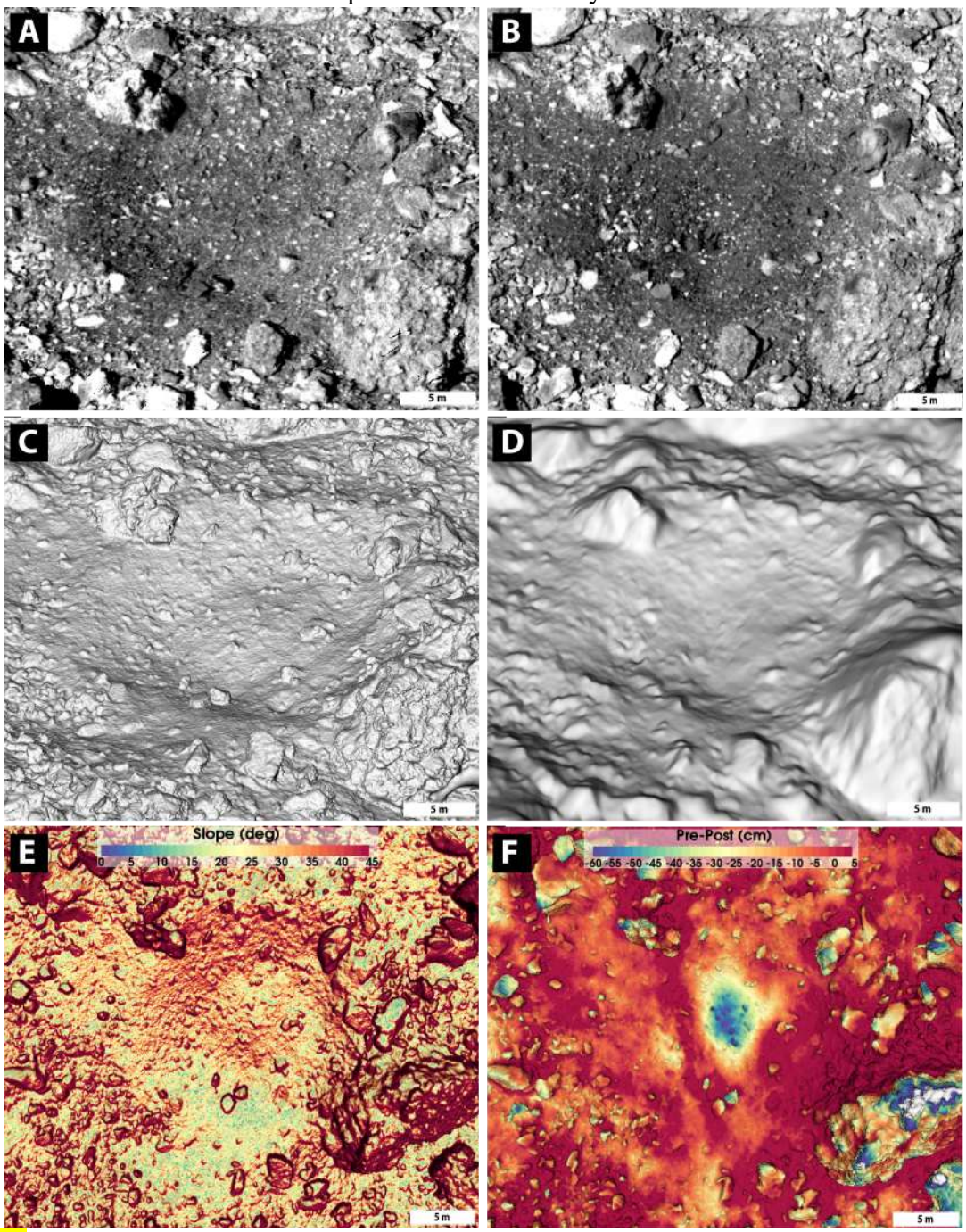

Figure 4. Images and altimetry products reveal the extent of surface changes from sampling. (A) Pre-sampling image collected on 7 March 2019. (B) Post-sampling image collected on 7 April 2021 (final flyby). These images have a pixel scale of about 5 cm. (C) Pre-sampling DTM based on OLA data, with a ground sample distance of 5 cm. (D) Post-sampling DTM constructed using stereophotoclinometry, with a ground sample distance of 5 cm. The change in topography between (C) and (D) is relevant, whereas different surface textures in (C) and (D) are due to the different DTM construction approaches. (E) Pre-sampling slope map, based on the DTM and surface accelerations [2]. f) Difference between the pre- and post-sampling DTMs illustrating the newly formed TAG crater. Bennu north (+*z*) is up in all panels.

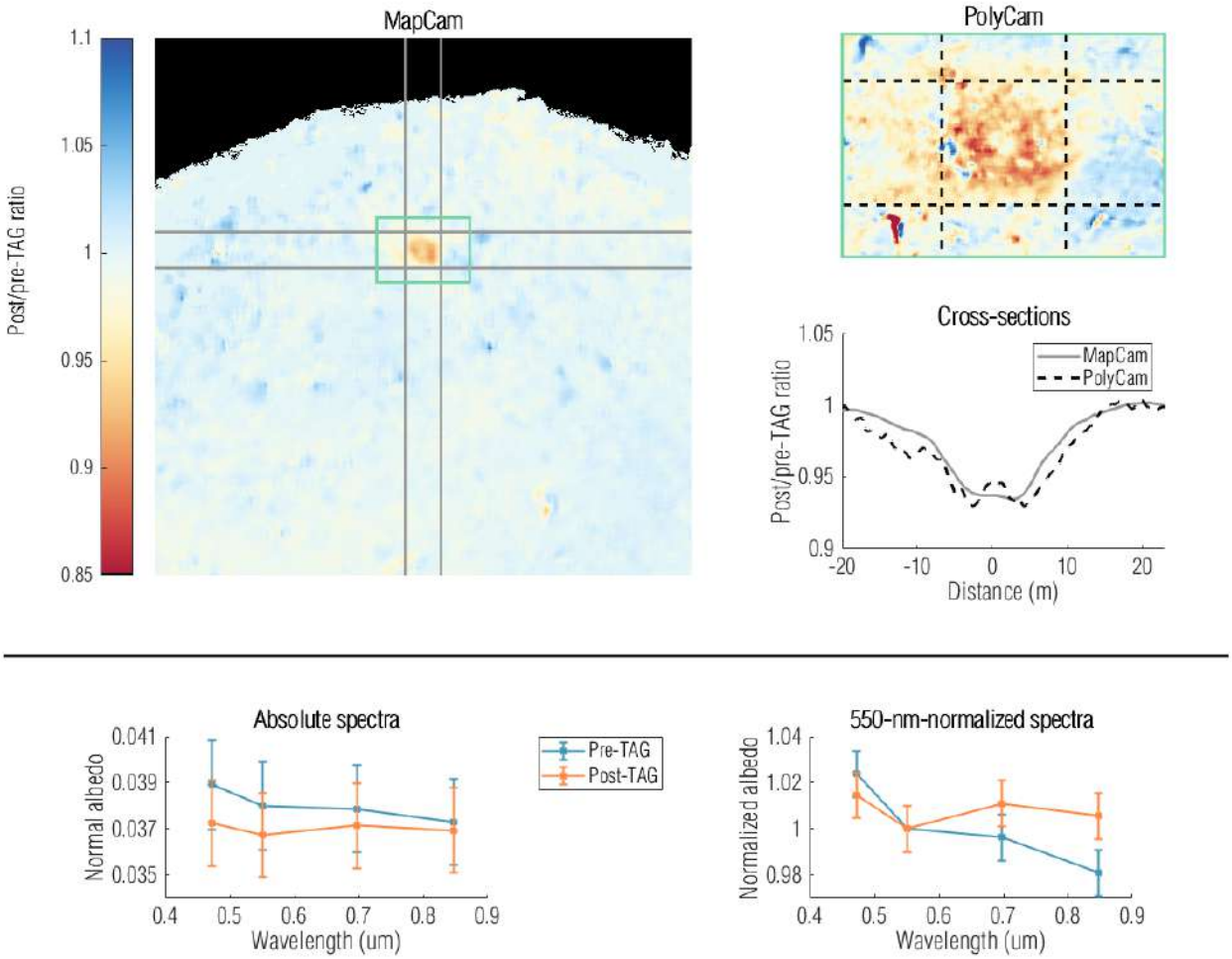

Figure 5. **OCAMS post-TAG images show changes in surface optical properties.** (A and B) Reflectance changes in MapCam (A) and PolyCam (B) data before and after sampling (TAG). (C) Plot of reflectance change in cross sections of Hokioi crater. (D) Absolute spectra from MapCam color filters. (E) Spectra normalized to 0.55 µm.

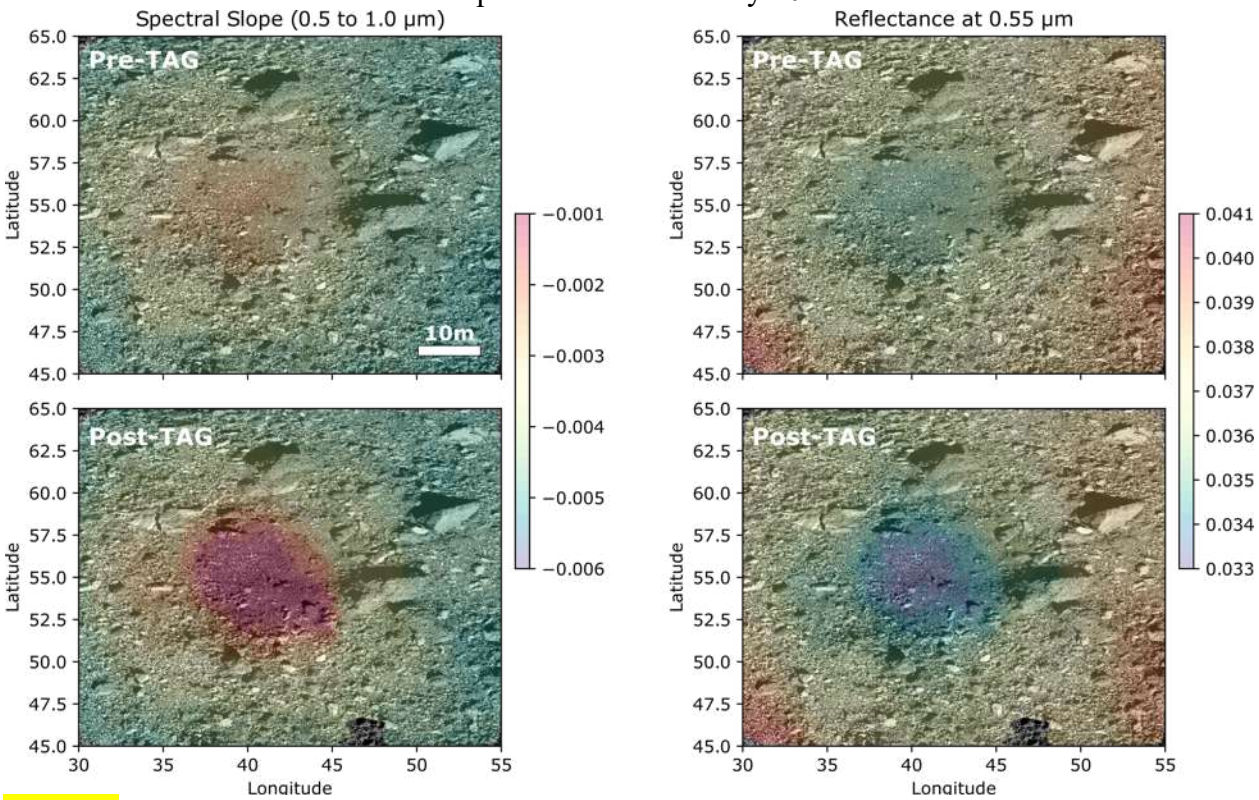

Figure 6. OVIRS spectra show the changes in spectral slope and reflectance resulting from sampling. (**A**) OVIRS spectral slope before sampling. (**B**) OVIRS reflectance at 0.55 μm before sampling. (**C** and **D**) Same as (A) and (B), but after sampling.

5

Supplementary Materials

The Subsurface of Bennu Excavated by OSIRIS-REx Sample Collection

Supplementary Information/Materials and Methods

1 SAMPLING OVERVIEW

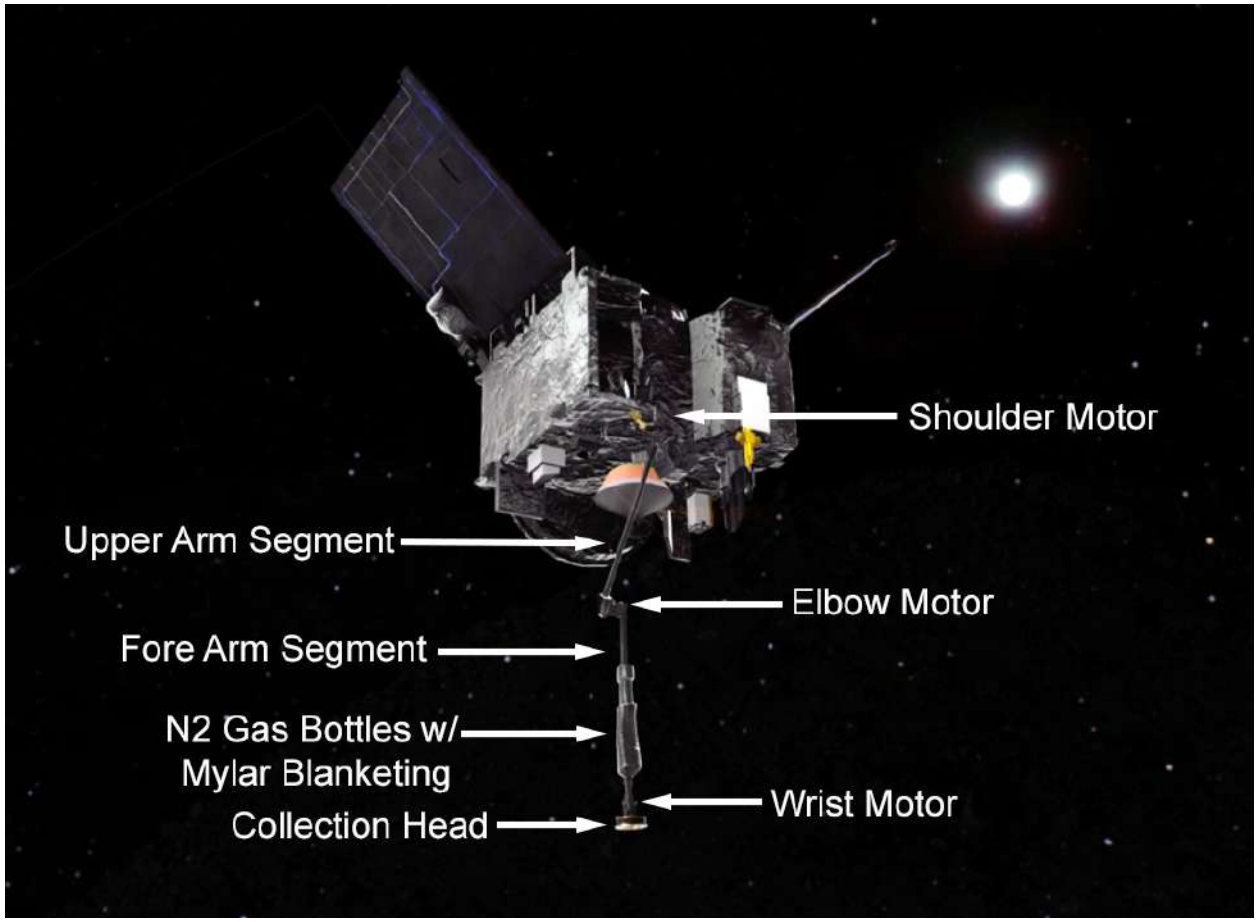

Figure S1. Illustration highlighting the major components of TAGSAM. TAGSAM acquired the bulk sample by releasing a jet of high-purity nitrogen gas that excites and "fluidizes" at least 60 g of regolith into the collection chamber. During the collection time, gas is injected into the surface and subsurface, mobilizing particles into the collection volume. The baseplate of TAGSAM contains 24 contact-pad samplers made of stainless-steel Velcro. These pads collect small particles up to 1 mm in diameter upon contact with the asteroid surface. Image Credit: NASA/Goddard/SVS/CI Lab.

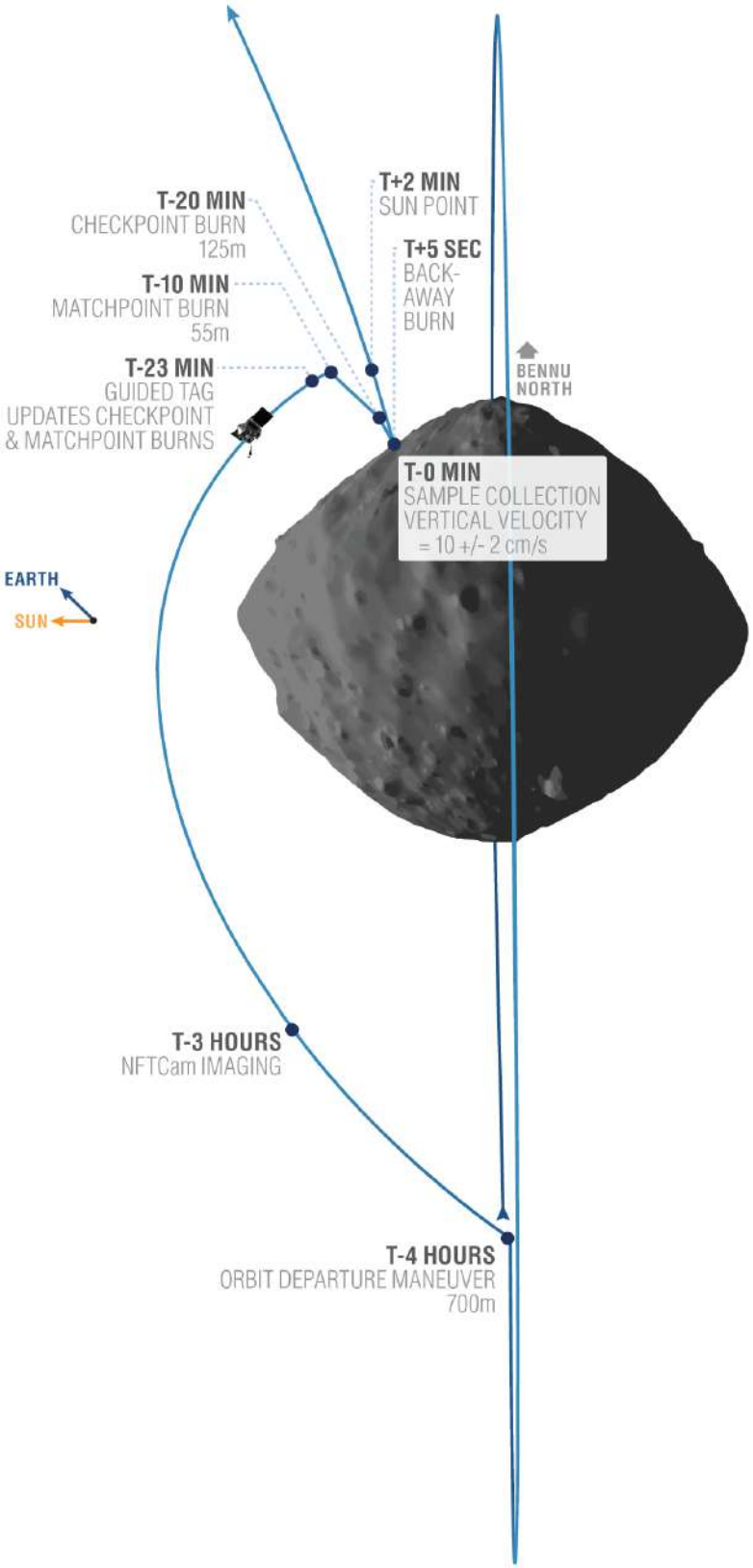

Figure S2. Diagram of the spacecraft trajectory and key events during sampling [1]. Credit: Lauretta et al. 2021.

2 BENNU FINAL FLYBY (BFF) OBSERVATIONS

The OSIRIS-REx spacecraft approached and flew by Bennu one final time on 7 April 2021. The goal of these Bennu Final Flyby (BFF) observations was to acquire a near-global dataset that allows asteroid surface change detection when compared to pre-sampling science observations from the global survey of Bennu (called the Detailed Survey). These data were also used to assess instrument performance degradation from sampling and instrument viability.

The mission's Flight Dynamics Team [62] designed a trajectory that imitates a hybrid of the Detailed Survey's Baseball Diamond Flybys 1 and 2 (FB1 and FB2) [1], with a FB1-like equatorial sub-spacecraft latitude and a 12:30pm local solar hour sub-spacecraft longitude and a FB2-like range to Bennu's center of mass of 3700 m. On this trajectory, the spacecraft performed nadir-pointed north-south linear scans that extended across Bennu's polar dimension plus navigation uncertainties, with PolyCam as the primary instrument and OTES, OVIRS, and OLA as secondary instruments (fig. S3A). Additionally, slews of MapCam color-filter images were interspersed throughout the observation at regular intervals (fig. S3B). The instruments observed for 1.4 Bennu rotation periods.

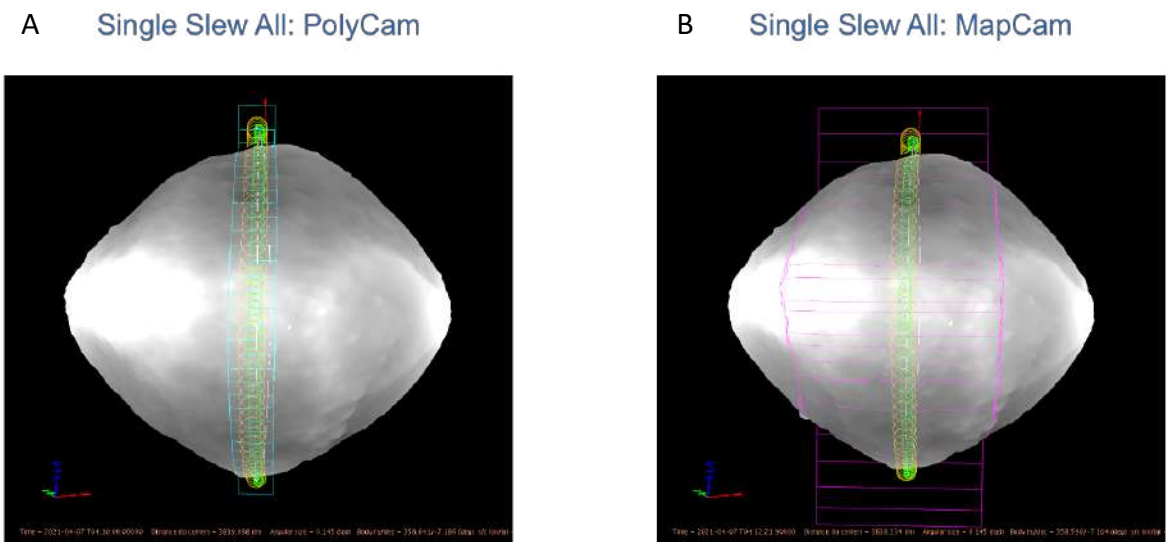

Figure S3. Demonstrations of single linear scans showing (**A**) PolyCam (aqua) and (**B**) MapCam (purple) footprints. OTES (orange) and OVIRS (green) footprints are shown in both figures.

Table S1. Viewing conditions for the linear scans.

North Slew (+40° to +90° latitude)

	Phase (°)	Incidence (°)	Emission (°)	LSH	Range to surface (m)
Minimum	9.18	47.57	48.98	8.787	3645
Maximum	12.62	92.56	101.2	15.67	3875

Mid Slew (-40° to +40° latitude)

	Phase (°)	Incidence (°)	Emission (°)	LSH	Range to surface (m)
Minimum	8.119	5.995	5.439	12.02	3530
Maximum	14.4	49.6	54.84	12.86	3700

South Slew (-90° to -40° latitude)

	Phase (°)	Incidence (°)	Emission (°)	LSH	Range to surface (m)
Minimum	7.662	42.82	47.89	9.51	3645
Maximum	15.28	87.08	92.92	14.22	3808

Table S2. Nightingale viewing conditions. While the observation was planned to obtain global coverage of Bennu, Nightingale was the area of highest priority for imaging and change detection.

Latitude (°)	Longitude (°)	Phase (°)	Incidence (°)	Emission (°)	LSH	Range to surface (m)
55.04	43.09	9.59	62.9	65.9	11.85	3725.5
57.04	42.89	9.60	64.7	67.8	11.84	3731.5
57.07	40.81	9.67	64.8	68.1	11.71	3732.2
55.21	40.95	9.66	63.1	66.4	11.71	3726.9

Table S3. Detailed observation parameters for the 5.9-hour (1.37 Bennu rotations) linear scanning duration.

Observation Date:	2021-04-07 (DOY097)
Observation Duration (# of Bennu Rotations):	5.9 hours (1.37 Bennu Rotations)
Range to Bennu COM:	3802-3866m
Observation Type:	Linear Scan (North-South scanning)
Spacecraft Pointing:	Nadir
Scan Range:	499m (Bennu polar diameter) + 2-sigma
Planning Radius:	249.5m (Bennu polar radius) + 2-sigma Nav. Uncert.
Slew Rotational Resolution:	3.3˚
PolyCam Imaging Cadence:	6.6˚ (every other slew)

PolyCam Across-Slew Overlap:	30-33% (near equator, increasing towards poles)
Number of PolyCam Images Per Slew:	16
Total Number of PolyCam Images:	1216 (regular); 20 (darks); 1236 (total)
MapCam Imaging Cadence:	19.8˚ (every 6 slews)
MapCam Across-Slew Overlap:	58-60% (near equator, increasing towards poles)
Number of MapCam Images Per Slew:	12 (3 color-sets minus the pan-filter)
MapCam Along-Slew Overlap:	73-91%
MapCam Along-Slew Filter Overlap:	~10-20% (based on visual inspection)
Total Number of MapCam Images:	300 (regular); 40 (dark); 340 (total)
Total Number of OCAMs Images:	1576
Spectrometer Imaging Cadence:	Continuous; same as slew rotational resolution (3.3˚)
OVIRS Across-Slew Overlap:	0% near the equator (~3.5m gores that decrease and close towards the poles)
OTES Across-Slew Overlap:	39-42% (near equator, increasing towards poles)

3 SPACECRAFT VELOCITY PROFILE

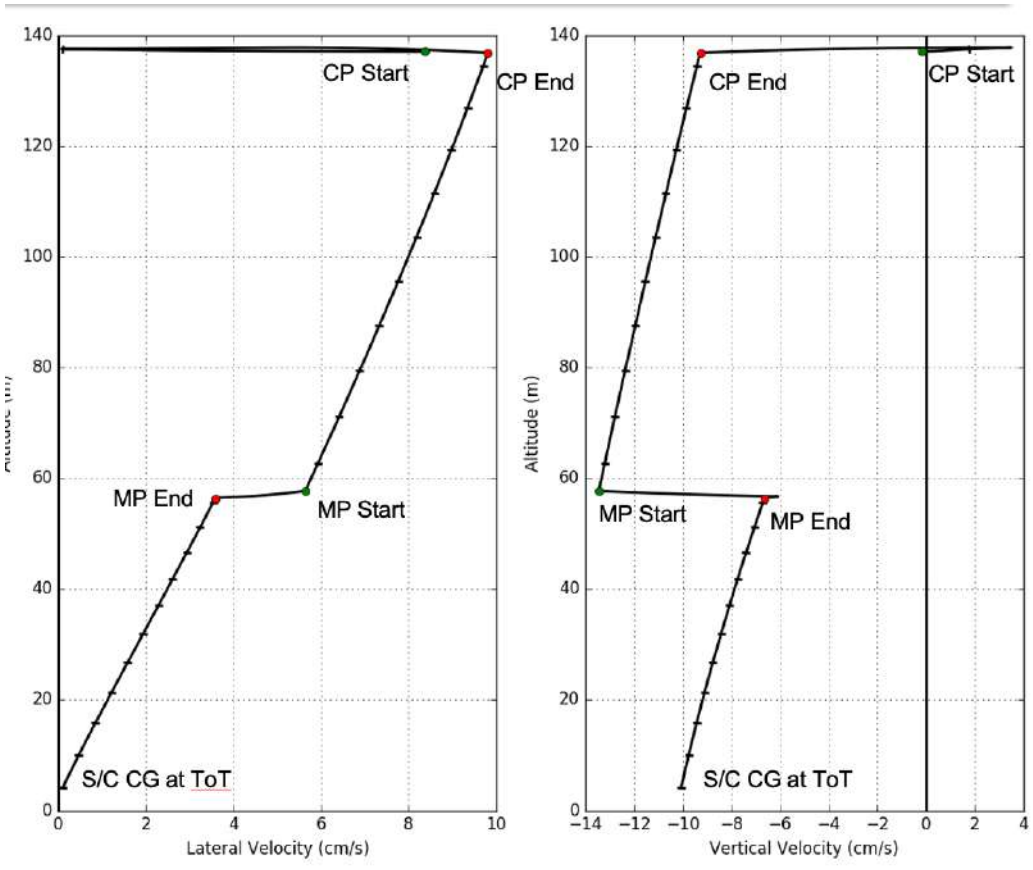

Figure S4. Diagrams of the spacecraft center of gravity (S/C CG) lateral and vertical velocity during the final stages of sampling. The propulsive maneuvers at the Checkpoint (CP) and Matchpoint (MP) were designed to achieve a lateral velocity of 0 cm s^{-1} and a vertical velocity of 10 cm s^{-1} at the time of touch (ToT).

4 Determination of Contact Point

To determine the point where TAGSAM contacted the surface of Bennu, we manually registered the SamCam image taken closest to the time of surface contact (image 20201020T214948S882) to the Recon C Nightingale mosaic (Fig. 1A) by matching landmarks in both images. We updated the mosaic's geometry using v20 of the OLA-based 5-cm shape model and version 16 of the Bennu Planetary Constants Kernel (PCK) [62], which were both more up to date than what was available when the Nightingale mosaic was first produced after the Recon C flyby. We used the center of the TAGSAM head, which was visible in the SamCam image, as the point of contact. Once the SamCam image was registered to the Nightingale mosaic, we located the point of the TAGSAM center in the mosaic and extracted the latitude and longitude coordinates.

5 Post-Contact Material Mobilization

5.1 SamCam Image Analysis

One second after contact, the TAGSAM gas valve opened, initiating gas flow, and lofting abundant sampleable material (fig. S5). This post-contact sequence of SamCam images shows that many particles kicked up by the disturbance were emplaced on the top of TAGSAM, allowing us to measure the SFD in each image (Supplement 12.1).

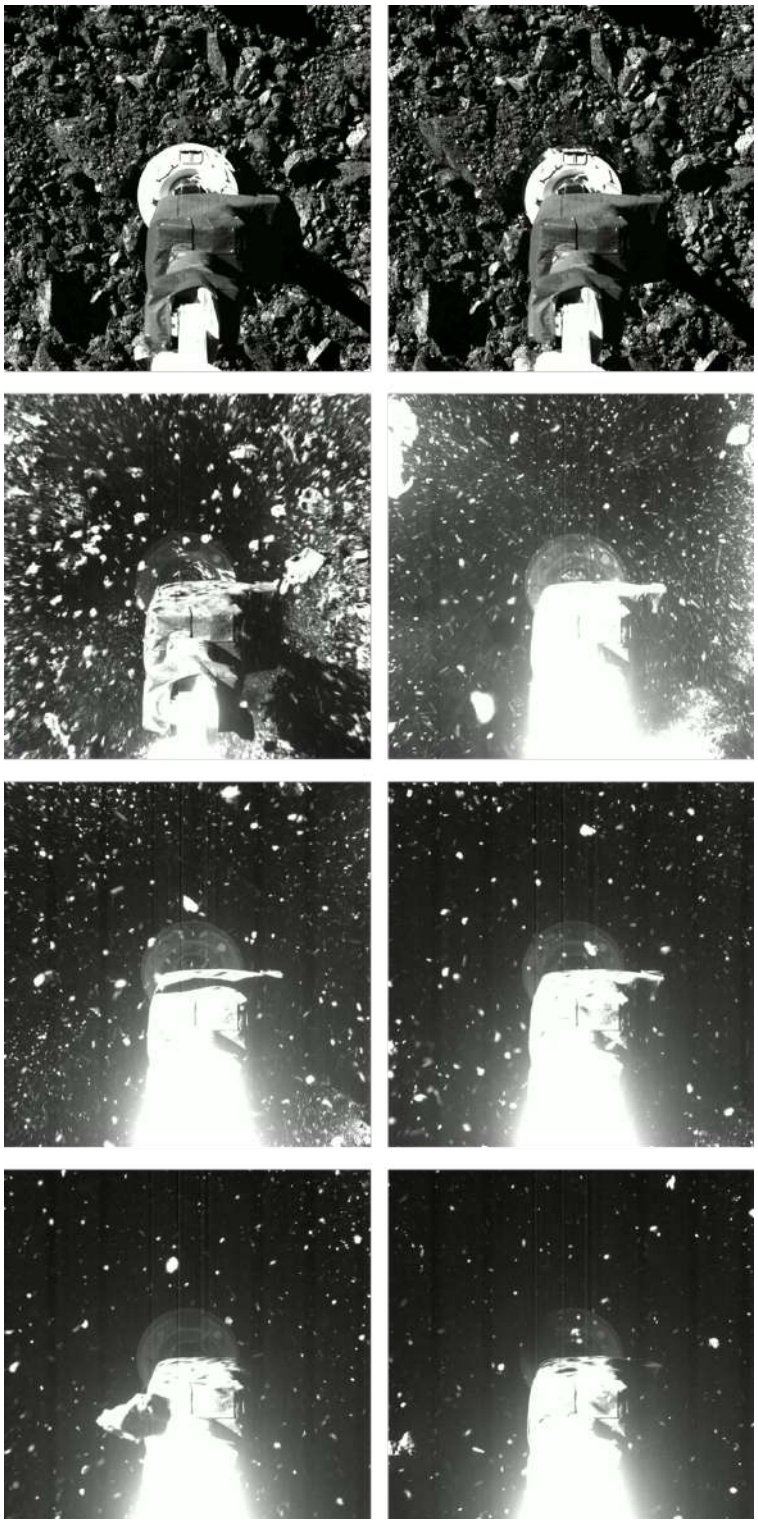

Figure S5. SamCam images demonstrating the TAGSAM interaction with Bennu during sample collection. Images were taken at 21:49:48, 21:49:50, 21:49:51, 21:49:52, 21:49:53, 21:49:54, 21:49:56, 21:49:57 UTC on 20 October 2020. The field of view in the starting image is about 2 m from corner to opposite corner. The pixel scale (assuming the original surface) changes by ~15% in these 9 seconds due to forward drift.

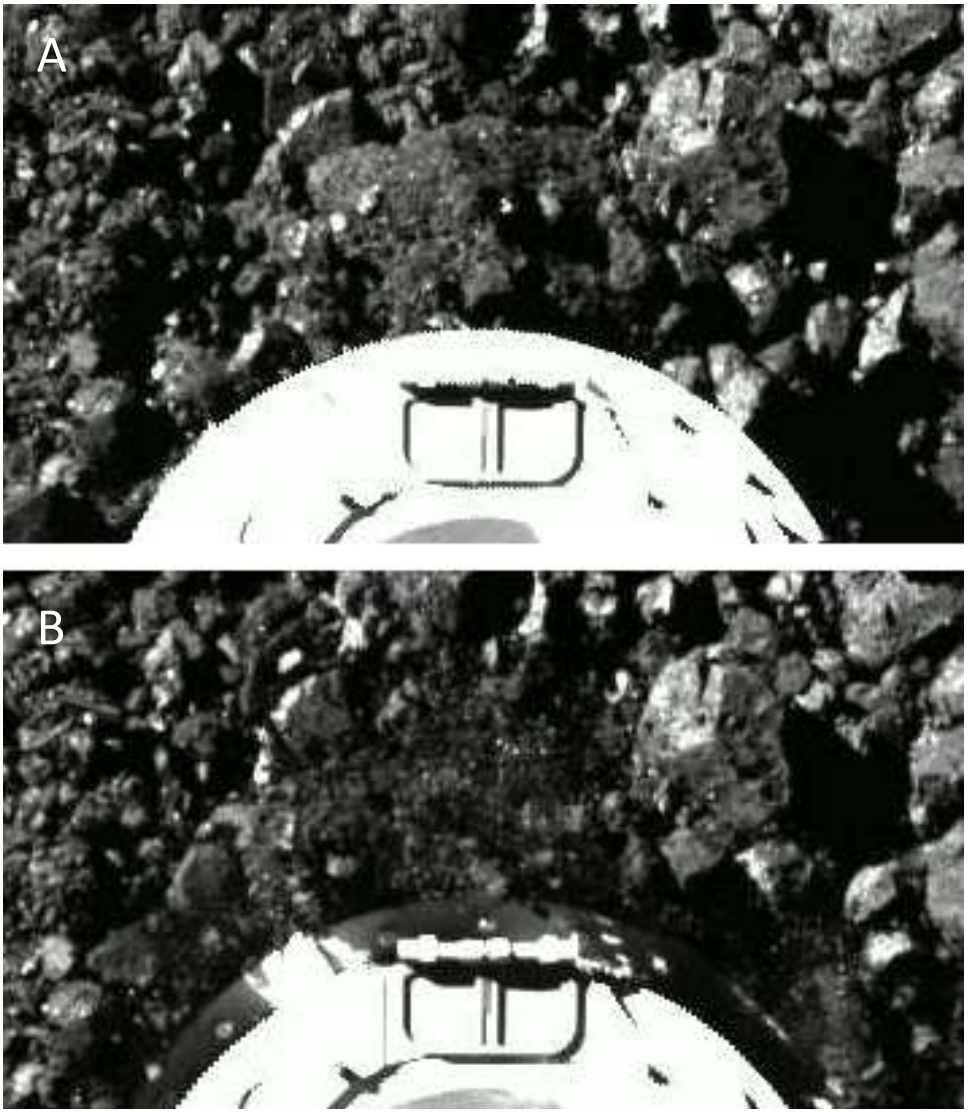

Figure S6. SamCam images demonstrating the TAGSAM interaction with Bennu right before (**A**) and right after (**B**) contact. Images are zoomed in on the boulder on the western edge of the TAGSAM head that was partially disaggregated as a result of surface contact. Disaggregated portions are most obvious where particles are present above the baseplate. Images were taken at 21:49:48 and 21:49:50 UTC on 20 October 2020. North is to the right of the image. For a blinking version see Movie S1.

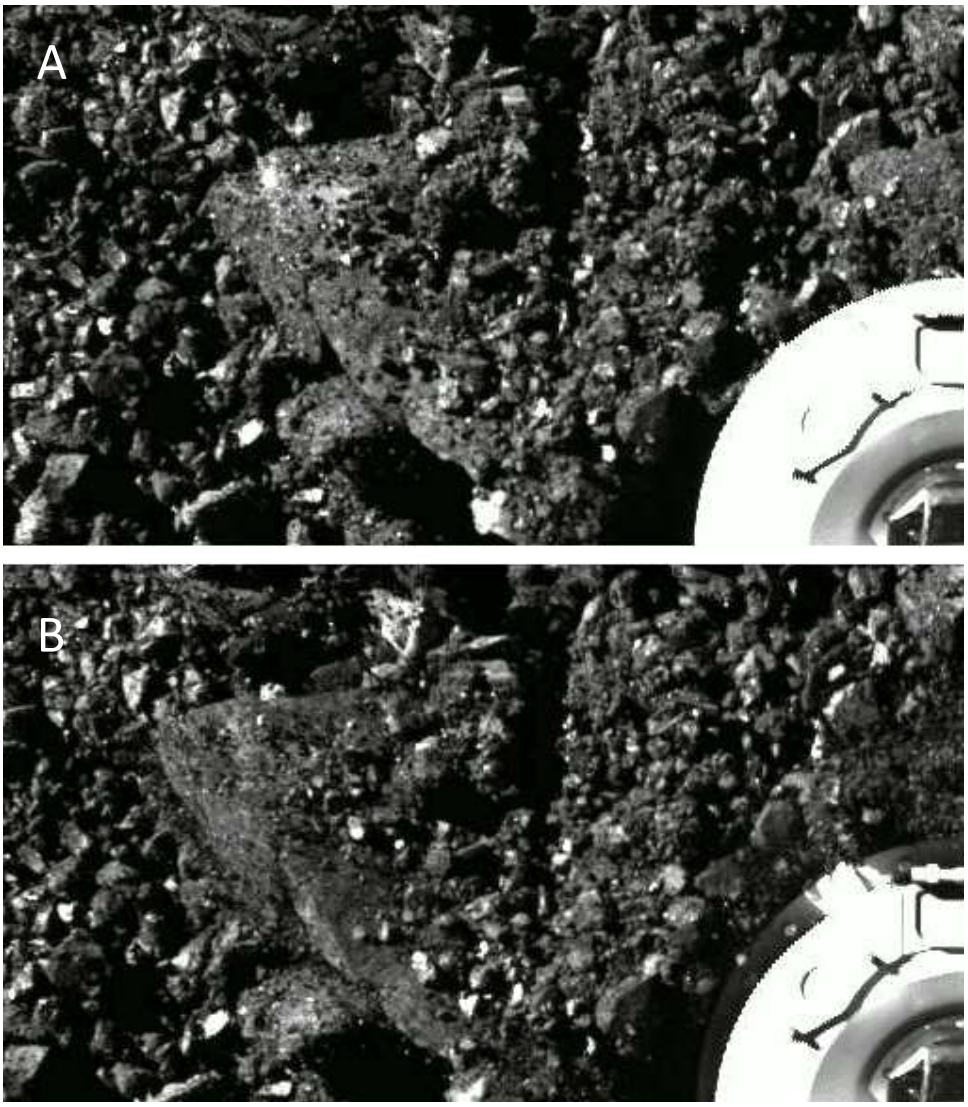

Figure S7. SamCam images demonstrating the TAGSAM interaction with Bennu right before (**A**) and right after (**B**) contact. Images are zoomed in on the boulder to the southwest of the contact point that was apparently flipped by TAGSAM during surface contact. Images were taken at 21:49:48 and 21:49:50 UTC on 20 October 2020. North is to the right of the image. For a blinking version see Movie S2.

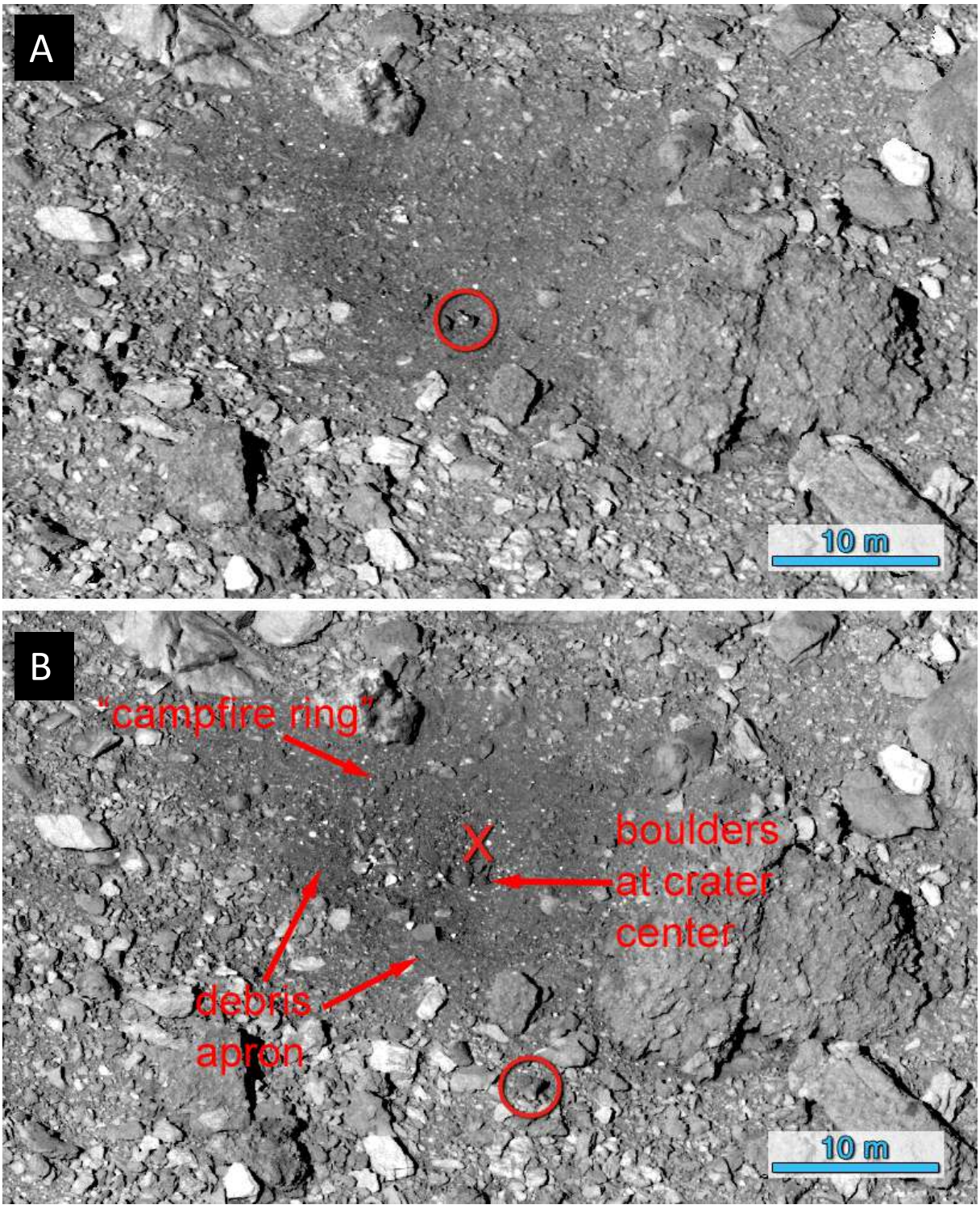

Figure S8. PolyCam images demonstrating the effects of sample collection. (**A**) Image collected on March 7, 2019. The red circle highlights the original location of the launched boulder. (**B**) Image collected on April 7, 2021, showing the TAG point (red X) and highlighting the large boulder thrown about 12 meters (red circle). Key features are labeled (see main text for discussion) For a blinking version see Movie S3.

5.2 Liberated Dust Mass Estimation

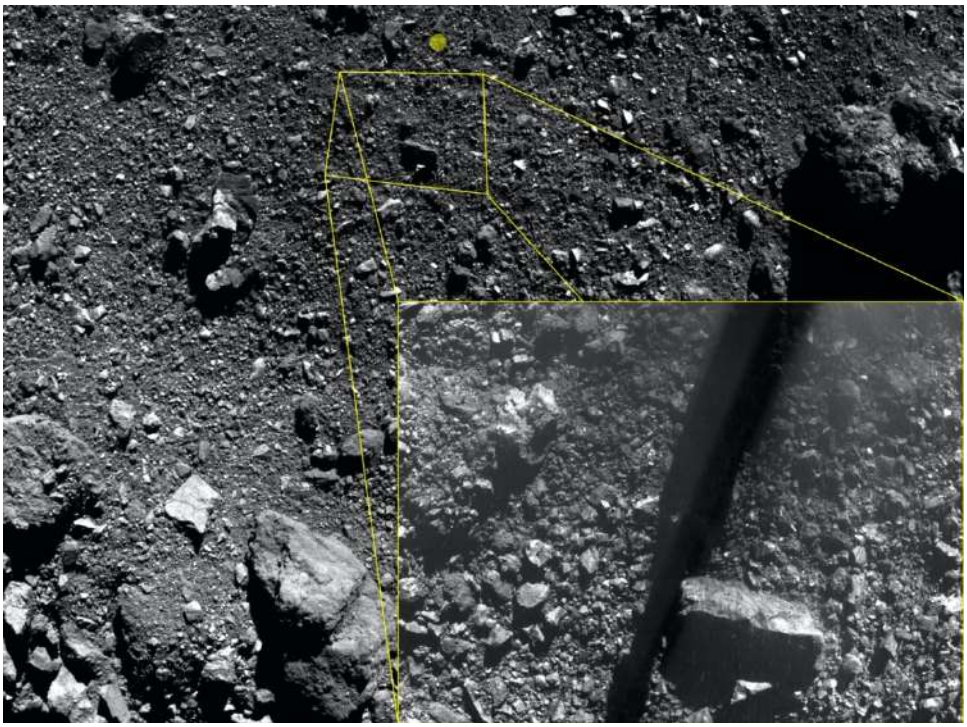

Figure S9. Last pre-contact NavCam 2 image with the contact location in the field of view acquired at 21:46:41.117 UTC. The yellow circle shows the contact location based on correlation with the SamCam image acquired at the time of contact. The inset image (lower right) is the NavCam 2 image acquired at 21:49:50.689 UTC during the initiation of surface contact. In the upper right of the pre-contact image is a boulder which was left undisturbed by the sampling event, indicating material outside of an area ~7 m in radius or more from the sample site was unchanged in the immediate aftermath.

We combined our measurement of the post-gas-release dust cloud's optical depth with the size frequency distribution (SFD) to determine the mass and source region of the dust cloud seen in Fig. 2D. We estimated overall mass and original layer thickness of the initial dust cloud by comparing the two images acquired before and after the gas release. Analysis of the opacity, mass, and original layer thickness of the unresolved dust component of the post-contact dust cloud relied on multiple assumptions, standard extinction relationships and a hybrid particle size frequency distribution, which we describe below.

Assumptions

We made several assumptions to simplify both the measurement and analysis. They are listed here:

1. The particles are spherical with radius r in the unresolved submillimeter size range (the resolution of the *before* and *after* images varied across the field but approximated 1 mm per pixel). We measured the optical depth due to the cloud's extinction of light from the reflected solar beam by comparing the signal above identical surface units in the *before*

and *after* images. We imposed a size frequency distribution for this submillimeter population and fixed the census constant so that the optical depth precisely matched the measured average optical depth.

2. The cloud is uniform. There is a uniform dispersal of all size ranges within the submillimeter population.
    a. One can observe concentrated streaks and streams of particle clusters, probably associated with larger particles fragmenting while streaming outward, but we will ignore that in this work; also, we avoided obvious streaks in our measurements.
    b. Particle sorting by size vs. distance from the center seems reasonable, but we also ignored that.
3. In measuring optical depth, we only counted unresolvable material scattering or absorbing reflected light. We did not count particles visible as such in the images.
4. The dust cloud is cylindrically symmetric around its center, which is assumed to be the center of TAGSAM.
5. The dust cloud presents as an upside-down cone of cross-sectional area A (as viewed from above). If flattened into a slab with the same cross-sectional area that slab would have average thickness z. The sub-population that we are interested in measuring results from the lofting of a layer of particles with cross-sectional area B and thickness y
6. The illumination geometry corresponds to an incidence angle of 66.6°, an emission angle of 0° and a phase angle of 66.6°.
7. The optical properties at 0.55 μm wavelength apply to the scattering and absorption of the solar light in the images.
8. The particles are large enough that extinction takes place in a geometric (as opposed to a Rayleigh, or Mie) regime.
9. Light passes through the cloud only once.
    a. This is justified based on the geometry. The solar incident beam illuminates the ground at a shallow angle (zenith angle = 66.7) without passing through the cloud; the cloud's radius is around 3 m and its height off the ground is around 3 m. Its general cross-sectional geometry is an upright cone with an angle around 45°, which allows the solar beam to have a direct view of the ground under the half of the cloud in the solar direction which is the precise part of the cloud being imaged.
10. Particle density ρ = 1800 kg m^{-3}. Mass concentration, mass of material per unit volume in the cloud itself, is denoted by $\mathbb{P}$, a number much smaller than 1800 kg m^{-3}.

Definitions:

- I_0 Initial Irradiance (Flux) or Radiance (Intensity) (from Sun) [W/m^2/μm/sr or W/m^2/μm or DN or DN/sec]
- I Irradiance (Flux) or Radiance (Intensity) at distance z (after extinction) [W/m^2/μm/sr or W/m^2/μm or DN or DN/sec; must be consistent with the 'before' measurement]
- ε_{ext} Extinction Coefficient (also called attenuation coefficient) [1/m]
- τ Optical Depth [Dimensionless]
- z Thickness of Cloud (distance over when extinction takes place) [m]
- B Cross-sectional Area of Dust Layer before lofting [m^2]

- y Thickness of Dust Layer before it gets agitated and lofted by gas bottle [mm]
- n Number Density of Particles of Dust within the Cloud [1/m^3]
- m Mass of an individual particle [kg]
- Q_{ext} Extinction Efficiency [Dimensionless]
- ρ Particle Density of [kg m^{-3}]
- P Cloud Mass Concentration [kg/m^{-3}]
- σ_{ext} Extinction Cross Section [m^2]
- α_{ext} Mass Extinction Coefficient (aka mass attenuation coefficient) [m^2 g^{-1}]
- r Radius of particle of dust within the Cloud [m]
- d Diameter of particle of dust within the Cloud [m]
- A Cross-sectional Area of Cloud Slab [m^2]
- V Volume of Cloud [m^3]
- M Mass of Cloud [kg]

Opacity Equations:

Beer's Law relates **intensity** [or **flux**] of incident and observed light to optical depth:

$$I = I_0 e^{-\tau_{ext}} \qquad \text{Equation S1}$$

Beer's Law solved for **optical depth:**

$$\tau_{ext} = \ln \frac{I_0}{I} \qquad \text{Equation S2}$$

Relating **optical depth** to extinction coefficient and path length, or cloud thickness:

$$\tau_{ext} = \varepsilon_{ext} z \qquad \text{Equation S3}$$

Relating **scattering cross section** to particle radius and scattering efficiency:

$$\sigma_{ext} = \pi r^2 Q_{ext} \qquad \text{Equation S4}$$

Relating **extinction coefficient** to scattering coefficient, particle number density, particle radius and scattering efficiency

$$\varepsilon_{ext} = n\sigma_{ext} = n\pi r^2 Q_{ext} \qquad \text{Equation S5}$$

Solving for **particle number density** or **particle concentration**, in terms of scattering properties, particle size, measured attenuation and cloud depth:

$$n = \frac{\varepsilon_{ext}}{\pi r^2 Q_{ext}} = \frac{\tau_{ext}}{\pi r^2 Q_{ext} z} = \frac{\ln\left(I_0 / I\right)}{\pi r^2 Q_{ext} z} \qquad \text{Equation S6}$$

Combining the 4 previous formulae to relate **optical depth** to scattering efficiency, cloud thickness, particle radius, and particle number density:

$$\tau_{ext} = \pi r^2 n Q_{ext} z \qquad \text{Equation S7}$$

Cloud mass concentration expressed in terms of other quantities:

$$\mathrm{P} = nm = \frac{\ln\left(I_0/I\right)}{\pi r^2 Q_{ext} z}\frac{4}{3}\pi r^3 \rho = \frac{4\rho r \ln\left(I_0/I\right)}{3 z Q_{ext}}$$ Equation S8

Equation S.9 relates mass extinction coefficient to extinction coefficient and cloud mass concentration, with subsequent equations showing how it relates to extinction coefficient, optical depth and cloud mass concentration:

$$\alpha_{ext} = \frac{\varepsilon_{ext}}{\mathrm{P}} = \frac{n\pi r^2 Q_{ext}}{\mathrm{P}} = \frac{\tau_{ext}}{z\mathrm{P}} = \frac{\ln\left(I_0/I\right)}{z\mathrm{P}} = \frac{3Q_{ext}}{4\rho r} = \frac{3Q_{ext}}{2\rho d} \approx \frac{3}{2\rho r} = \frac{3}{\rho d}$$ Equation S9

Relating particle mass to radius and particle density:

$$m = \frac{4}{3}\pi r^3 \rho$$ Equation S10

Defining the Cloud Volume as:

$$V = Az$$ Equation S11

Combining the above formulae to relate total Cloud Mass of dust cloud particles to Cloud Area (measurement), particle radius (independent variable), particle density, ratio of incident to observed signal (before/after signal ratio) and particle extinction efficiency in the geometric regime (assumed to be ≈2):

$$M = Vnm = Aznm = \frac{4Az\pi r^3 \rho \tau_{ext}}{3\pi r^2 Q_{ext} z} = \frac{4Ar\rho \ln\left(I_0/I\right)}{3Q_{ext}} = \frac{4Ar\rho\tau_{ext}}{3Q_{ext}}$$ Equation S12

Hybrid Size Distribution: Weibull/Rayleigh + Power Law

We combined the two distributions (Weibull/Rayleigh and Power Law) into a single closed form PSFD below and above the notch radius r_2:

$$dn = \begin{cases} C\dfrac{2r}{\lambda}e^{-r^2/\lambda^2}\,dr = C\,d_1\,dr & r \le r_2 \\ c_1 r^{-c_2}\,dr = c_1\,d_2\,dr & r \ge r_2 \end{cases}$$ Equation S13

The differential PSFD for particles in the smaller size range represents a Weibull distribution for k=2, also known as a Rayleigh, or Rayleigh-like, distribution and the PSFD for larger size ranges is a power law distribution. For convenience, we introduced the constants d_1 and d_2 to represent the terms accompanying the constants C and c_1.

The actual Weibull distribution is

$$f\left(r;\lambda,k\right) = \frac{k}{\lambda}\left(\frac{r}{\lambda}\right)^{k-1} e^{-(r/\lambda)^2} \text{ where } x = r/\lambda$$ (Papoulis & Pillai, 2002). Equation S14

The optical depth follows the same paradigm as above, though it is now the sum of two terms:

$$d\tau_{ext} = \begin{cases} \tau_{ext}^{\ Rayleigh} & r \le r_2 \\ \tau_{ext}^{\ Power\ Law} & r \ge r_2 \end{cases}$$

$$\tau_{ext} = \tau_{ext}^{\ R} + \tau_{ext}^{\ P}$$

Equation S15

We integrate the optical depth $d\tau_{ext}^{\ R}$ between the limits r_1 and r_2 and the optical depth $d\tau_{ext}^{\ P}$ between the limits r_2 and r_3

After integrating, we find that the Power Law optical depth is given by

$$\tau_{ext}^{\ P} = \pi Q_{ext} z \frac{c_1}{3-c_2}\left[r_3^{\,3-c_2} - r_2^{\,3-c_2}\right] = c_1\, d_3$$

Equation S16

The Rayleigh extinction optical depth is given by:

$$\tau_{ext}^{\ Rayleigh} = \pi Q_{ext} z C\left\{r_1^2 e^{-(r_1/\lambda)^2} - r_2^2 e^{-(r_2/\lambda)^2} + \lambda^2\left(e^{-(r_1/\lambda)^3} - e^{-(r_2/\lambda)^3}\right)\right\} = C\, d_4$$

Equation S17

We solve for the census constants C and c1 just as before, but this time subject to the constraints, which hold at the notch radius, r_2:

$$\tau_{ext} = \left(c_1\, d_3 + C\, d_4\right) dr$$

Equation S18

and

$$C\, d_1\, dr_R\left(r_2\right) = c_1\, d_2\, dr_P\left(r_2\right)$$

Equation S19

We solve the resulting system of 2 equations and 2 unknowns for the census constants:

$$c_1 = \frac{\tau_{ext} d_1}{d_1 d_3 + d_2 d_4}$$

Equation S20

$$C = \frac{\tau_{ext} d_2}{d_1 d_3 + d_2 d_4}$$

Equation S21

where $\lambda = r_2\sqrt{2}$, represents the most probable radius

For reference, in the above expressions,

$$d_1 = \frac{2r}{\lambda} e^{-r^2/\lambda^2}$$

$$d_2 = r^{-c_2}$$

$$d_3 = \frac{r^{-c_2}\pi Q_{ext} z}{3-c_2}\left[r_3^{\,3-c_2} - r_2^{\,3-c_2}\right]$$

$$d_4 = \pi Q_{ext} z\left\{r_1^2 e^{-(r_1/\lambda)^2} - r_2^2 e^{-(r_2/\lambda)^2} + \lambda^2\left(e^{-(r_1/\lambda)^3} - e^{-(r_2/\lambda)^3}\right)\right\}$$

Equation S22

5.3 TAG Debris Plume Analysis

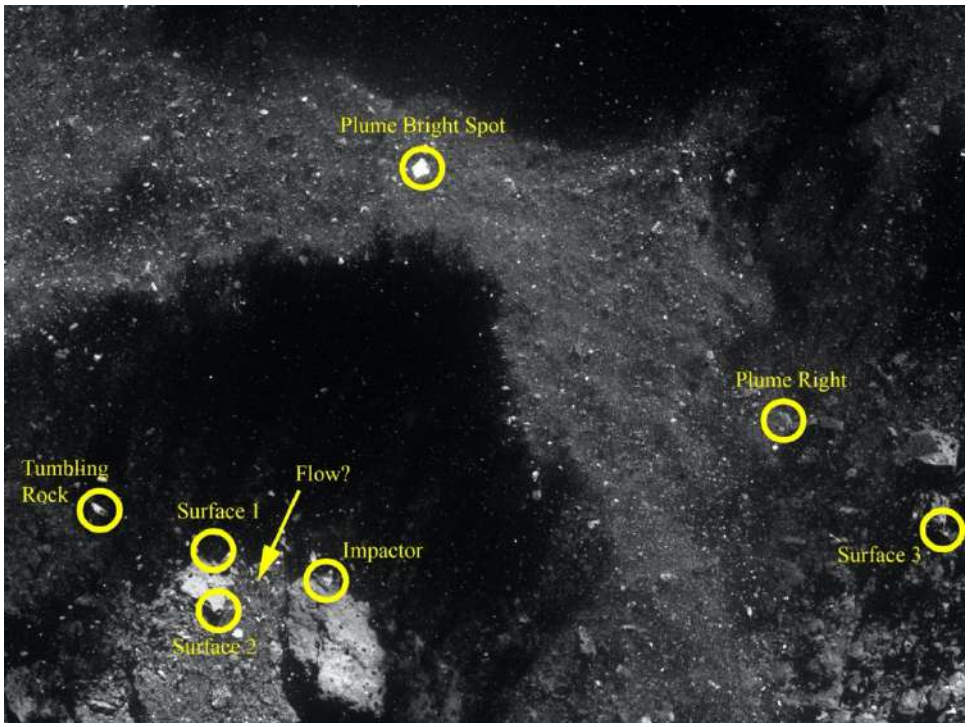

Figure S10. NavCam 2 image acquired during back-away at 21:50:49.680 UTC, showing an opaque lofted plume of mostly unresolved objects from the upper left of the image down to the lower right corner.

Seven features persistent throughout ~1 minute of the back-away imaging are indicated in fig. S10: three on Bennu's surface (Surface 1, Surface 2, and Surface 3) and four lofted objects (Tumbling Rock, Impactor, Plume Bright Spot, and Plume Right). Tumbling Rock is a high-albedo tabular body that tumbles above the surface and does not encounter the surface during the imaging period. The Impactor is a more rounded feature that is initially lofted but does not have enough altitude to clear one of the boulders on the original Bennu surface. The Plume Bright Spot and Plume Right are two larger rocks that are embedded in the plume and interact with the surrounding plume material. Also indicated is an area that exhibits characteristics of granular flow between two Bennu surface features. In this area waves of small rocks appear to "crash" on the larger boulders and remain in contact with the surface.

Image analyses indicate the lofted plume is composed of small, mostly unresolved particles moving away from the asteroid surface with apparent motion inconsistent with surface motion. Image-to-image tracking of the seven landmarks in Fig. 2A reveals different motion between objects that are lofted and those that are in contact with Bennu's surface. Fig. S11 shows that original surface features (indicated with triangles) are generally moving faster through the NavCam 2 images than objects that have been liberated from the surface (indicated with solid circles). First-order camera modeling using NavCam 2's viewing geometries during back-away imaging indicates that the higher altitude objects (*i.e.*, the lofted objects), cannot be mechanically attached to the surface or their apparent image speed would have to be the same or higher than the lower altitude objects to which they were rigidly attached.

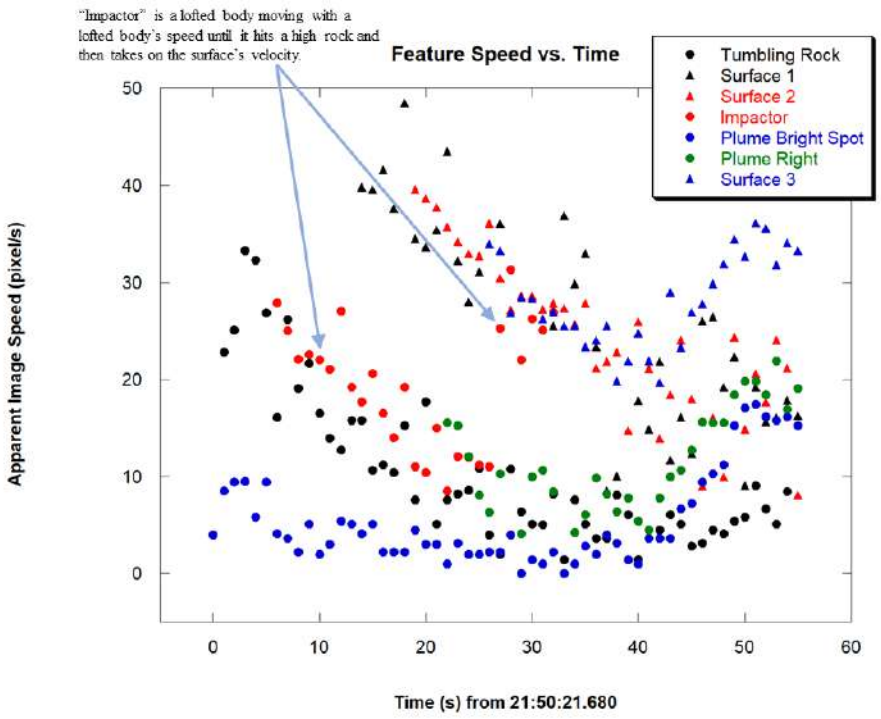

Figure S11. Plot of apparent lateral object velocities (pixels s^{-1}) in NavCam 2 images for the seven landmarks shown in Fig. 2A. The Impactor object (solid red circles) moves with a speed very different from the surface features until it contacts a boulder on the surface, partially fractures and then appears to move along with the original surface. Towards the end of the NavCam 2 back-away imaging (at ~40 s) all the landmarks appear to move with similar velocities due to spacecraft motion.

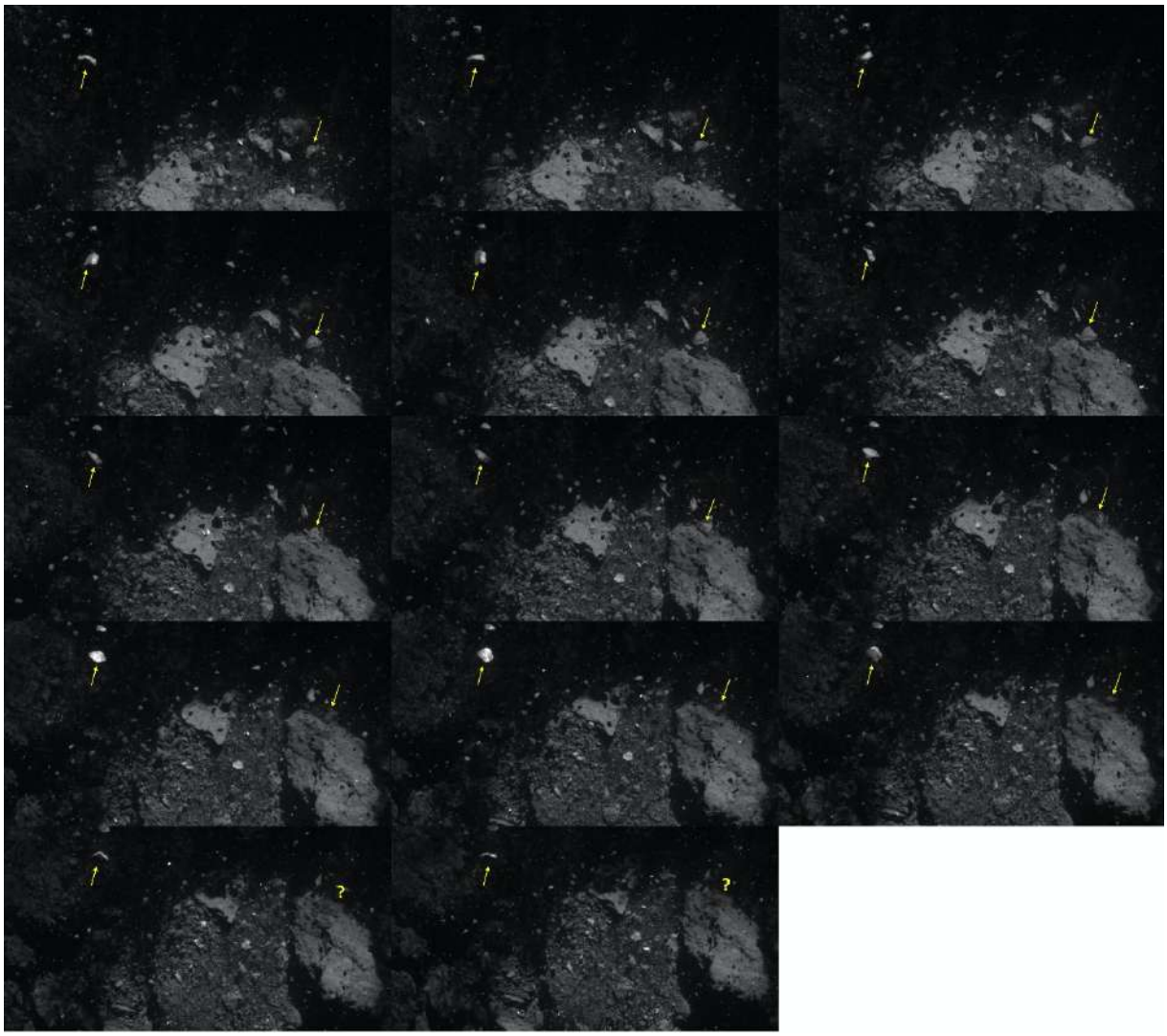

Figure S12. NavCam 2 post-contact image sequence showing two lofted bodies, one second separates each frame. The lofted object on the left is the Tumbling Rock from fig. S10. The lofted object on the right is the Impactor from fig. S10. To view the images in a time sequence, see Movie S4.

6 POST-SAMPLING INSTRUMENT PERFORMANCE

6.1 OCAMS DUST LOADING ESTIMATE

The degree of loading experienced by each of the three OCAMS cameras varied depending upon the imager and filter combination (table S4). SamCam has three identical panchromatic filters, to mitigate dust coating during sampling. It recorded a decrease in transmission of 57.3%. The PolyCam—with the largest opening of any optical instrument on the OSIRIS-REx science deck—recorded a decrease of 20.5%, while the MapCam's 5 color filters plus pan, recorded decreases of 7.5 (b'), 7.3 (v), 7.0 (w) and 7.0 (x) %. While spectrally flat, the dust appeared to be slightly more transmitting in the near-IR and red and slightly less transmitting in the blue and green.

Table S4. Post-sampling decrease in optical throughput for different OCAMS imager and filter combinations, NavCam 1&2, OVIRS, and OTES.

Optical System	Fraction of Original Transmission (%)
PolyCam	79.53 ± 0.36
MapCam b	92.27 ± 0.23
MapCam v	92.39 ± 0.33
MapCam w	92.74 ± 0.18
MapCam x	92.71 ± 0.37
MapCam pan30	91.99 ± 0.30
SamCam Pan 5 (relative to Pan 4)	42.7 ± 1.7
NavCam 1	33.6 $\pm$ 3.0
NavCam 2	30%
OVIRS	95%
OTES	85%

6.2 OCAMS Radiometric Calibration Update

The sampling event deposited dust on the external optical surfaces of the OCAMS imagers (MapCam's outer lens and PolyCam's primary and secondary mirrors). This dust loading results in decreased optical throughput. The OCAMS calibration pipeline translates raw camera data (measured in Digital Numbers) to physical units (represented as radiance and I/F) using radiometric conversion constants (RCCs) that depend on the optical throughput of the cameras [6]. We updated the pipeline's RCCs using a stellar-based radiometric calibration in which we compared images acquired of Vega before and after sampling (05 Nov 2019 and 19 Jan 2021, respectively).

Aliasing of the OCAMS detectors [6] prevented us from accurately imaging Vega as a point source. Therefore, PolyCam was intentionally defocused (focused away from infinity) to blur Vega over many detector pixels. MapCam, which does not have a focus mechanism, instead acquired data while the spacecraft slewed Vega across many pixels. We acquired three images with PolyCam and each MapCam filter [5] pre- and post-sampling. The images were dark subtracted using the median of three darks taken before the Vega images and three darks taken after. With each set, we compared the summed energy from Vega before and after sampling to estimate the change in optical throughput. We calculated the median of the three images for each filter to produce a final radiometric change. Table S4 lists the change in optical throughput for each filter.

We evaluated the efficacy of this update by comparing images of Bennu before and after sampling (excluding the sample site itself, which had obvious surface changes). Though the pre- and post-sampling images were acquired with similar observation geometry, they were not identical, which led to photometric differences. Therefore, we photometrically corrected all images such that the images represent normal albedo (0° phase, incidence, and emission) using published photometric models [63]. We found that the MapCam images compared favorably – i.e., MapCam measured the normal albedo of Bennu's surface as approximately the same (<0.5%) before and after sampling.

PolyCam, however, had radiometric offsets that varied across the surface. This variation was largest at the beginning and end of the observation windows, where the sub-spacecraft latitudes were most different (pre-sampling imaging transited from 5° to -2° latitude, while post-sampling imaging transited from -9° to +5° latitude). The radiometric offsets varied by a few percent on average. A pure radiometric calibration error would manifest as a scalar offset across the surface and observation window. A spatially varying difference indicated the offset depends, at least in part, on photometric correction. This was expected, as the variation was within the predicted accuracy of photometric correction – approximately ±5% from phase angles of ~8° [63]. Nonetheless, if uncorrected it would manifest as a true change in the surface. We therefore imparted an additional radiometric offset that we calculated locally over the region around the sample site, minimizing the difference between pre- and post-sampling imaging in this surrounding region. This multiplicative correction reduced the reflectance measured in post-sampling PolyCam imaging by an additional 1% and brought the radiometric/photometric uncertainty in PolyCam ratios to ~±1%. The efficacy of this correction is depicted in the pre/post-sampling ratio of the surface outside the sample site in Fig. 5a.

Dust loading on the OCAMS optics also produced additional stray light in all post-sampling images. In PolyCam, this manifested as spatially invariant background stray light that was dependent on the brightness of the scene. That is, it was in-field stray light that depends on how much of the field of view was filled by Bennu and the reflectance of the surface being imaged. We quantified the background by measuring shadows in pre- and post-sampling images. We found that the shadows (where there is theoretically no light) in pre-sampling imaging had an average reflectance of 0, but in post-sampling imaging had an average that varied between 0.002 and 0.005, with a median of 0.00317 across all images. We subtracted this additive correction from all post-sampling PolyCam images, reducing the uncertainty due to stray light to ~1%.

MapCam has out-of-field stray light that manifests as brightening in the corners and edges of the image where a bright source (i.e., Bennu) is just outside the field of view [19]. As such, the stray light depends on how the camera is pointed with respect to Bennu. We modelled the stray light, pre- and post-sampling, by averaging together many images of Bennu (in each position) such that Bennu itself averaged out, leaving the stray light signal. These 'Bennu flats' were not as effective as true flat fields but approximated the stray light to within ~1%. Figure S16 depicts the stray light patterns (for a northern Bennu pointing, i.e., observing the sample site) pre- and post-sampling. Due to dust loading on the lens, the stray light level increased from ~2% pre-sampling to ~5% post-sampling. Removing the stray light from pre- and post-sampling images before the change analysis reduced the uncertainty due to stray light to <1%.

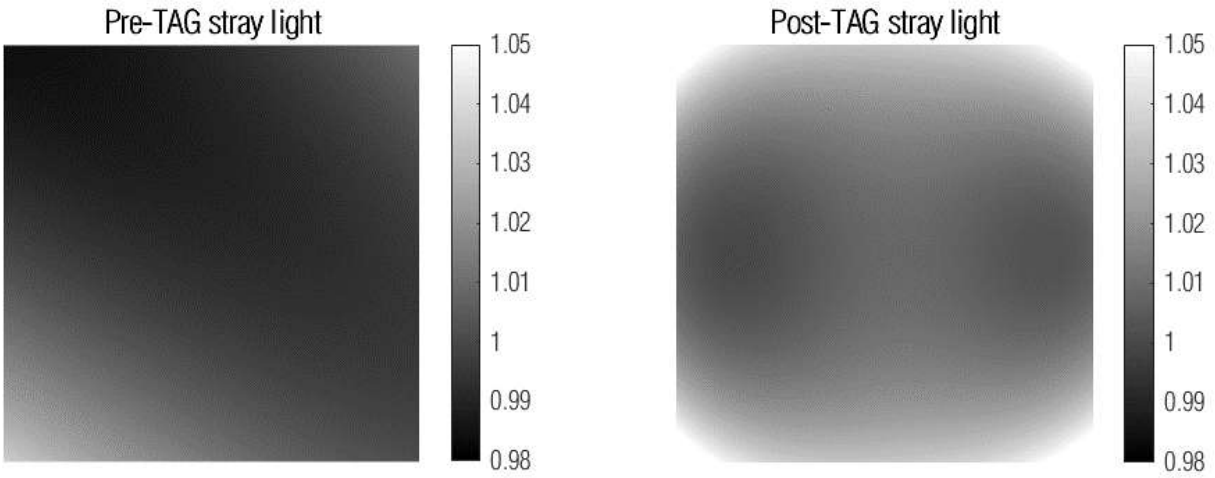

Figure S13. Dust loading on MapCam's outer optic increased the amount and structure of the stray light from bright sources immediately outside the MapCam field of view.

The final radiometric correction applied to the pre/post-sampling ratios involves the pre-sampling PolyCam images from Baseball Diamond Flyby 1 (FB1) [1]. Short exposure times in FB1 images led to detector artifacts along one edge of the images, which in turn reduced the efficacy of charge smear correction in the OCAMS calibration pipeline [6]. To produce a global albedo map of Bennu, using FB1 data, Golish et al. [6] implemented an advanced charge smear correction that used data from neighboring images to fill in the areas obscured by artifacts. This process was largely effective (reducing the radiometric error by a factor of 4) but left some uncorrected charge smear. These errors would appear in pre/post-sampling ratios as surface changes.

However, by reprojecting (using *cam2cam*) post-sampling images into the image space of a FB1 image, we directly measured the uncorrected charge smear. As with the reprojection steps in the change analysis, accurate image-to-image and image-to-shape-model registration was critical. We were careful not to let this process include (and remove) real surface change. Charge smear always occurs along detector columns, giving it a distinct linear form. Calculating the effect as a function of column isolated the artifacts and ignored true variations (which are extremely unlikely to manifest purely along detector columns). An example of the process, using an image of Nightingale (fig. S14), shows that the column-to-column variation was reduced from 2-3% to <0.5%, while the ~5% change at the sample site was not inadvertently imparted in the pre-sampling images. We removed the uncorrected charge smear from all FB1 data before performing pre/post-sampling ratios.

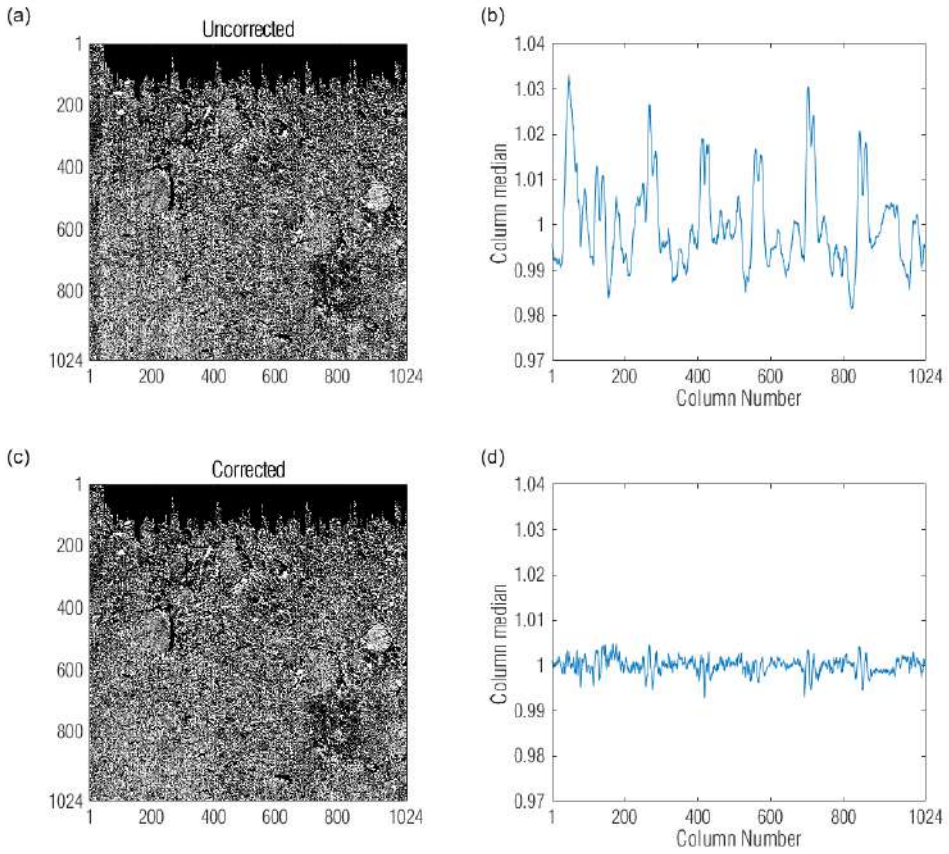

Figure S14. Uncorrected charge smear in FB1 images (a) have a columnar structure (b). Using post-sampling imaging as a reference, we can remove the majority of the artifacts (c and d).

6.3 NavCam 1

We measured a 66.4 $\pm$ 3.0% reduction in NavCam 1 throughput after TAG, presumably due to dust loading on the lens. The pre-sampling throughput was established through stellar observations in all the optical navigation images taken over the course of the mission, and the post-sampling throughput was determined similarly using stellar observations in the optical navigation images taken immediately post-sampling on 21 to 23 October 2020, as well as the optical navigation images taken 19 March to 9 April 2021, during the post-sampling campaign (Section 2). There was no significant change in the observed throughput between the 21–23 October 2020 images and the March/April 2021 images (fig. S15).

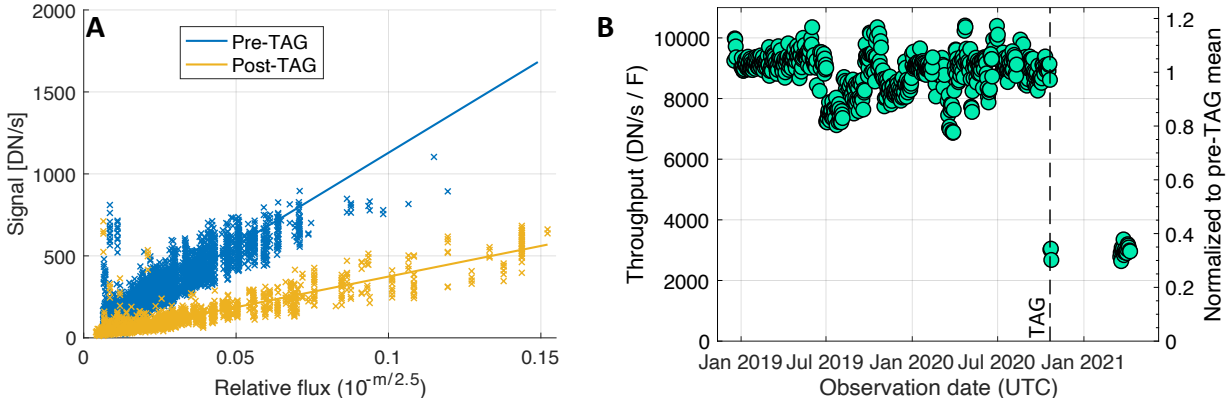

Figure S15. (**A**) Measured star signals for NavCam 1 as a function of expected relative flux according to the UCAC4 star catalog V-band magnitude. Pre-sampling (blue) is all stellar observations from 10 August to 20 October 2020 with their linear fit, the slope of which is the measured throughput. Post-sampling (yellow) is all stellar observations from 21 to 23 October 2020 and 19 March 19 to 9 April2021 with their linear fit. (**B**) Measured NavCam 1 throughput over time for stellar observations binned by observation date. The vertical dashed line denotes when sampling occurred on 20 October 2020.

NavCam 1 throughput was measured by comparing measured star signals to the expected relative flux as defined by the UCAC4 star catalog stellar magnitudes. The amplitude of the fitted PSF was used for the signal. The slope of a linear fit to the stellar signals as a function of relative flux provides a measure of the throughput in $\frac{DN}{s}/F$, where DN is the measured star signal, s is the image exposure time in seconds, and $F = 10^{-\frac{m_v}{2.5}}$ is the expected relative flux determined from the star's UCAC4 V-band magnitude mv. The NavCam 1 stellar observations were binned by observation date and this linear fit was performed separately for each observation date to produce fig. S15B.

6.4 NavCam 2

After the sampling sequence was completed, we captured images of star fields using NavCam 2 to assess the reduction in throughput due to dust coverage on the lens. We then took these star images and matched the observed stars with stars from the UCAC4/Tycho-2 star catalogs [64,65] using the processes described in Liounis *et al*. [66,67]. We repeated this process with star field images captured before arrival at Bennu during interplanetary cruise [8]. With the match between the observed stars in the images and the catalogue stars, we were able to estimate the reduction in through put by fitting a model of the form

$$I = \frac{gc}{1.25}10^{am} \qquad \text{Equation S.23}$$

where I is the observed intensity per second of exposure, g is the gain of the camera for the image, m is the magnitude of the observed star according to the star catalogue, and a, c are the fit parameters. We performed this fit using both the sum of the 5x5 grid of pixels about the

observed peak and the integrated volume of the fit point spread function to the observed star in the image. The fits from pre-sampling to post tag were compared and show approximately a 70% reduction in intensity throughput from before sampling for a 3rd magnitude star. These results are depicted in fig. S16.

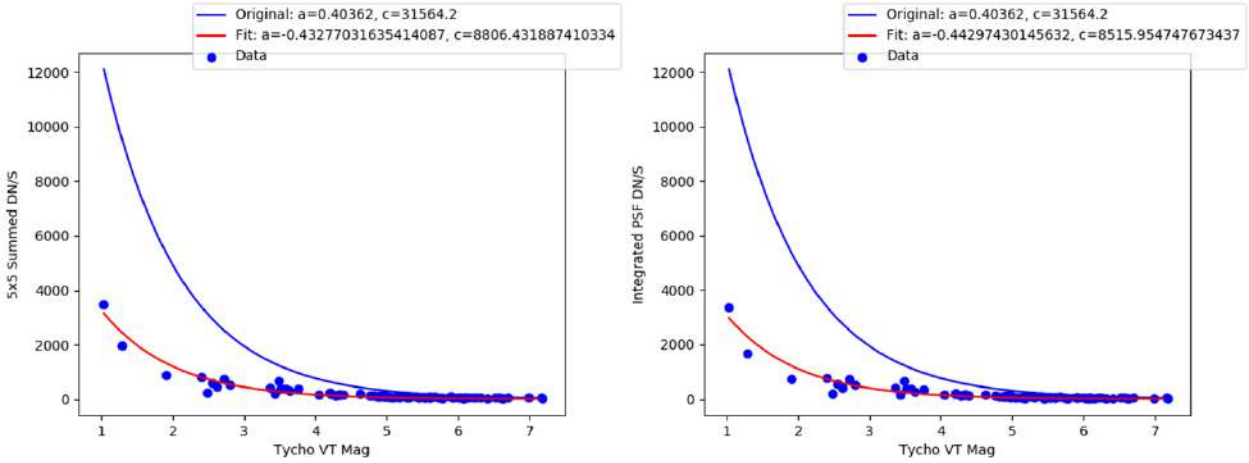

Figure S16. Comparison of conversion from visual magnitude to image intensity before (blue) and after (red) sampling using Tycho VT star magnitudes and a 5x5 summed grid of pixels (left) and the integrated volume of the fit to the point spread function of observed stars (right).

6.5 OLA

OLA achieved ~3% of valid signal returns during the final Bennu flyby, a significant decrease from the ~80% achieved during past operations of similar range, rendering these data unusable. Particulates kicked up by sampling may have collected on OLA's optical window, accounting for this reduced transmission. OLA's transmission and attenuation are estimated at ~70% and ~30%, respectively.

6.6 OTES

Given the potential for damage to or contamination of the OTES instrument during the sampling sequence, a standard deep space calibration sequence was acquired post-sampling on 18 November 2020. These data showed the instrument to be healthy, returning values within expected ranges for all telemetry. To evaluate the data for the presence of contamination we used a simple measure of instrument performance called the instrument response function, IRF. The IRF represents the contribution of the instrument itself (e.g., optical elements, beam splitter, mirrors, coatings, and detector) to the measured signal as a function of wavelength. The OTES IRF is determined using the equations and methods described in [9], which are not repeated here. Relevant to the analysis presented in this work is the fact that the magnitude of the IRF (for an uncontaminated instrument) varies over temperature primarily with the detector response and, to a lesser degree, interferometer alignment and does so in a predictable way. Thermistors on the instrument optics, and near the internal calibration target and detector enable measurement of relevant temperatures. Based on measurements acquired during environmental testing, the

OTES IRF varies, on average, <11% between 300 and 1350 cm^{-1} (7.4 to 33.3 µm) over the allowable operational temperature range of the instrument, 10 to 40° C [9]. To supplement the data shown in figure 16b of [9], we have calculated the variation in the IRF at 1090 cm^{-1} using data acquired during environmental testing (fig. S17). This wavenumber corresponds with the approximate location of the Christiansen feature in Bennu surface spectra acquired at roughly mid-day (i.e., a wavenumber at which there should be minimal absorption due to silicate minerals on Bennu [17]. This analysis shows that the total variation in the IRF at 1090 cm^{-1} over the allowable operational temperature range of the instrument is ~13%. However, throughout mission operations, the instrument temperature during science and calibration sequences has been consistently maintained at ~15 ±2° C, which results in a fluctuation in the magnitude of the IRF of only ~1% during typical operations. In contrast, the average IRF measured during the post-sampling calibration sequence exhibited a ~15% decrease in signal at 1090 cm^{-1} (fig. S16); given that only about 1% of that can be attributed to small fluctuations in the instrument temperature during the sequence, we attribute most of this change to the presence of a contaminant reducing the signal measured at the detector. The most likely location for this contamination is the primary mirror (and we assume so here), although we cannot definitively exclude contamination on other surfaces at this time.

Because the primary mirror is in the optical path of all post-sampling observations, the contribution of the contaminant cannot be removed with the standard OTES processing. Instead, we obtain a measure of the contaminant's wavelength-dependent spectral shape by dividing the average IRF from the post-sampling calibration sequence by the average IRF from a pre-sampling sequence and use this IRF ratio (Fig. 3) for analysis of the contaminant composition described in the text.

The OTES post-TAG emissivity spectra exhibited deviations from pre-sampling data that we attribute primarily to this contamination. The standard OTES calibration algorithm does not correct for the particulate contamination, resulting in the average BFF spectrum of Nightingale appearing to have greater spectral contrast than observed prior to sampling. However, scaling the BFF spectrum to a comparable pre-sampling spectrum reveals that the most substantial difference is minor changes in relative band depths (fig. S16B). If the contamination were opaque or optically thick, we would expect Bennu BFF spectra to resemble the contaminant spectrum rather than the pre-sampling data. Nonetheless, some of the observed difference in relative band depth <700 cm^{-1} (>14.3 µm) is likely attributable to interference from the particulate contaminant.

The effect of the particulate contamination on measured spectra varies with the relative temperatures of the contaminants (where the primary mirror temperature is a proxy for the contaminant temperature) and the scene. In the case where the scene is spectrally featureless space, the particulates are substantially hotter than the background (~15° C vs. -270° C) and we see their signature in isolation. When Bennu is the intended scene (during the BFF observations) its contribution is not featureless and is warmer than the particulates (~50 – 100° C vs. ~15° C), making for a more complicated physical interaction —the radiance from the scene will be absorbed by the particulates and re-emitted at their temperature with the particulates contributing their own spectrally-dependent radiance [68]. We note that temperature estimates for Bennu's surface in the BFF data are derived from applying the standard calibration to the BFF data and are not corrected for the effects of the contamination. However, they appear to be only

slightly different than model predictions for the solar distance and local time of the BFF observations, as reported in the text.

There is precedent for correcting thermal infrared spectra of planetary surfaces for this kind of contamination. The Mini-TES instruments on the Mars Exploration Rovers experienced a similar issue resulting from deposition of airborne particulates on the optics that directed energy into the instrument [32]. A model was developed to account for this contamination and correct the Mini-TES spectra [32,68]. Based on the characteristics of the BFF spectra and the known particulate spectral dependence, it is probable that a similar correction can be developed for the OTES instrument.

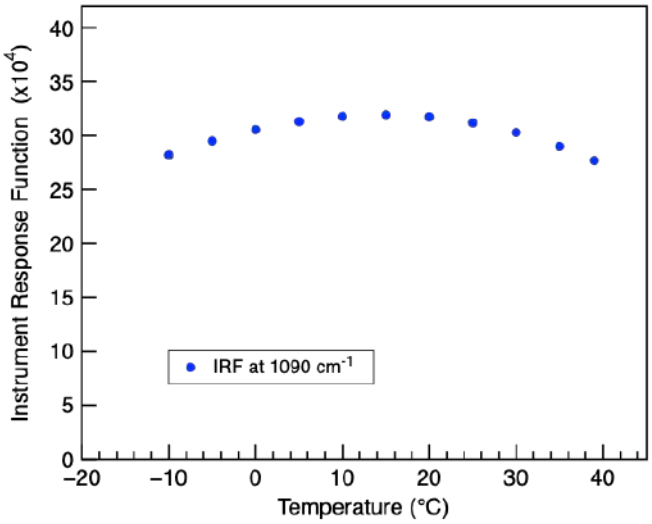

Figure S17. The predicted variation in the OTES Instrument Response Function (IRF in units of W Volt cm^{-2}/cm^{-1} sr^{-1}) with temperature at 1090 cm^{-1} based on measurements collected during thermal vacuum radiometric testing.

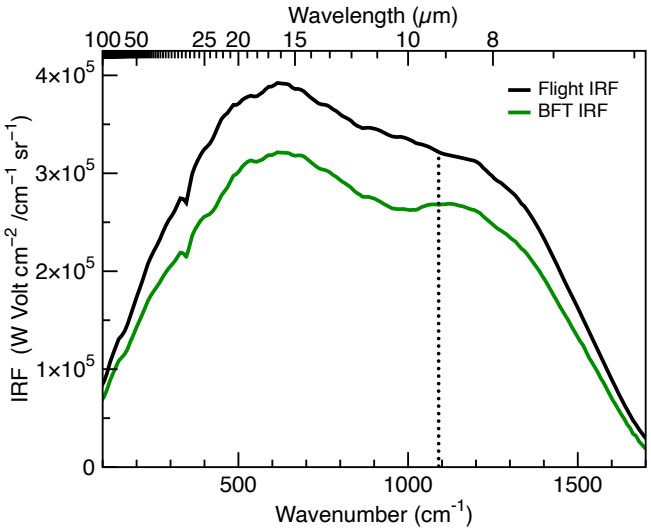

Figure S18. Comparison of pre- and post-sampling OTES instrument response functions. The Flight IRF exhibits the energy reaching the detector prior to particulate contamination during

the sampling event. The BFF IRF shows the reduction in energy reaching the detector after the sampling event. The wavenumber of the Christiansen feature in Bennu surface spectra (1090 cm^{-1}) is indicated by the dotted line.

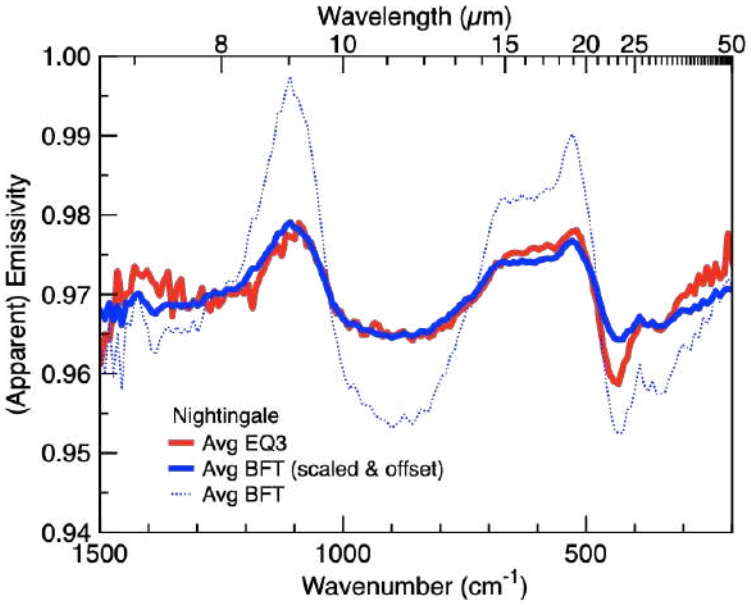

Figure S19. Scaling the final flyby spectrum to a comparable pre-sampling spectrum

7 Post-Sampling Altimetry

7.1 TAG Crater Characterization

PolyCam images of the sampling region were used to develop a Digital Terrain Map (DTM) of the Nightingale site following sampling. These images have a spatial sampling of the surface of approximately 5 cm per pixel, which is limited relative to the much higher resolution data of nearly 2 mm per pixel collected prior to sampling. The post-sampling DTM used in this analysis was developed with stereophotoclinometry (SPC) [34]. The DTM was built with a ground sample distance also equal to 5 cm per pixel to maximize the use of spatial information captured by the images. The images, however, were not ideal for SPC use. Lighting conditions were limited to near identical conditions with high incidence angle. The spacecraft viewing geometry also varied moderately across the post-sampling site. Only three of the 5 imaging conditions needed for making an SPC product were achieved [36,69]. Comparison of this DTM to the OSIRIS-REx Laser Altimeter DTM with the same ground sample distance of 5 cm produced with data collected before sampling shows that the SPC DTM has vertical uncertainties slightly larger than the resolution of the images used to develop the DTM. The comparison reveals that the root mean square across undisturbed regions is 16 cm; these uncertainties are greatest at the summit of boulders but less in smoothly varying terrain near the TAG point, which are 10 cm.

The post-sampling DTM was built by registering portions of the images obtained during the farewell tour to landmarks exterior to the crater that were not affected by the sampling event. These landmarks were developed by combining **SP**C and **O**LA data to build a high resolution

588 "**SPO**" global shape model of Bennu. This new model used all images of the surface of Bennu
589 from both OCAMS and TAGCAMS collected over the entire mission. These SPO landmarks
590 ensured proper regional registrations of the ensuing DTM with the global SPO model. The images
591 locked in placed were used to develop small scale DTMs or maplets in the area where the
592 sampling activity had disturbed the Nightingale site. These new maplets were then combined to
593 build the post-sampling DTM.
594 The resulting DTM is not perfectly registered with the OLA pre-sampling DTM. There is
595 about a 10 cm radial offset between the two, mostly due to a scale difference between the global
596 SPO and the global OLA shape model (OLAv20). The difference in these two models arises from
597 the weight given to the different data types used in modeling the asteroid. SPO weighs imaging
598 data more heavily than altimetry ranges, while OLA results rely entirely on altimetric results. Both
599 models indicate a size for Bennu that is identical within the known uncertainties of all the data
600 that went into the developments of these models.
601 To accommodate this 10-cm offset the post-sampling DTM was carefully registered to the
602 OLA pre-sampling DTM. Landmarks that were not disturbed by the sampling were used for this
603 registration. We used landmarks where the surface shape was flat, to limit errors caused by local
604 height differences between the OLA and SPC DTM, which result from SPC's tendency to smooth
605 and shorten the heights of rocks, especially when the data are of limited quality.

606 ## 7.2 Surface Properties from Cratering Efficiency Assessments

607 TAGSAM collects sample by releasing nitrogen gas [4,15]. The velocity and thus energy
608 associated with gas release varies with temperature per the ideal gas law at the time of
609 deployment. Assuming temperatures of 250 to 400 K [31], the energy of the gas released ranged
610 from 6.7 to 11 kJ. For this estimation, we assumed that the energy of the gas could be equated
611 to the kinetic energy of a projectile with an assumed particle density of 2000 kg m^{-3}. Using an N_2
612 gas mass of 0.061 kg , the comparable projectile has a radius of 2 cm and velocities ranging from
613 470 to 600 m s^{-1}. We considered the scaling parameters for several types of targets listed in Table
614 S5. The use of these parameters provides a qualitative sense of the how different materials with
615 different angularity, porosity, and strength attributes could influence the formation of the
616 observed crater.
617 We also consider the energy from the thrusters in excavating the subsurface. The
618 backaway maneuver imparted a total velocity of 0.44 m s^{-1} (deceleration of 0.04 m s^{-1} plus escape
619 velocity of 0.4 m s^{-1}) to the spacecraft, which had a mass of ~1300 kg. Thus, the total kinetic
620 energy of thruster firing imparted to the spacecraft was 0.13 kJ. The thrusters are canted at a 45-
621 degree angle. We divide by cosine (45˚) to derive a total energy from the thrusters onto the
622 surface of 0.18 kJ. Even though the total energy of the thrusters is minimal compared to TAGSAM
623 gas release, the thrusters operated for 24 seconds after TAG and played a role in shaping the final
624 state of the surface after sampling.
625 Each material considered has both a gravity and strength scaling constant as
626 recommended by [45]. This allows for a uniform scaling relationship that includes the transition
627 between strength- and gravity-controlled cratering. We used a range of target regolith bulk
628 densities for our assessment from 500 kg m^{-3} to 1000 kg m^{-3}. The latter value is just below the
629 bulk density of 1190 ± 13 kg m^{-3} for Bennu [35].

Table S5. Parameters used to assess TAG cratering efficiency.

Target type	Qualitative attributes	Scaling exponent, μ	Gravity scaling constant, H1*	Strength scaling constant, H2*	References
Sand	Sub-angular No tensile strength Angle repose = 28-35 Porosity=35±5%	0.41	0.59	0.4	[45-47,70-72]
Glass beads	Rounded No tensile strength Angle repose = 28-35 Porosity=35±5%	0.5	0.27	1.	[73]
Sand Fly Ash	Angular Low tensile strength Porosity=60%	0.35	0.59	0.81	[46]

* Uniform scaling relationship used as per Holsapple, 1993 for estimating cratering efficiency.

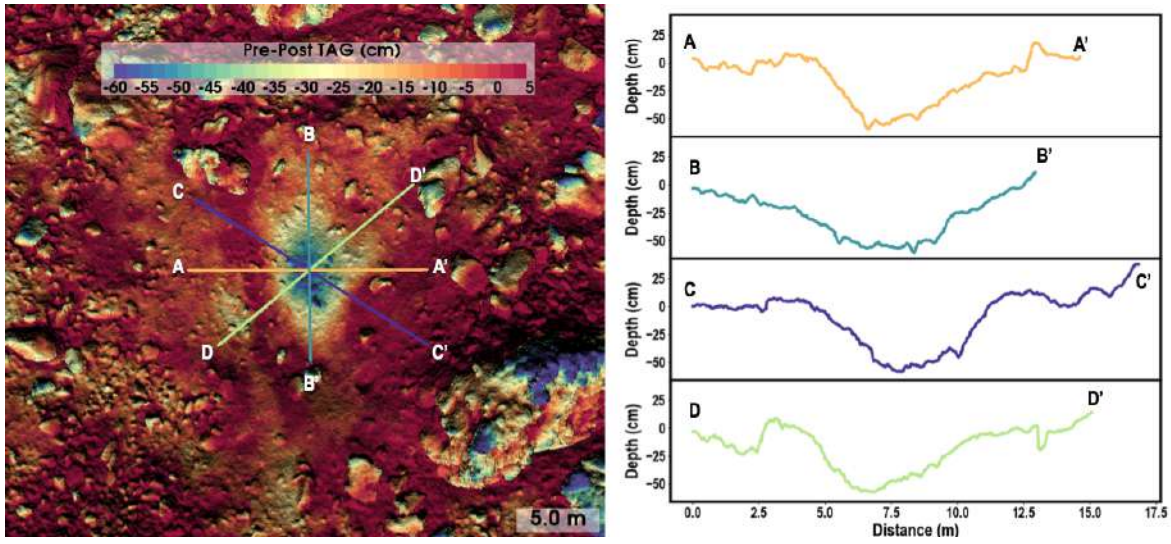

Figure S20. Profiles (right-hand) through TAG-crater using difference map (left hand side) between the pre-sampling OLA DTM and post-sampling SPC DTM. The difference map is overlain on the original pre-sampling DTM generated with OLA data.

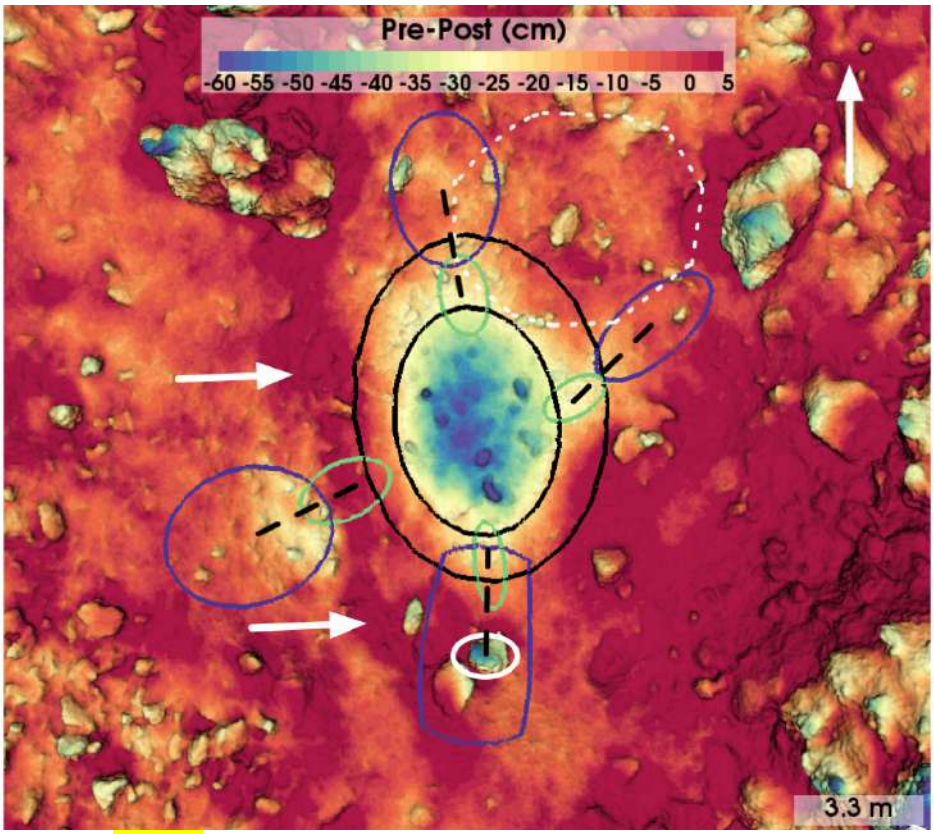

Figure S21. Same as Fig. 4D highlighting features of interest. These include areas influenced by the spacecraft thrusters (light green ellipse for start position and dark purple for final position); a boulder that appears in the scene after sampling (solid ellipse); white arrows indicate location where debris might have been deposited during surface relaxation (). Black ellipses show two bounding cases for the post-TAG crater used in this analysis: the smaller limit measures 6.0x4.3m or 5.1±1.2 (Total displaced volume=8.6±0.9 m^{-3}) and is delineated by the inner edge of the estimated thruster plume locations, and thus results from TAGSAM gas release. The large crater is likely a combination of both TAGSAM and thruster firing during the backaway burn and measures 9.0x6.5m or 7.8±1.8m (Total displaced volume = 12.2±0.9 m^{-3}). Black dotted lines approximately connect the maximum thruster pressures at the start and end of the departure maneuver [15]. Dotted region to the north and north-west of indicate regional readjustment.

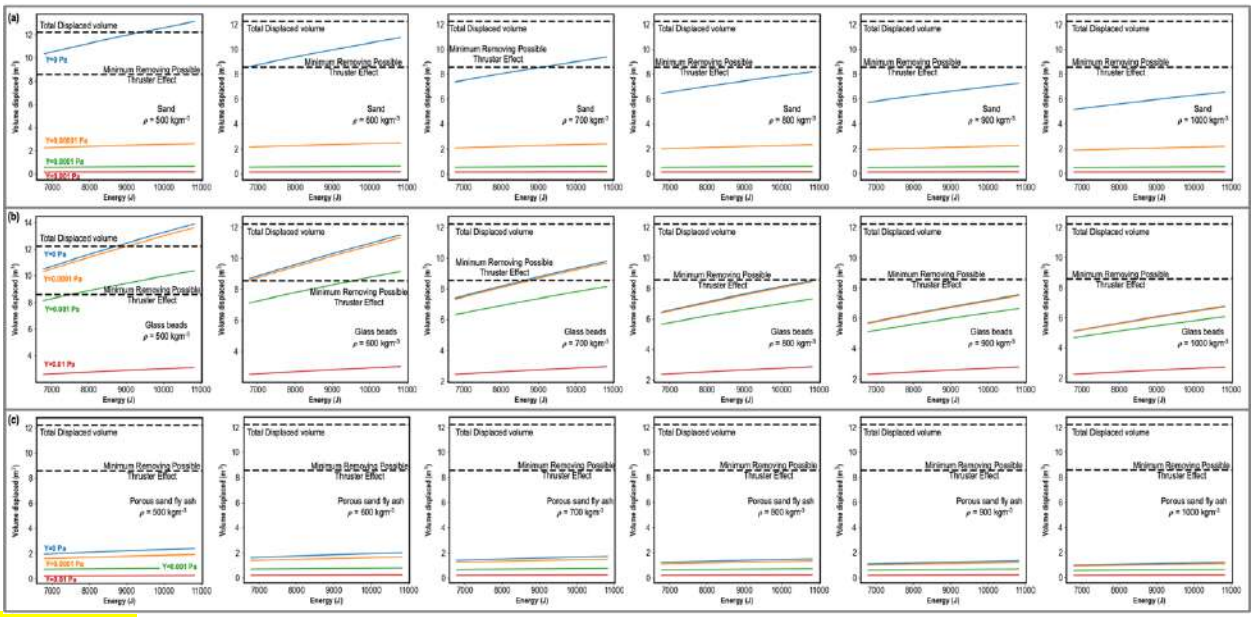

Figure S22. Cratering efficiency as a function of energy release for surface material with sand-like characteristics (A and B), glass-bead like characteristics (C and D) and sand-fly ash characteristics (E) (see table S5 for details).

8 POST-SAMPLING SFD

8.1 PRE-SAMPLING ANALYSIS

The work of [14] summarizes the huge team effort accomplished to count particles on the whole surface of Bennu, as well as on the primary and backup site selected. For the Nightingale sample site, several multiscale imagery datasets were used to count particles pre-sampling from the Baseball Diamond (BBD), Recon A, and Recon C campaigns [1], with average pixel scale images ranging between 0.05 m, 0.01 m and 0.004 m, respectively, and average phase angle between 31° and 57°.

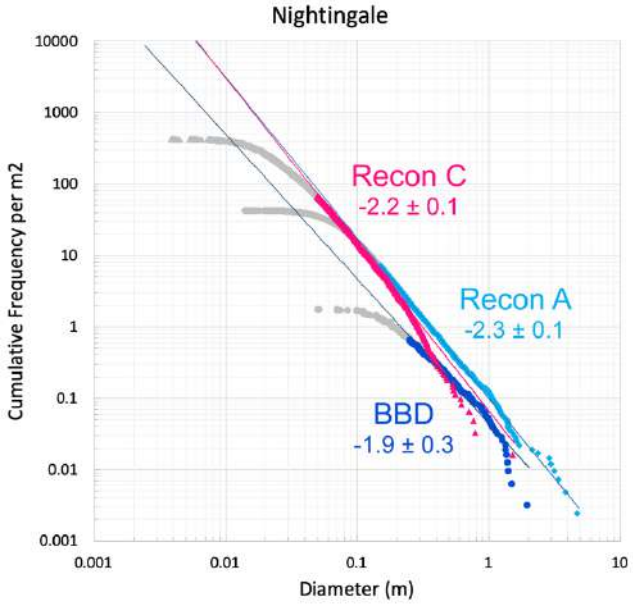

Figure S23. The Nightingale pre-sampling size frequency distributions obtained on the BBD, Recon A, and Recon C imagery datasets, with the corresponding power-law indices obtained above the completeness limits. Particles below the completeness limit are shown in grey. Data from [14].

8.2 Particle Distribution in the Newly Formed Crater

The imagery dataset that we used to determine the SFD of the surface post-sampling consists of seven OCAMS PolyCam images taken on 7 April 2021, all with pixel scale of 5 cm and a phase angle ranging between 9.07° and 9.74° (table S6). Such images fully cover the Nightingale site post-sampling, hence providing the possibility to identify all particles present on site larger than 4 pixels, as commonly done on other Solar System bodies [74,75].

Table S6. List of the seven OCAMS PolyCam images used for particle identification.

OCAMS PolyCam Image ID	Acquisition Time (UT)	Phase Angle (°)	Pixel Scale (m/pixel)
ocams20210407t062114s948_pol_iofl2pan_536373.fits	2021-04-07T06:21:14	9.52	0.05
ocams20210407t061636s649_pol_iofl2pan_536358.fits	2021-04-07T06:16:36	9.73	0.05
ocams20210407t061631s050_pol_iofl2pan_536357.fits	2021-04-07T06:16:31	9.74	0.05
ocams20210407t062558s469_pol_iofl2pan_537301.fits	2021-04-07T06:25:58	9.29	0.05
ocams20210407t062604s065_pol_iofl2pan_537298.fits	2021-04-07T06:26:04	9.28	0.05
ocams20210407t063042s461_pol_iofl2pan_537263.fits	2021-04-07T06:30:42	9.09	0.05
ocams20210407t063048s046_pol_iofl2pan_537262.fits	2021-04-07T06:30:48	9.07	0.05

We made use of the Small Body Mapping Tool software (SBMT) [76] to project such images on the DTM prepared for the post-sampling Nightingale site. Afterwards, we imported the estimated contact spot (30 cm size) and selected a circle larger (11.8 m) than region around the predicted contact point defined by the 2-sigma dispersions on the spacecraft trajectory (8.6 m

size) [14] but concentric, to have a wider statistic of particles that may have been mobilized during sampling. We then identified all particles as ellipses, deriving their maximum sizes and cumulative frequency per square meter (fig. S23).

The possibility to double-check the identified particles on different images taken at slightly different illumination and viewing angles was of help, since the low phase angle (<10°) results in only small shadows cast. The total number of particles identified in the study area is 1048, with a maximum diameter of 1.9 m. The resulting cumulative number of particles per square meter is indicated in fig. S25, with a density of 0.01 for the maximum size and 6.02 for 20-cm particles.

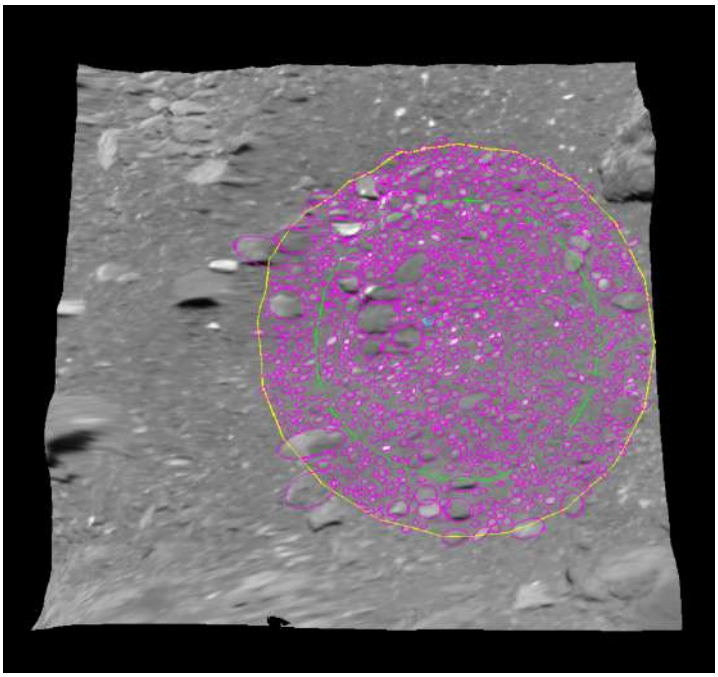

Figure S24. The 1048 particles identified inside the Nightingale site post-sampling. The light blue circle is the estimated contact spot (30 cm). The green circle is the 80 percent 2 sigma sampling site (8.6 m size). The yellow circle is the actual 11.8 m circle where we counted all particles. The image in background is ocams20210407t062114s948_pol_iofl2pan_536373.fits (pixel scale of 5 cm) overlaid on the post-sampling DTM.

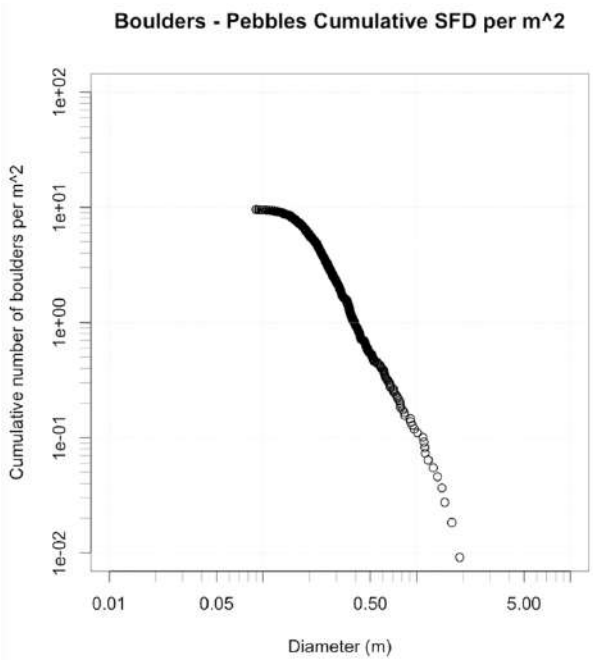

Figure S25. Cumulative number of particles per square meter identified on the Nightingale post-sampling surface.

To test whether the resulting SFD can be fitted by a power law, as done for the pre-sampling counts [14], we used the Clauset et al. [77] methodology. This approach validates the existence of the power-law fitting model, which is characterized by the scaling parameter called α_{Cl}. The power-law index of the cumulative distribution we hereafter refer to as α is related to the scaling parameter as $\alpha = 1 - \alpha_{Cl}$. This method also identifies the completeness limit x_{min}, which is the threshold value above which the power-law exists. The estimation of x_{min} is done through the Kolmogorov-Smirnoff (KS) statistic which finds the value that minimizes it. Afterwards, α_{Cl} is determined through the maximum likelihood estimator (MLE). The uncertainty for both α_{Cl} and x_{min} is then derived through a non-parametric bootstrap procedure that generates many synthetic datasets from a power-law random generator and performs several KS tests to verify if the generated and observed data come from the same distribution.

This technique returns a *p*-value that can be used to quantify the plausibility of the hypothesis. Considering the significance level of 0.10, if the *p*-value is $\geq$0.1, then it is possible to conclude that any difference between the empirical data and the model can be explained with statistical fluctuations [77]. On the contrary, if the *p*-value is <0.1, then the data set does not come from a power-law distribution, but instead, from a different one.

Through the KS statistic we identified that the completeness limit x_{min} for the Nightingale post-sampling counts is 0.22 m (with a total number of 561 particles larger than x_{min}), while the value of the power-law index α is –2.7 (fig. S26). To evaluate the uncertainty for x_{min} and α we generated 1000, 5000, and 10,000 synthetic datasets using the non-parametric bootstrap procedure. For all cases we derived a x_{min} uncertainty of 0.02 m, while a 0.15 uncertainty for α. The scatterplot of x_{min} against α is presented in fig. S26B, in order to evaluate how a change in x_{min} results in a different value for α, while the frequency histograms of x_{min} and α are indicated in fig. S26, C and D. As presented in fig. S26A, the *p*-value obtained is 0.65. Since this value is

≥0.1, we can affirm that (i) any difference between the empirical data and the model can be explained with statistical fluctuations, (ii) we cannot reject the power-law model for these data, and (iii) the data are consistent with a power-law.

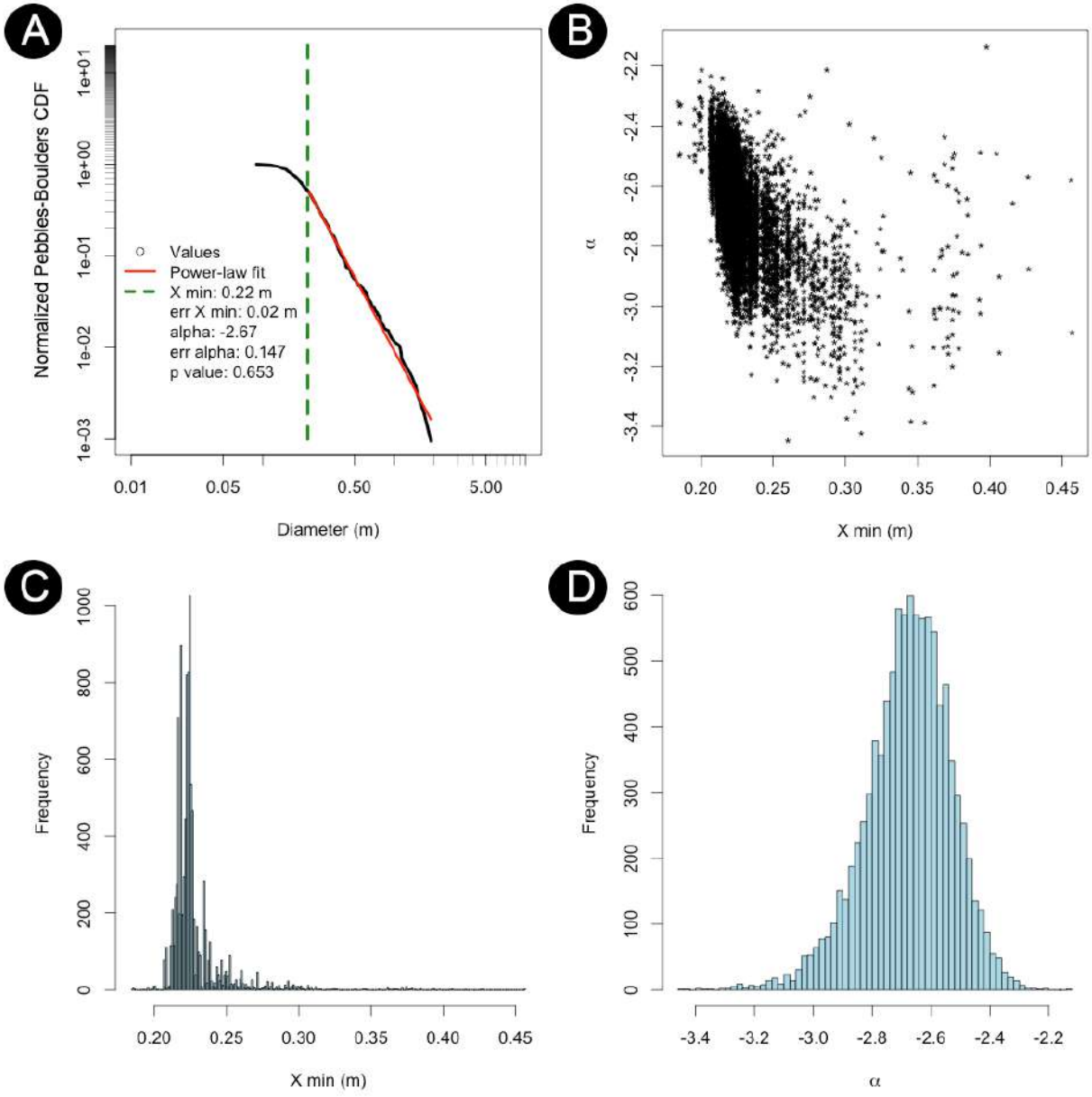

Figure S26. (A) Normalized cumulative distribution function showing the obtained sizes, the power-law fitting curve and the x_{min} limit. The total number of particles larger than x_{min} and used for the fit is 561. (B) Scatterplot of x_{min} against α resulting from 10000 synthetic datasets. (C) Frequency histogram of x_{min}. (D) Frequency histogram of the power-law index α.

Our post-sampling counts have a completeness limit of 0.22 ± 0.02 m and the resulting power-law index is -2.7 ± 0.2. If we compare these results with the pre-sampling data (fig. S27), the sampling event has generally increased the number of small particles when compared to the

pre-sampling surface. Despite the slightly worse illumination conditions of the post-sampling imagery data (<10° phase angle with respect to the 52° of BBD or 31° of Recon A), it has been possible to reach a completeness limit that is 3 cm smaller than the BBD one. The post-sampling resulting power-law index does not overlap (even if the error bars are taken into consideration) with the BBD value or Recon A values. Moreover, the number of counts, and the corresponding density per square meter, is always larger than the pre-sampling situation, for all particle sizes smaller than 90 cm. Conversely, the largest dimensions show comparable densities to the pre-sampling situation.

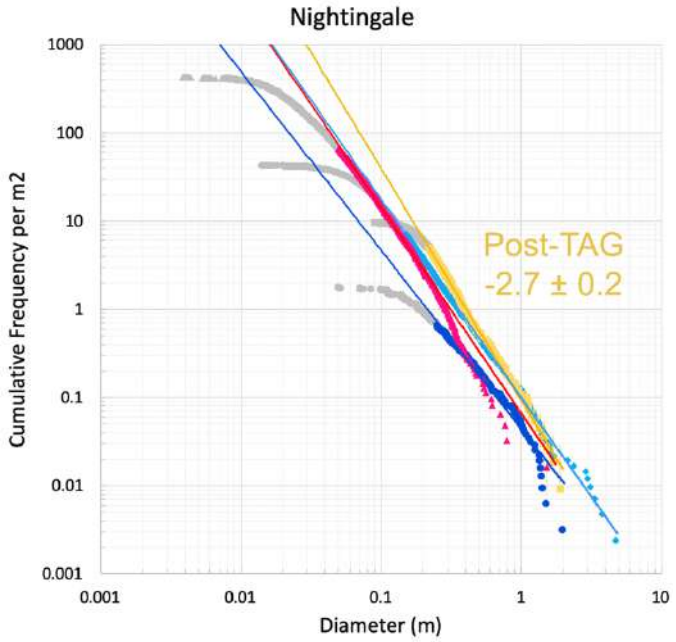

Figure S27. The Nightingale post-sampling SFD compared to the pre-sampling results of Burke et al. (2021).

In situ fragmentation may have modestly contributed to the observed increase in particles smaller than 90 cm. The disruption threshold for a 40 cm-diameter spherical rock is ~ 40 Joules/kilogram if it is impacted by a projectile at 500 m s^{-1} [28]. Assuming a particle density of 2200 kg m^{-3}, a 40-cm rock requires ~ 2920 J to catastrophically disrupt. Since the estimated energy of the gas released during sampling ranged from 6700 to 11000 J, 40-cm size rocks could have been disrupted, creating fragments as large as 32 cm. Assuming that the fragments from the disruption are described by a power-law SFD with an exponent of –2.7 (fig. S27), the sampling event would have produced an additional 4.4 to 7.8 rocks with diameters between 25 and 32 cm, representing an increase of 2 to 4%. In contrast, if we compare the BBD density of 25-cm particles with the post-sampling results, we see that there is an increase of 5.5×. Therefore, the increase in the numbers of particles smaller than 90 cm was likely dominated by the surface flow effects outlined above.

9 OCAMS CHANGE ANALYSIS

We performed the sampling change analysis by taking the ratio of post-sampling images to pre-sampling images from MapCam and PolyCam. We photometrically corrected all images to 0° phase, incidence, and emission using published photometric models of Bennu [6]. To divide the images directly (pixel-by-pixel), we used the ISIS application *cam2cam* to reproject a pre-sampling image from its own image space (fig. S28A) to the image space of the post-sampling image to which it was compared (fig. S28B). The result was the pre-sampling image as if it had been acquired with the post-sampling geometry (fig. S28C). This reprojection depended critically on the registration of the images with respect to each other and the shape model, as well as the accuracy of the shape model. For MapCam, we used OLA v20 shape model tiles with a ground sample distance (GSD) of 20 cm (better than the ~25 cm per pixel resolution of the images). For PolyCam, we used OLA v20 shape model tiles with a GSD of 5 cm (similar to the ~5 cm pixel scale of the images).

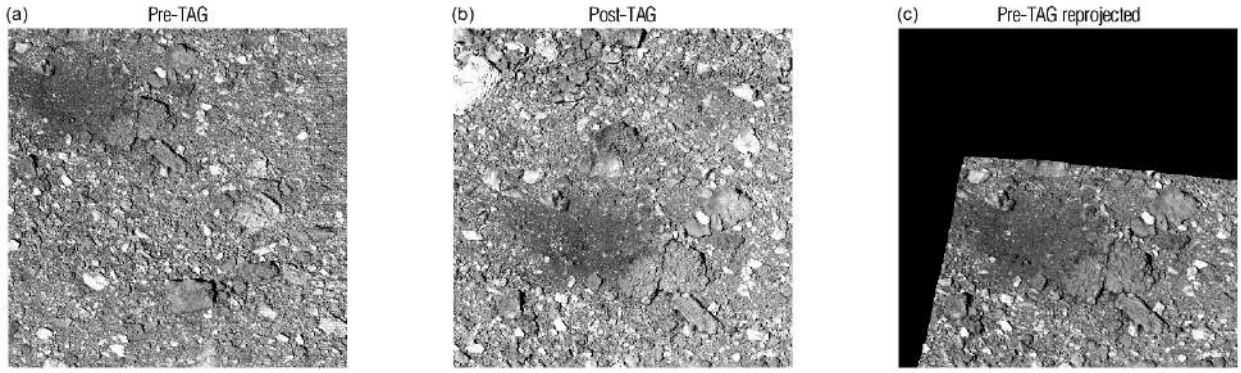

Figure S28: To calculate albedo changes of the surface due to the sampling event, we measure the change between a pre-sampling image (a) and a post-sampling image (b), where we have reprojected the former to match the viewing geometry of the latter (c).

Even with careful registration and high-resolution shape models, reprojection was imperfect for features with large height differences (e.g., tall rocks or steep-walled craters). Slight observation geometry differences led to slight shifts in their locations during reprojection. This produced small 'hot spots' in the image ratios (Fig. 6A). These hot spots did not detract from the analysis for two reasons. First, they were typically lower in magnitude than the change measured at the sample site. Second, those that were of similar magnitude were universally associated with rapid height changes in the surface (e.g., the shadow of a tall rock appeared to shift). This was particularly evident in the PolyCam ratio image, which was inherently more sensitive to this effect due to its higher spatial resolution. For example, ratios around the rock southwest of the sample site were as large as 75% due to its shifting shadow but were not representative of true surface changes.

We calculated cross-sections (Fig. 6A) through the sample site by taking the median of the rows/columns within the solid grey lines (MapCam) and dashed black lines (PolyCam). We smoothed the resulting vectors using a moving low-pass filter with a width of 13 and 9 pixels for MapCam and PolyCam, respectively. We resampled the smoothed vectors from pixel space to

physical extent (in meters) relative to the center of the median windows. This allowed us to average the vertical and horizontal cross-sections together to further reduce noise, as well as plot the MapCam and PolyCam cross-sections on the same plot.

To calculate MapCam spectra of the surface, we reprojected the b', w, and x MapCam images to match the observation geometry of the v image, again using *cam2cam*. We created the absolute MapCam spectra by calculating the median of the pixels in the square defined by the intersection of the horizontal and vertical median cross-sections. We calculated the median in each of MapCam's four color filters for the pre- and post-sampling observations. The error bars plotted with the absolute spectra represent the published ±5% radiometric uncertainty [6]. To create the normalized spectra, we divided the absolute spectra by the value at 550 nm (the v filter's effective wavelength). The errors bars plotted with the relative spectra represent a filter-to-filter uncertainty of 1%.

OCAMS image registration

As noted above, accurate registration of the images to each other and a Bennu shape model was critical to the *cam2cam* reprojections used in both the change analysis and effective calibration of the images. This was achieved by photogrammetrically controlling the relevant images to the OLA v20 shape model.

For the PolyCam analysis, two pre-sampling PolyCam images, acquired at 17:37:51 and 17:45:01 on 07 March 2019, were determined to provide the best area of common coverage with the post-sampling Nightingale image, acquired at 06:21:14 on 07 Apr 2021. We created a control network of 406 control points by matching common features in the images to subpixel accuracy. We registered the PolyCam images to highest resolution OLA v20 shape model tiles (GSD ~ 5 cm, similar to the pixel resolution of the images). We used the 17:37:51 pre-sampling image, which provided the most coverage, as the ground truth source. We adjusted camera pointing and spacecraft position orientation in the other images to register with the ground truth image.

The jigsaw bundle adjustment solution for the PolyCam images had a mean RMS of 0.33 pixels with a maximum of 2.13 pixels on the control points. 392 of 409 (96.5%) control points have an RMS of less than 1.0 pixel. The 17:45:01 pre-sampling image had an average RMS of 0.64 pixels; the 06:21:14 post-sampling image had an RMS of 0.43 pixels.

For the MapCam analysis, 16 post-sampling images that included Nightingale (four from each of MapCam's four color filters) were co-registered to a single pre-sampling v-filter image (acquired at 20:03:31 on 07 Apr 2021). The pre-sampling image had been previously controlled to the global (88 cm GSD) OLA v20 shape model for global color mapping [19] and was used here as ground truth for the post-sampling images. The control network, with measurements shared between the pre- and post-sampling images, contains 195 control points (fig. S29) and 1418 measures. We computed all control point latitude, longitude, and radius values based on the pre-sampling image and held them fixed. The camera angles for the 16 post-sampling MapCam images were constrained to vary by no more than 1.0 decimal degree and adjusted relative to the pre-sampling image. We held the spacecraft position fixed in the solution. The maximum control point residual was 2.38 pixels with an average residual of 0.78 pixels.

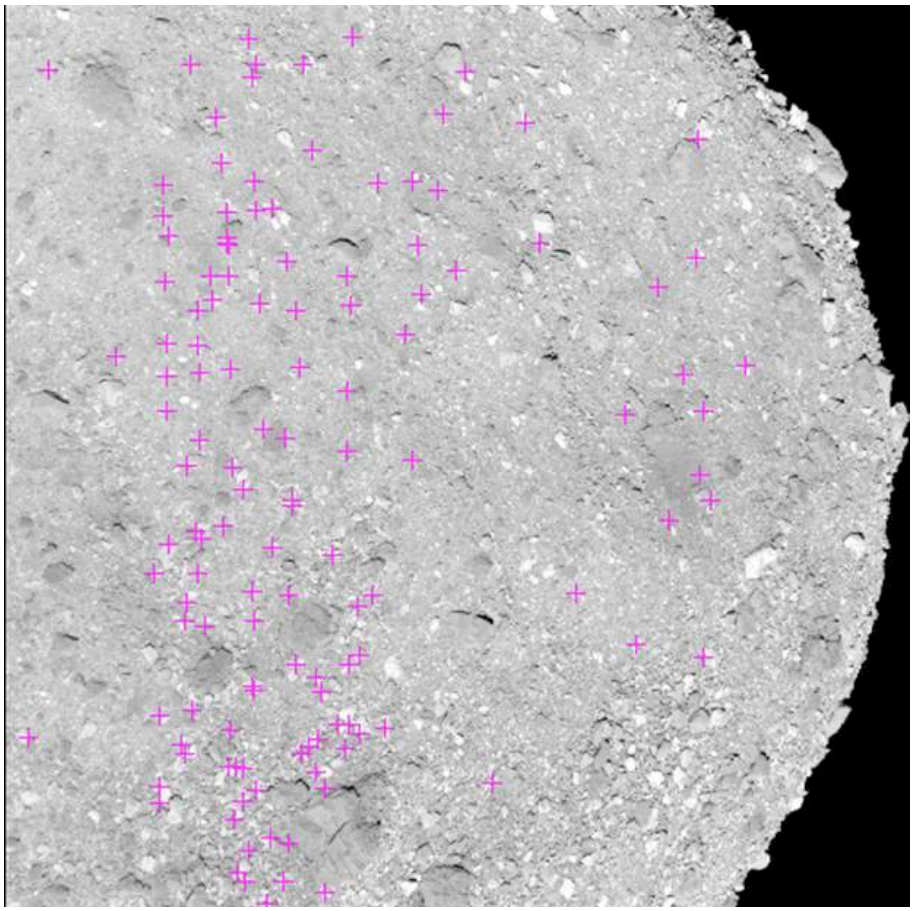

Figure S29. The pre-sampling MapCam image with an overlay of control point locations measured with the overlapping post-sampling MapCam images. The latitude, longitude and radius values of these points were established with the pre-sampling image and held as ground truth in the bundle adjustment.

10 OVIRS Change Analysis

OVIRS data post-sampling show a small decrease in throughput that varies with wavelength, and possibly instrumental conditions, from dust on the instrument. To compare changes in Nightingale before and after TAG, this effect was corrected using data from the Equatorial Survey phase. First, data acquired in May 2019 (EQ3), at ~12:30pm local solar time were used to generate a correction factor: all spectra from 45 to 50 deg N and 30 to 35 deg E, a small region near Nightingale but outside of the area affected by TAG, were averaged in both data sets. The spectral difference between the EQ3 and Bennu Farewell Tour data were calculated for this region; this technique coarsely adjusts for all changes between the two data sets: illumination angle, spatial resolution, and instrument performance. This correction was then applied to the Bennu Farewell Tour data before mapping. The Bennu Farewell Tour data have an original spatial resolution of ~12 m footprint. The data was resampled to 20 m per footprint, the spatial resolution of the EQ3 data, to better enable comparison with that dataset.

Spectral parameters were mapped onto a 200,000-facet shape model (~3 m per facet) [35,38] to further facilitate comparison between the spectral datasets. At each facet, spectral

slope and reflectance at 0.55 µm from multiple, overlapping OVIRS footprints were averaged (Fig. 6B). Spectral slope was calculated from 0.5 to 1.0 µm with a linear least-squares fit to each spectrum from both EQ3 and the corrected Bennu Farewell Tour dataset (fig. S32).

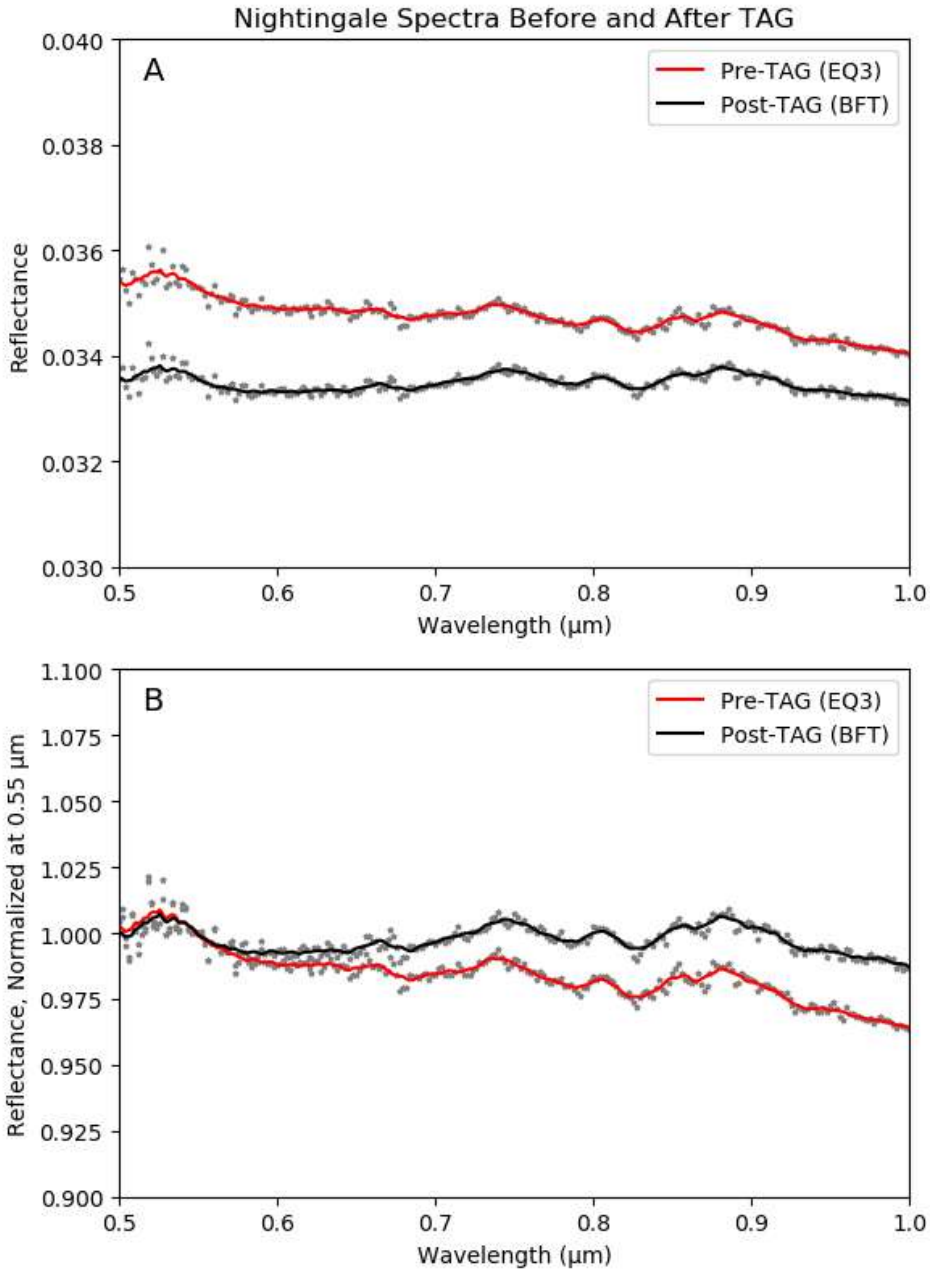

Figure S30. Visible – near-infrared OVIRS spectra of the Nightingale site (region from 53 to 57 deg N and 40 to 44 deg E) from before sampling (data (Simon et al. 2020) acquired during Equatorial Stations 3 (EQ3) (red) [1] and after sampling (BFF dataset; black). The final flyby spectrum has been corrected for lower throughput due to dust on the OVIRS primary; (**A**) Nightingale is darker at all wavelengths from 0.4 – 1.5 µm in the post-sampling spectrum. (**B**) Nightingale is redder in the post-sampling spectrum, demonstrated with spectra normalized at 0.55 µm.

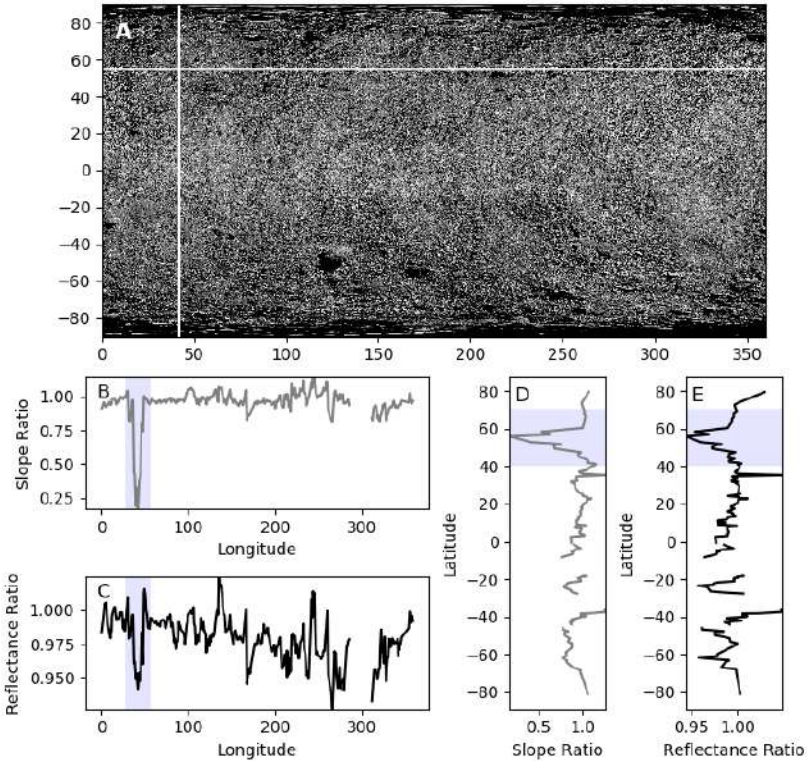

Figure S31. Latitude and longitude transects of spectral slope ratio (BFF/EQ3 spectral slopes from 0.5 – 1.0 µm) and reflectance ratio (BFF/EQ3 reflectance at 0.55 µm). (A) Transects were chosen to cover the Nightingale site at ~42E, 55N. (B, D) The slope ratio is significantly lower at Nightingale (blue box; >5 standard deviations) due to the reddening of BFF slope, which approaches zero in the BFF observations of Nightingale. (C, E) The reflectance ratio at Nightingale is ~3 standard deviations lower than other points on the latitude transect (E), however, the longitudinal reflectance ratio transect shows the effect of an increase in detector temperature with time, as the spacecraft scans moved from west to east; even with this effect, Nightingale still has a lower reflectance ratio due to darkening in BFF observations than surrounding longitudes (C).

Table S7. Spectral slope change in percent per micron at the sample site and outside the sample site calculated over multiple wavelength ranges. B', V, and X refer to approximate wavelengths of MapCam color bands.

Slope calculation	Sample site (percent per micron)*	uncertainty	Outside sample site (%/micron)*	unc.
0.5 to 1.0 µm	0.188	0.023	0.001	0.017
b' to v (0.47 to 0.55 µm)	0.245	0.030	0.029	0.055
v to x (0.55 to 0.85 µm)	0.202	0.027	0.000	0.029
b' to x (0.47 to 0.85 µm)	0.211	0.024	0.006	0.021
1.0 to 2.0 µm	0.058	0.018	0.001	0.012

*Change in spectral slope from pre-sampling (EQ3 dataset) to post-sampling (BFF dataset)

11 Collected Mass Estimate

11.1 SamCam Sample Verification Image Analysis

The collected sample mass was estimated using image analysis to determine particle volumes, assuming particle densities of 1800 kg m^{-3} and bulk densities of 1200 kg m^{-3} (fig. S32). We estimated the volume of particles contained within TAGSAM by comparing pre-sampling SamCam images of TAGSAM empty with those acquired post-sampling. The wrist motor allows TAGSAM to be rotated towards the camera, revealing the bottom surface, and providing a window into the interior collection chamber through a clear mylar flap.

Using the decrease in signal from reference to post-sampling, we invoked the principle of non-uniqueness and estimated the entire head to be populated by particles like those observed. The average brightness of the same TAGSAM surface after sampling experienced a factor of ~67.5 reduction, 1.48% of its pre-sampling value. Such a reduction corresponded to a minimum number of reflections. Relating the number of reflections directly to number of interfaces, or layers in the interior model representing the number of average particles within TAGSAM resulted in a total mass estimate of 450 g. The low and high estimates were 134 g and 1004 g.

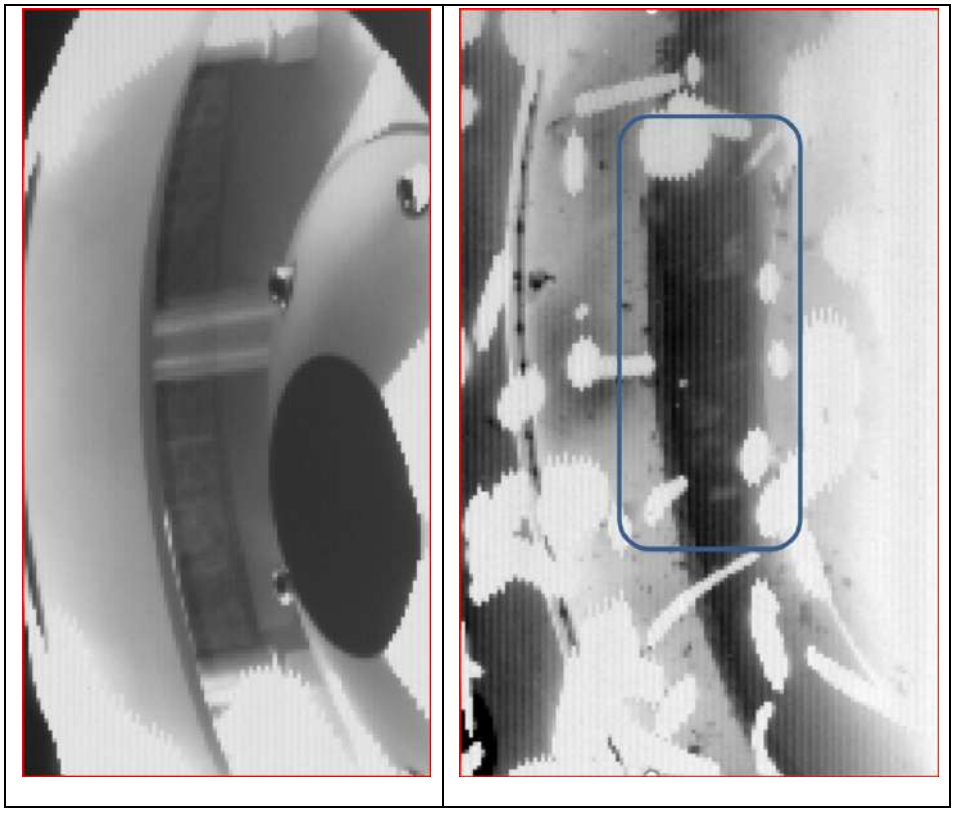

Figure S32. Image of the interior of TAGSAM before (a) and after (b) sampling. Images have similar illumination geometry. After image is much more strongly contrast-stretched (by a factor of 5) but shows a TAGSAM interior significantly darker than the before view, indicating the presence of a strong absorber. We can distinguish the outlines of individual particles within the

interior; we measure the average diameter of the most visible members to be 9.1 mm (± 0.5). The bright white blobs and streaks in (b) are particles escaping from TAGSAM.

11.2 Particles Adhering to Contact Pads

Twenty-four contact pads placed around the baseplate collected a separate surface sample (fig. S33). From the post-sampling SamCam and StowCam images, we observed a total of 23 particles, up to 4 mm in diameter, clinging to the contact pads mounted on the TAGSAM base plate (table S8). In addition, we observed at least 260 smaller particles clinging to the bottom surface or interior cavity of TAGSAM.

a **b**

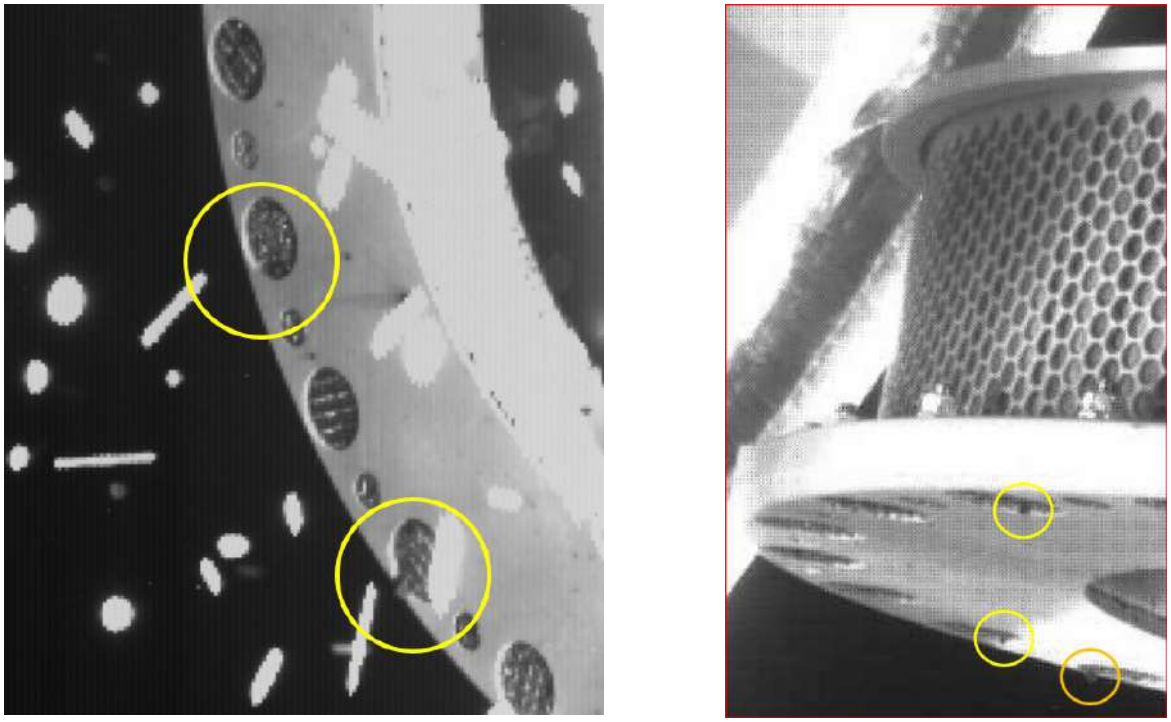

Figure S33. TAGSAM head contact pads successfully collected Bennu surface particles. Frames (a) SamCam and (b) StowCam show several particles lodged within the folds of the crushable stainless steel collection matrix. The two particles highlighted within the SamCam field appeared stationary through several frames of the very dynamic post-sampling observation field, which contained dozens of particles escaping from TAGSAM and tracking across the image field of view. The StowCam field was relatively static by comparison. Highlighted particles from both imagers are 2-to-4 mm in diameter based on their submillimeter plate scales.

Table S8. Bennu particles identified from both SamCam and StowCam images by comparing with images with similar illumination geometry taken before sampling. The images covered a range of exposure times from 1 msec to 5 seconds and a range of emission angles ranging from nearly perpendicular to nearly edge on. We identified particles both a) on the contact pads and b) off the contact pads adhering directly to the TAGSAM bottom surface or interior cavity and measured their approximate sizes.

a

Pad ID	#	Size (mm)
1	2	1.2, 1.2
2	1	2.9
3	1	1.4
4	2	4.1, 2.3
8	2	0.83, 0.75
9	1	2.7
10	1	2.4
11	1	1.1
12	1	0.83
13	4	1.06, 0.75, 1.5, 3.4
15	1	3.5
16	1	1.7
17	1	1.8
18	1	2.5
19	1	1.7
20	1	3.2
22	1	2.2

b

Location	#	Size (mm)
Between 16 & 17	1	1.5
Around Flat Base of Bottom Surface Circumference	> 260	< 0.75
Around Visible Section of Interior Cavity of TAGSAM Bottom Surface	> 180	< 0.75

11.3 Mass Loss Estimation from SamCam Image Analysis

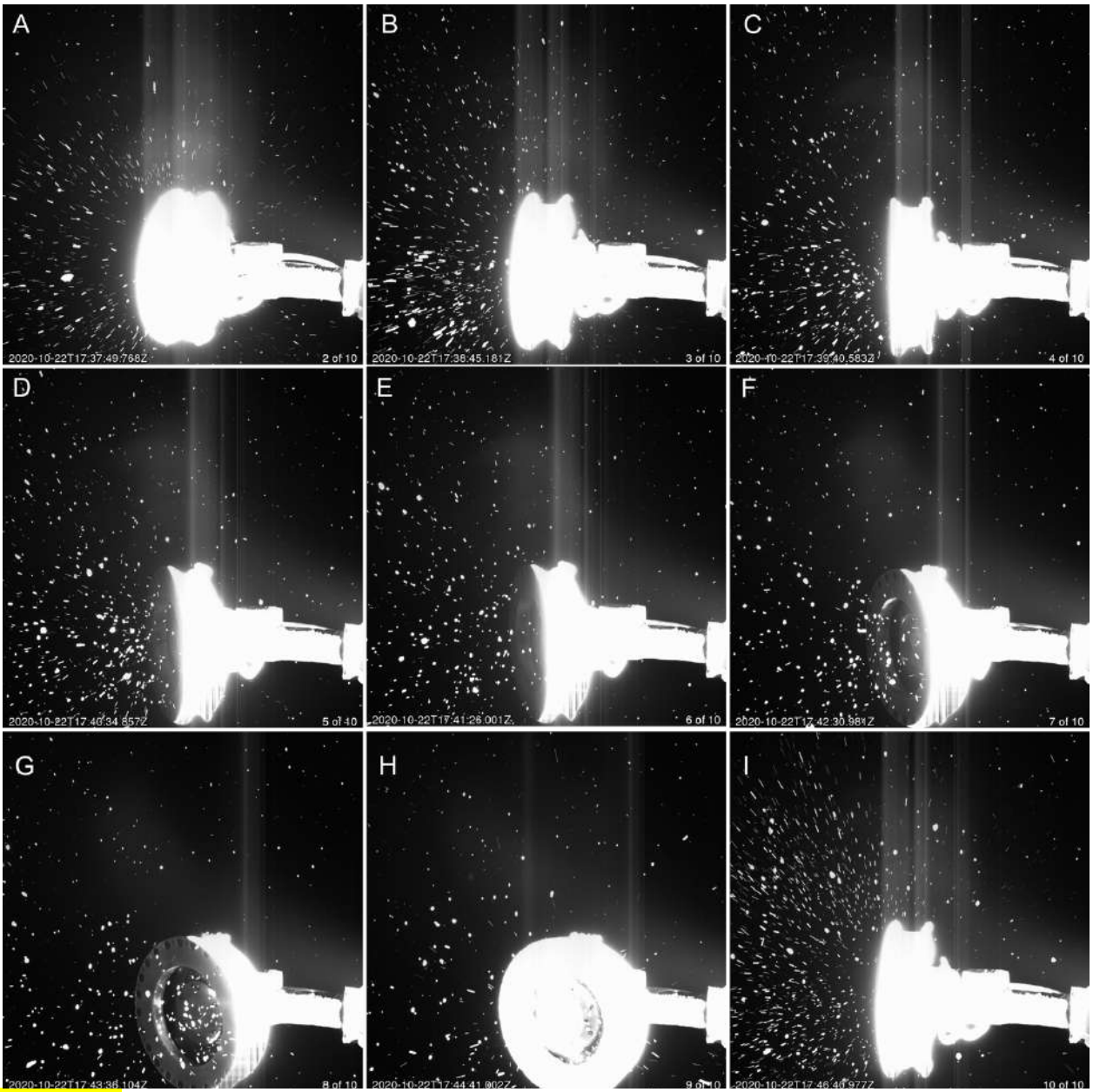

Figure S34. SamCam images acquired on October 22, 2020, during the TAGSAM post-sampling checkout. These long (1.5 s) exposure images highlight the escaping particles, which appear as radiating lines due to their relative motion during the image exposure period.

The median estimated range from the camera to the particles at the time of their first observation was 2.4 m and the median estimated velocity was 0.8 cm s^{-1}. For reference, TAGSAM itself was 2.0–2.2 m from the camera at the times of these observations. The nature of the angular camera field of view (FOV), which widens in physical space as the distance from the camera increases, means that there is more observable space farther from the camera than close to it. This creates an observational bias where particles are more likely to be observed across

three or more images if they are on the far side of TAGSAM and moving away from the camera. Those particles closer to the camera and moving towards it are more likely to move out of the FOV quickly and not persist across three or more images since the FOV is smaller in physical space on the near side of TAGSAM.

The size and mass of each particle was estimated using photometric techniques [53] using the 3D trajectories to determine range to each particle and phase angle. In total, we observed a minimum estimated 54.78 g of material leaving TAGSAM, with a mean particle mass of 0.030 g, and an average mass loss rate of 2.21 g min^{-1} between the first wrist movement and last image taken. Particle diameters ranged from 0.004–22.9 mm with a mean diameter of 0.920 mm (fig. S35). The particles we observed leaving TAGSAM only represent a fraction of the particles observed in the images, thus these results represent a lower bound.

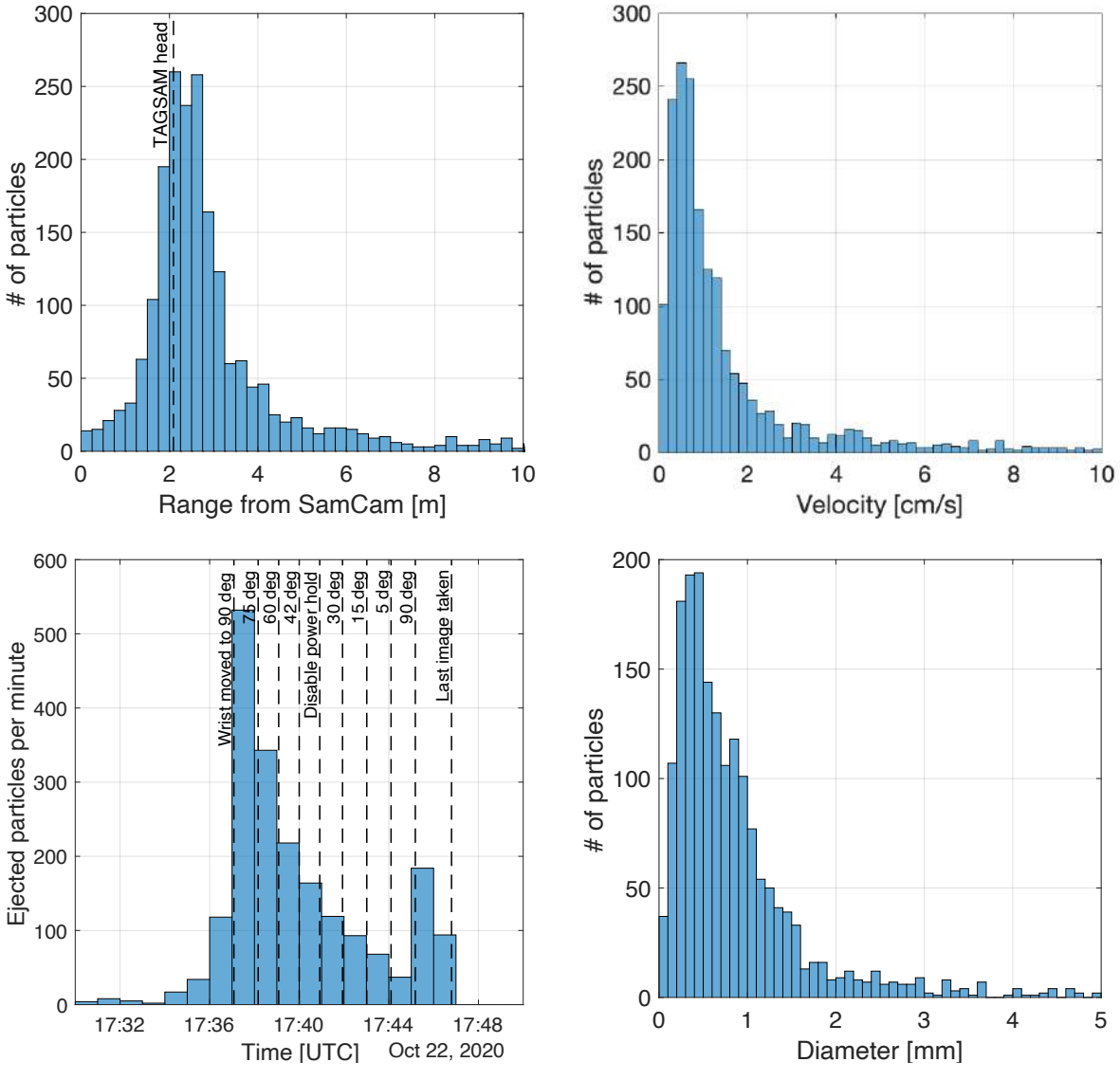

Figure S35. (a) Histogram of estimated range from the camera to each particle at the time of their first observation in 0.25 m bins. The vertical dashed line indicates the approximate range to

TAGSAM during the imaging sequence. (b) Histogram of estimated velocity of each particle in 0.2 cm s^{-1} bins. (c) Histogram of ejection times for each particle in 1-minute bins. Dashed vertical lines denote the times of spacecraft activities, including movements of the TAGSAM wrist joint to the specified angles, the disabling of the powered hold of the wrist joint at 17:41 UTC, and the epoch of the last image taken at 17:46 UTC. (d) Histogram of particle diameters in 0.1 mm bins.

We developed a set of techniques to automatically detect, associate, and track particles across each sequence of TAGSAM images, due to the large population of particles present in each of the images. This process begins with the raw image sequences and results in a set of detections and tracks that have been associated with one another to produce a set of particles that have been uniquely identified.

First, we subtract the global background level from each image by subtracting the mean of the image's masked dark pixels which corrects for the image bias and global dark signal. However, due to the imaging geometry and presence of TAGSAM in the image, a substantial amount of stray light remains in the image after global background subtraction. Thus, we use an iterative background subtraction technique [78] to remove as much of the remaining stray light in the image as possible. This iterative technique effectively acts as a low pass filter, using alternating size convolution kernels to build up a background image that is then subtracted from the image itself. After this correction, the only remaining signals in the image are those from TAGSAM, visible particles, and remaining stray light that was not subtracted during the process.

After performing the background and stray light correction, we apply a mask to each image to remove the remaining signal from TAGSAM. This mask is constructed manually for each image since the signal coming from TAGSAM is unique for each wrist position and exposure time. We also apply an additional mask to longer exposure images where the stray light is not completely subtracted during the image correction process. After applying the mask(s), the particles are the only signals remaining in the image.

Once the images have been corrected such that only the particle signals remain, automatic particle detection then begins by applying a strict digital number (DN) threshold to binarize the image to isolate the particles from background noise and remaining stray signal. For this analysis, pixels below a 100 DN threshold are set to zero, and above 100 DN are set to one. Once we determine the set of remaining "lit" pixels, we use a clustering algorithm to identify and cluster pixels that are most likely from the same particle source. This is accomplished using an iterative optimal clustering algorithm applying the Calinksi-Harabasz evaluation criterion [79]. The computed optimal *k*-value (representing the number of clusters or candidate particle detections in the image) is then used as the *k*-value in a *k*-means algorithm [80] which returns the coordinates of the clusters in the image. A tracking window of size 8 x 8 pixels is then centered around each coordinate, and the centroid (center) for each is determined. These centers represent the detections of candidate particles found in each image.

Once all the detections in the images are computed, they can be associated to one another across the image sequence using a variety of criteria. These associations allow unique particles to be identified and tracked across a sequence of images. The track association algorithm used for this analysis is based on a classical multiple hypothesis tracking (MHT) algorithm [81] which allows for a history of multiple hypotheses to be stored and tested for each detection and candidate track. The detection-to-track association is accomplished by exploiting

the fact that the particles in the image follow a nearly perfect linear path across the image sequence, due to the lack of external forces. More specifically, detections within a specified distance around the most current detection in the track are determined, and a line is fit to the set of all detection in that given track's history. All lines with a coefficient of determination greater than the allowable threshold ($R^2 > 0.99$) are flagged and stored as valid tracks.

After all possible tracks are computed, they must be constrained and deconflicted to only allow tracks that are physically possible and uniquely associated with an exclusive set of detections. We accomplish this by first only keeping tracks that have detection-to-detection velocities (observed angular velocities) in the same direction, which enforces that the particle does not change direction over time. We place a separate constraint on the range of observed angular accelerations in each track, to enforce that the acceleration is approximately constant, as expected for a constant velocity trajectory. Once the constraints are applied, we deconflict the tracks from one another to ensure that each track is associated with an exclusive set of detections, such that no two tracks share any detections. The remaining tracks after deconfliction represent the final set of which is used for further trajectory reconstruction and photometric analysis.

We reconstructed the 3D trajectory of each particle using a method developed to reconstruct the particle ejection events observed at Bennu by OSIRIS-REx [29,55]. The particles' trajectories were estimated using three or more observations, assuming each particle is following a constant-velocity linear trajectory through 3D space and knowing the ejection location. In this case, the ejection location was found by finding the intersection of a linear fit to the particle's detections with an ellipse representing the location of TAGSAM within the images. The range from the camera to TAGSAM at each wrist position is known from 3D modeling of the spacecraft. Therefore, this intersection point of the particle's trajectory with TAGSAM within the image can be projected into a 3D position for the ejection location of each particle. The 3D position and velocity of the particles was then estimated using this ejection location and the observed angular positions of each particle within the images. See [55] for a more detailed description of this trajectory reconstruction method.

We then estimated the size of each particle photometrically, using the reconstructed 3D trajectories for range and phase angle information. The total DN signal for each observation, measured by integrating the fitted PSF model, was converted to V-band apparent magnitude m_v using the following equation:

$$m_v = zmag - \log_{10}(DN) + 2.5\log_{10}(t) \qquad \text{Equation S.24}$$

where *DN* is the total measured signal from PSF fitting and t is the image exposure time in seconds. The $zmag$ value used was 9.7, which was determined based on the bright star Spica that was visible in the images. This value was verified to produce m_v values that provide a good match between particle diameters derived from photometry and those directly measured for the larger resolved particles within the images.

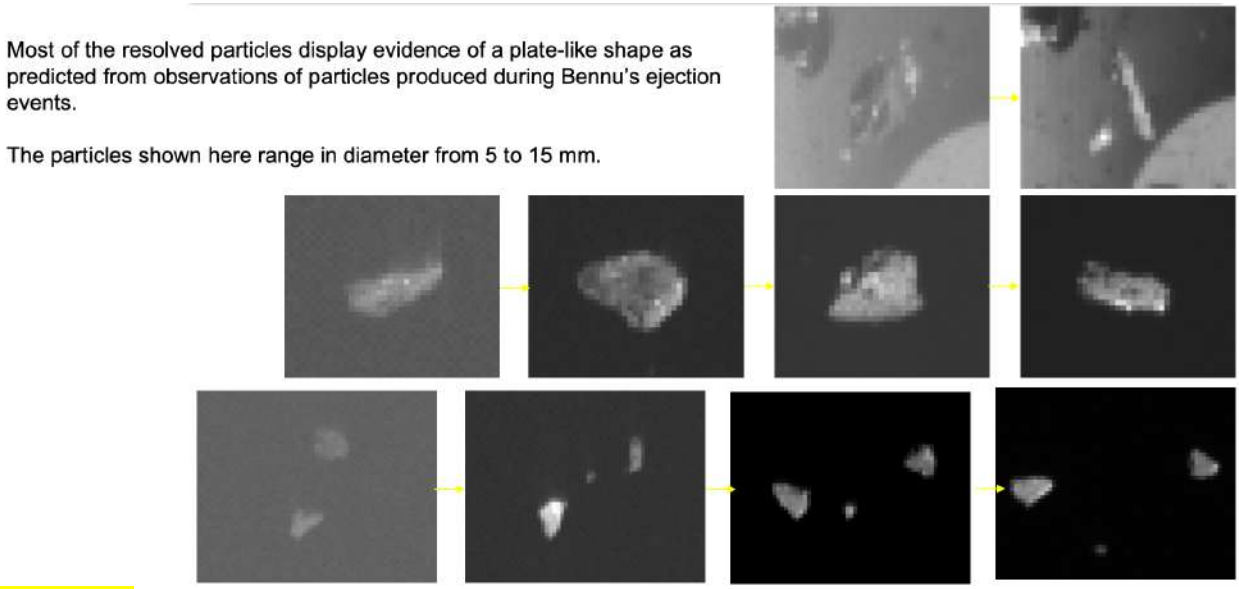

Figure S36. Postage-stamp cutouts from SamCam images of the escaping particles. The same particle is shown in each row, providing multiple viewing angles to assess the shape.

The apparent magnitude was then converted to absolute magnitude given the range and phase angle as determined by the trajectory estimation. We used a phase coefficient of 0.013 magnitude per degree of phase angle, which was estimated for particles ejected from the surface of Bennu [53]. We estimated the photometric diameter of each particle from the absolute magnitude using the average Bennu albedo of 0.044 [31]. Based on the conclusions of Hergenrother et al [53] and Chesley et al [54] for previously observed ejected Bennu particles, we assumed the particles were "flake-like" ellipsoids with semi-axes of a×a×b and an axial ratio b/a = 0.27. For the reported particle diameters, we used the diameter of a volume-equivalent sphere, $D=2\sqrt[3]{(a^2\ b)}$. The mass of each particle was estimated using the ellipsoid volume and a presumed particle density of 1800 kg m^{-3}.

Due to the automated detection and tracking method used, false positive detections and mis-associations of detections (i.e., linking detections between images that are not the same particle) is possible and expected for a portion of the detections and tracks. Therefore, particles with an estimated velocity greater than 20 cm s^{-1} were assumed to include mis-associations or false detections and were not included in the results presented here. This applied velocity outlier threshold is an order of magnitude greater than both the median particle velocity and the velocity that TAGSAM itself was moving during the wrist movements, which was 0.5–1 cm s^{-1}.

12 Size Frequency Distribution of the Collected Sample

12.1 SamCam Analysis of Particles on TAGSAM

The spatial resolution at the disk is 1 mm per pixel. Using five continuous SAMCAM images, particles and dark spots on the bright TAGSAM disk were measured by approximating them as ellipses. We produced plots of cumulative size frequency distribution SFD for each image. Data for > 2 mm particles (2 pixels) are fitted with the equation:

$$y = ax^p \qquad \text{Equation S.25}$$

using the least-square method, where y is cumulative particle count, x is the particle major axis, is an empirical coefficient, and p is the power-law index. The uncertainty in p is estimated from the standard deviation of the power-law indexes of these five data.

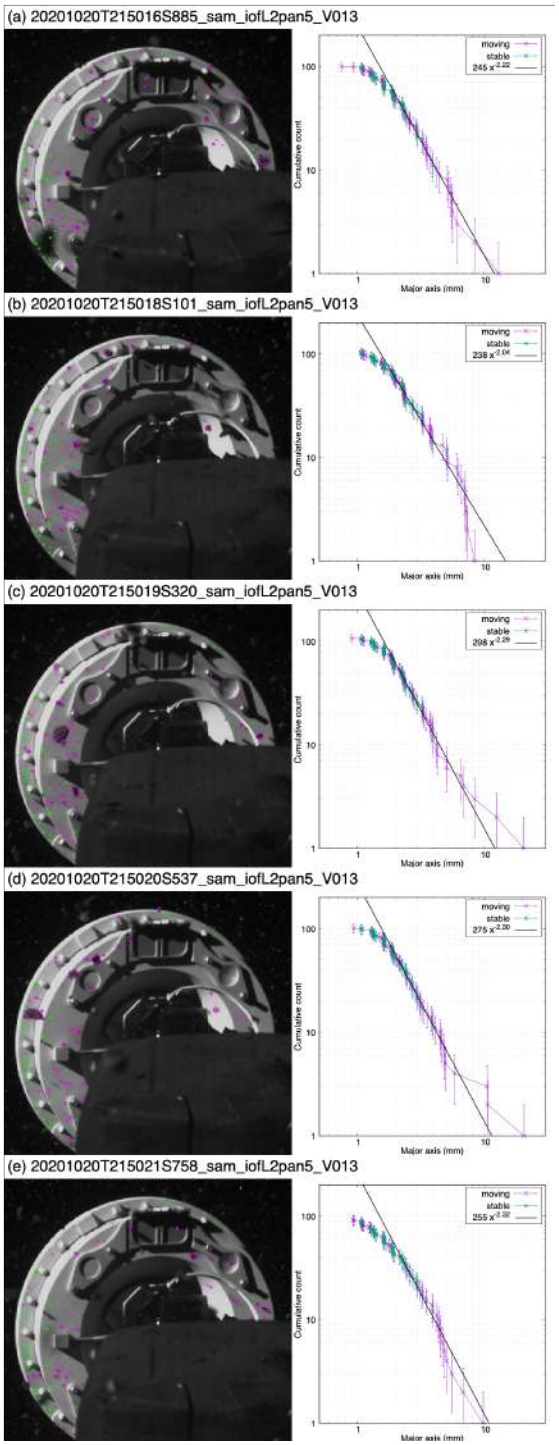

Figure S37. Particles kicked up by the sampling disturbance onto the top of the TAGSAM disk. Each figure shows a SamCam image during back-away after sampling and its corresponded particle SFD. Particles that appear to be stationary on the disk are marked with green, and others (i.e., moving) are marked with magenta.

The five SFDs were added to obtain the "total SFDs" (fig. S38). The average of the power-law index from five images and the power-law index p from the total SFD are the same: -2.23 (table S9). This agreement supports the validity of the analysis.

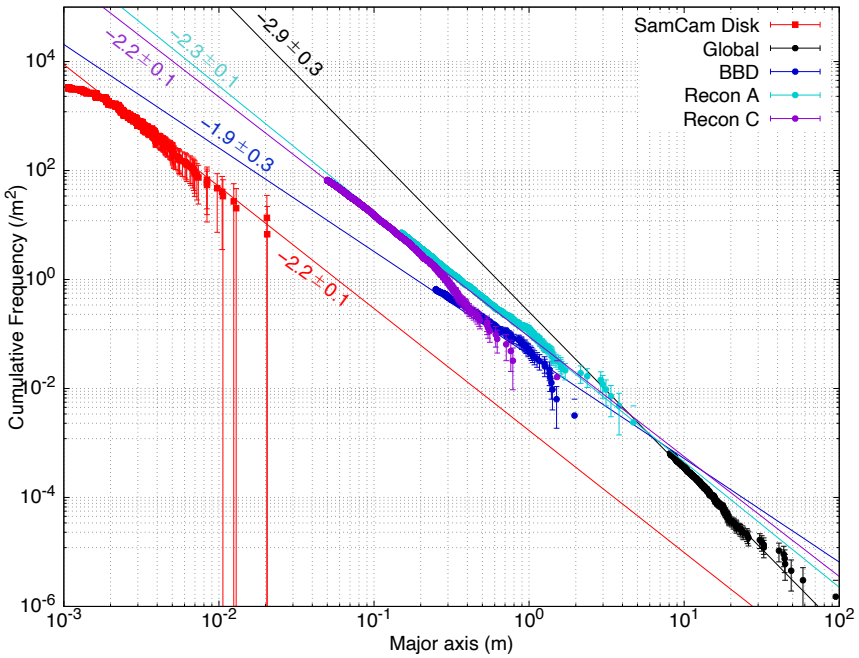

Figure S38. Cumulative SFD of kicked up particles found with high confidence level (red particles labeled in each image) on the disk. The cumulative SFD is estimated based on the added data points.

Image ID	Power-law index
20201020T215016S885_sam_iofL2pan5_V013	–2.22
20201020T215018S101_sam_iofL2pan5_V013	–2.04
20201020T215019S320_sam_iofL2pan5_V013	–2.29
20201020T215020S537_sam_iofL2pan5_V013	–2.30
20201020T215021S758_sam_iofL2pan5_V013	–2.32

Table S9. Power-law index determined from particle counts in the images shown in fig. S37.

12.2 NavCam 2 Analysis of Particles in the Dust Cloud

The post-sampling NavCam 2 images revealed consistency between the surface particle SFD and those kicked up by the sampling event. NavCam 2 images captured a moving curtain of ejecta particles (fig. S39A). We identified moving particles in the ejecta curtain by comparing several consecutive images and measured their sizes assuming that these particles are on the surface. The obtained SFD follows a power law from 2 cm to 30 cm (fig. S39B), overlapping the size range measured by Recon observations.

Here we used these surface boulders as scale references for NavCam image. Because actual dust cloud is somewhere between the surface and the camera, the spatial scale we used is an upper estimate. The particles that are part of the optically thick ejecta cloud may have some variation in height. However, the height variation is unlikely large because self-shadowing is not observed across the cloud. Thus, relative scale estimate within the cloud curtain should be more accurate than the absolute scale. We also evaluated the robustness of our SFD estimation by identifying particles possibly outside the dust cloud. We identified particles located outside the dust cloud in two-dimensional images as out-of-cloud particles. The SFD of these possible out-of-cloud particles has a cumulative exponent of –3.5, not much different from particles inside the dust cloud, suggesting that the SFD of kicked up particles is homogeneous and that estimated relative SFD is robust.

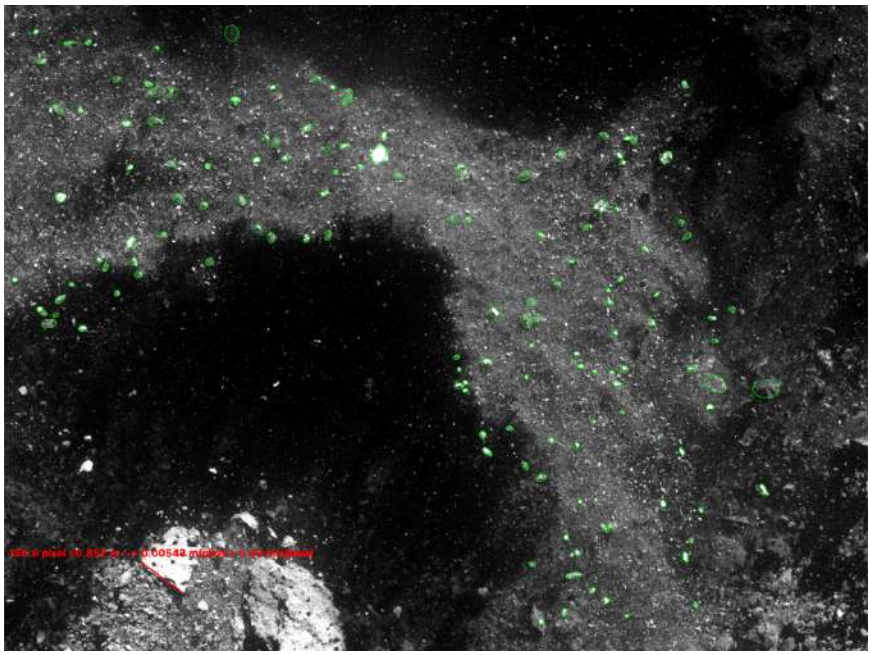

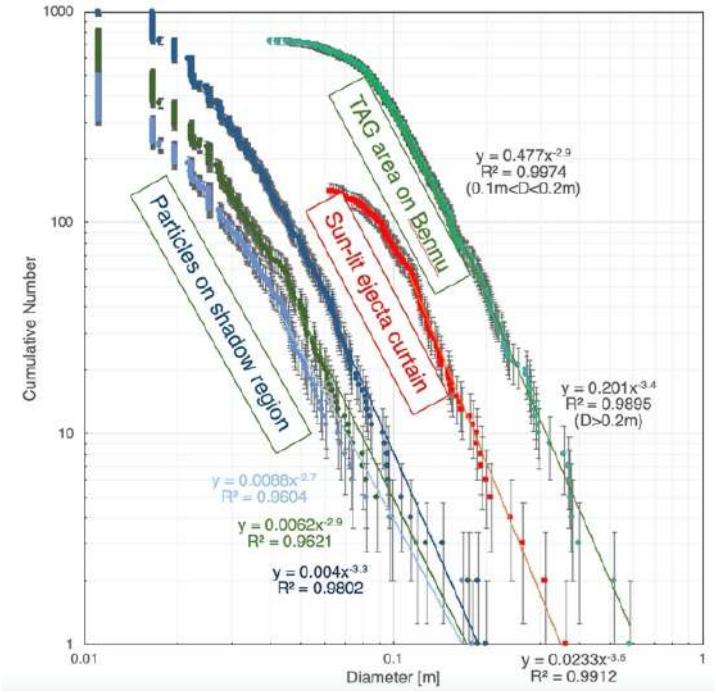

Figure S39. Particles in ejecta curtain generated by the sampling disturbance. (**A**) A NavCam 2 image of the TAGSAM ejecta curtain (20201020T215045S680_nft_L2). Particles moving in the sunlit side of the curtain are marked with light green. The motion was confirmed by comparing adjacent images. The shadowed region also contains moving ejecta particles. Because of the absence of a bright background curtain, smaller particles could be identified in the shadow region. (**B**) Comparison among the SFD of particles on Bennu surface near the sampling area, that in the sunlit side of the ejecta curtain, and that in the shadow region. We placed three different threshold brightness levels for finding small particles in the shadow region, but the obtained three SFDs agree with each other within the effort bars.